SYNTHESIS AND NMR-BASED NETWORK STRUCTURE ANALYSIS OF CATIONIC HYDROGELS FOR SEAWATER APPLICATIONS

Zur Erlangung des akademischen Grades eines

DOKTORS DER NATURWISSENSCHAFTEN

(Dr. rer. nat.)

von der KIT-Fakultät für Chemie und Biowissenschaften

des Karlsruher Instituts für Technologie (KIT)

genehmigte

DISSERTATION

von

M.Sc. Christian Fengler

aus Berlin

1. Referent: Prof. Dr. Manfred Wilhelm
2. Referent: Prof. Dr. Patrick Théato
Tag der mündlichen Prüfung: 26. Oktober 2022

DECLARATION

Hiermit erkläre ich, Christian Fengler, dass ich die vorliegende Doktorarbeit selbstständig im Rahmen der Betreuung durch Prof. Dr. Manfred Wilhelm verfasst habe und keine anderen als die von mir angegebenen Quellen und Hilfsmittel benutzt habe, die wörtlich oder inhaltlich übernommenen Stellen als solche kenntlich gemacht und die Satzung des Karlsruher Instituts für Technologie (KIT) zur Sicherung guter wissenschaftlicher Praxis in der gültigen Fassung beachtet habe.

Karlsruhe, den 22. Januar 2023

Christian Fengler

ABSTRACT

Superabsorbent polymers (SAPs) are hydrophilic polymer networks (i. e., hydrogels) that contain charged monomer units along the polymer backbone. Poly(sodium acrylate) (PSA), which has negatively charged carboxylate groups, is the most prominent chemical structure of SAPs. Recent studies have shown that PSA can be used as a separation medium for the desalination of salt water. This approach, however, is limited to NaCl solutions because the divalent Mg^{2+} and Ca^{2+} cations in seawater interact electrostatically with the anionic polymer backbone of PSA, inducing thereby a network collapse. To overcome this limitation, this dissertation explores the swelling and desalination capacity of cationic SAPs in seawater. Two cationic SAP model systems with distinct functional groups were synthesized. The first one is based on a poly(acrylamide) (PAM) derivative with a trimethyl quaternary ammonium group as the positively charged monomer unit. The second model system is based on poly(vinyl amine) (PVAm) bearing positively charged ammonium groups. Swelling capacity measurements reveal that divalent SO_4^{2-} anions in seawater induce a network collapse of PVAm similar to the PSA analogue. In contrast, the swelling behavior of PAM hydrogels is fully unaffected by seawater, suggesting that the quaternary ammonium moiety is essential to provide seawater resistant swelling properties of SAPs. In addition to swelling capacity studies, this dissertation aims to advance our understanding of the intriguing interplay between macroscopic, mechanical properties and molecular dynamics of the hydrogel network. Due to the inherent multi-length scale structural complexity of hydrogels, the quantitative correlation of mechanical properties with molecular dynamics remains a longstanding challenge. An advanced rheometer setup consisting of a portable low-field NMR unit that is integrated into a rheometer was used to study the gelation kinetics of acrylic acid (AAc) hydrogels. The elastic modulus G' was studied by small amplitude oscillatory time sweeps whereas the local molecular mobility of polymer network chains was probed by T_2 relaxation measurements. From the in-situ G' and T_2 correlation plots, it can be concluded that the elastic plateau modulus is inversely proportional to the T_2 relaxation time of the hydrogel. Consequently, the mechanical strength of hydrogels can be predicted based on the segmental mobility of polymer network chains, which has important implications for the further development of non-invasive and forceless mechanical characterization techniques.

ZUSAMMENFASSUNG

Superabsorbierende Polymere (SAPs) sind hydrophile Polymernetzwerke (i. e., Hydrogele), die geladene Monomereinheiten entlang der Polymerhauptkette enthalten. Poly(natriumacrylat) besteht aus negativ geladenen Carboxylatgruppen und ist die bekannteste SAP Grundstruktur. Jüngste Studien haben gezeigt, dass Poly(natriumacrylat) für die Salzwasserentsalzung verwendet werden kann. Dieser Ansatz ist jedoch auf NaCl-Lösungen beschränkt, da die im Meerwasser enthaltenen zweiwertigen Kationen Mg^{2+} und Ca^{2+} elektrostatisch mit dem anionischen acrylat-basierten Polymerrückgrat wechselwirken und dadurch einen Netzwerkkollaps induzieren. Um diese Limitierung zu überwinden, untersucht diese Dissertation die Quellkapazität von kationischen SAPs in Meerwasser. Zwei kationische SAP Modellsysteme mit unterschiedlichen funktionellen Gruppen wurden synthetisiert. Das erste SAP basiert auf einem Poly(acrylamid) (PAM) Derivat, welches eine positiv geladene quartäre Trimethylammoniumgruppe trägt. Das zweite Modellsystem basiert auf Poly(vinylamin) (PVAm), das positiv geladene Ammoniumgruppen trägt. Quellkapazitätsmessungen zeigen, dass zweiwertige SO_4^{2-} Anionen in Meerwasser, analog zu Poly(natriumacrylat), einen Netzwerkkollaps von PVAm verursachen. Allerdings ist das Quellverhalten von PAM nicht durch SO_4^{2-} Anionen beeinflusst, weshalb sich PAM basierte SAPs speziell für Meerwasseranwendungen eignen. Neben den Studien zur Quellfähigkeit, zielt diese Dissertation darauf ab, unser Verständnis des Zusammenspiels zwischen mechanischen Eigenschaften und der molekularen Dynamik des Hydrogelnetzwerks auszubauen. Aufgrund der inhärenten strukturellen Komplexität von Hydrogelen, welche sich über mehrere Längenskalen erstreckt, ist eine quantitative Korrelation mechanischer Eigenschaften mit der molekularen Dynamik stets eine Herausforderung. Zur Untersuchung der Gelierungskinetik von Acrylsäure basierten Hydrogelen wurde ein fortschrittlicher Rheometeraufbau verwendet. Dieser besteht aus einer tragbaren Niederfeld NMR Einheit, die in ein Rheometer integriert werden kann. Das Elastizitätsmodul G' wurde mithilfe von oszillierender Verscherung gemessen, während gleichzeitig die lokale molekulare Mobilität von Polymernetzwerkketten durch T_2 Relaxationsmessungen ermittelt wurde. Die in-situ G' und T_2 Korrelationen ergeben, dass das elastische Plateaumodul umgekehrt proportional zur T_2 Relaxationszeit des Hydrogels ist. Folglich kann die mechanische Festigkeit von Hydrogelen aus der molekularen Mobilität von Polymernetzwerkketten vorhergesagt werden, was entscheidend für die Weiterentwicklung von nicht-invasiven und kraftfreien mechanischen Messungen von Polymergelen ist.

PUBLICATIONS

Some of the research covered in this dissertation appeared previously in the following peer-reviewed publications:

1. C. Fengler, J. Keller, K.-F. Ratzsch, and M. Wilhelm. "In Situ RheoNMR Correlation of Polymer Segmental Mobility with Mechanical Properties during Hydrogel Synthesis." In: *Advanced Science* 9.4 (2022), e2104231.

2. C. Fengler, S. Spange, M. Sommer, and M. Wilhelm. "Synthesis of Superabsorbent Poly(vinylamine) Core–Shell Particles Monitored by Time-Domain NMR." In: *Macromolecules* 55.1 (2022), pp. 349–358.

3. N. W. Radebe, C. Fengler, C. O. Klein, R. Figuli, and M. Wilhelm. "Rheo-IR: A combined setup for correlating chemical changes via FTIR spectroscopy and rheological properties in a strain-controlled rheometer." In: *Journal of Rheology* 65.4 (2021), pp. 681–693.

4. T. Uhlig, C. Fengler, A. Seifert, F. Taubert, L. Kaßner, H.-J. Hähnle, et al. "Reversible and Stable Hemiaminal Hydrogels from Polyvinylamine and Highly Reactive and Selective Bis(N -acylpiperidone)s." In: *ACS Macro Letters* 10.3 (2021), pp. 389–394.

5. A. Jangizehi, C. Fengler, L. Arens, and M. Wilhelm. "Optimizing the Power Production in an Osmotic Engine via Microfluidic Fabricated and Surface Crosslinked Hydrogels Utilizing Fresh and Salt Water." In: *Macromolecular Materials and Engineering* 305.7 (2020), p. 2000174.

6. C. Fengler, L. Arens, H. Horn, and M. Wilhelm. "Desalination of Seawater Using Cationic Poly(acrylamide) Hydrogels and Mechanical Forces for Separation." In: *Macromolecular Materials and Engineering* 305.10 (2020), p. 2000383.

"It's pretty well established that there is an overconfidence effect. [...]
you don't have the competence to assess your own competence. [...]
you need competence in order to assess your own competence. [...]
Everyone has the Dunning-Kruger effect."

– Steven Novella, *The Skeptics' Guide to the Universe, Podcast #557*

ACKNOWLEDGMENTS

I would like to express my deepest appreciation to my supervisor Prof. Dr. Manfred Wilhelm, who provided continuous encouragement, expertise, philosophical insights into the scientific method, many useful physical quantities and units, and who gave me the freedom to pursue my research interests. I am grateful to have had the pleasure of working with my collaboration partners Prof. Dr. Michael Sommer, Prof. Dr. Christian Holm, Dr. Karl-Friedrich Ratzsch, Dr. Jonas Keller, Dr. Nonkululeko Radebe, Dr. Amir Jangizehi and Dr. Lukas Arens without whom this research would not have been possible. Their enthusiastic assistance and insightful comments have been essential at every stage of the research projects. I would like to express my sincere gratitude to the Fonds der Chemischen Industrie for providing financial support by the Kekulé fellowship. Special thanks to the Karlsruhe House of Young Scientists for funding my research visit to Stanford University. Many thanks to my office-mate Christos Georgantopoulos for all the fun times during the PhD and the years to come. I would also like to thank all members of the Polymeric Materials group for cultivating a supportive and diverse working environment as well as their efforts to ensure a well-functioning research infrastructure.

CONTENTS

I Introduction and Fundamentals

1 Research objectives and outline 3

2 Polymer gels 7
- 2.1 Classification and historical perspectives 7
- 2.2 Multi length-scale complexity of polymer gels 10
- 2.3 Swelling theory of superabsorbent polymers 13

3 NMR Relaxometry 19
- 3.1 Energy exchanges of a nucleus in a magnetic field 19
- 3.2 Relaxation phenomena based on molecular motion 20
- 3.3 TD NMR pulse sequences in soft matter analysis 24

II Results and Discussion

4 Synthesis of cationic hydrogel model systems 31
- 4.1 Monodisperse particles via droplet microfluidics 31
- 4.2 Poly(acrylamide) - the dormant framework 34
- 4.3 Poly(vinylamine) - the versatile framework 35

5 Swelling properties 41
- 5.1 Influence of synthetic parameters on swelling 41
- 5.2 Effect of salt concentration and ion valency on swelling 48

6 Dynamic-based assessment of network structure using NMR relaxometry 53
- 6.1 Improved protocol for the regularized inversion of time-domain NMR data 53
- 6.2 Network structure analysis by double quantum NMR 57
- 6.3 Topological insight into core-shell hydrogels 64

7 Rheo-NMR: Correlation of molecular dynamics with mechanical properties during gelation 71
- 7.1 Technical details of the Rheo-NMR device 71
- 7.2 Advanced monitoring of acrylic acid gelation 73

8 Seawater applications of cationic hydrogels 87
- 8.1 Membrane-free desalination of seawater 87
- 8.2 Harnessing sustainable mechanical energy from salinity gradients 95

9 Conclusion and outlook 99

III Appendix

A Synthesis Procedures 105

B Characterization and Application 111

Bibliography 120

Figure 1.1 Salt ion concentration gradients drive the Gibbs-Donnan equilibrium. 3
Figure 1.2 Cationic repeating units of the SAP model systems. 4
Figure 2.1 Binding energies of different crosslinks in polymer gels. 8
Figure 2.2 Repeating unit of PHEMA. 8
Figure 2.3 Repeating units of PEG, PPG, and PNIPAM. 9
Figure 2.4 Nanoscopic topological defects in polymer hydrogels. 11
Figure 2.5 Designing SAPs requires the consideration of at least three different length scales. 12
Figure 2.6 Illustration of the capillary effect. 13
Figure 2.7 Thermodynamic lattice model for polymer - solvent mixing. 15
Figure 2.8 Cyclic rank ξ for a network with functionality f and number of network strands ν. 16
Figure 3.1 Spin quantization of a spin-1/2 nucleus in an external magnetic field B_z. 19
Figure 3.2 Relaxation of the magnetization according to the Bloch equations in a NMR experiment after excitation with a $\pi/2$ pulse. 21
Figure 3.3 Dipolar coupling of two neighboring proton spins depends on the distance r and angle θ. 23
Figure 3.4 Saturation recovery pulse sequence to obtain T_1 relaxation times. 25
Figure 3.5 Hahn echo (a) and CPMG (b) spin echo pulse sequences to measure T_2 relaxation times of soft matter. 26
Figure 3.6 Modified Baum-Pines pulse sequence to measure residual dipolar couplings in low-field benchtop NMR spectrometers. 27
Figure 4.1 Glass capillary microfluidic device built within this dissertation. 33
Figure 4.2 Synthesis of cationic poly(acrylamide-*co*-(3-acrylamidopropyl) trimethylammonium chloride) (PAM) hydrogels. 34
Figure 4.3 Vinylamine – ethanimine tautomerism. 35

Figure 4.4 Synthesis of the *N*-vinylformamide (NVF) based hydrolysis-resistant crosslinker using BBE for the synthesis of PVAm hydrogels. 36
Figure 4.5 Size distribution of monodisperse, spherical PNVF hydrogels. 37
Figure 4.6 Two-step synthesis of monodisperse PVAm hydrogels. 37
Figure 4.7 Chemical structure of hemiaminal and aminal functional groups. 38
Figure 4.8 Reaction of PVAm with water-soluble bis(*N*-acylpiperidone) used for surface-crosslinking. 38
Figure 4.9 Crosslinking reaction of PVAm with OBP compared to PVAm hydrogel swelling kinetics. 40
Figure 5.1 Experimental setup for water absorbency measurements. 41
Figure 5.2 Influence of pre-gel monomer concentration on equilibrium swelling capacity. 42
Figure 5.3 Reaction pathways of pendant vinyl groups attached to an arbitrary polymer chain. 43
Figure 5.4 Influence of synthetic parameters on swelling capacity of cationic PAM hydrogels. 44
Figure 5.5 Spherical particle swelling. 45
Figure 5.6 Swelling kinetics of PNVF hydrogels with $DC = 2\,\text{mol\%}$ and varying dry particle sizes. 46
Figure 5.7 Influence of charged polymer backbone on swelling kinetics. 47
Figure 5.8 Salt concentration dependency of the equilibrium swelling capacity in NaCl solution and seawater. 49
Figure 5.9 Equilibrium swelling capacity of PSA and PVAm hydrogels as a function of divalent ion concentration. 50
Figure 5.10 Chemical structure of glycidyl trimethylammonium chloride. 52
Figure 6.1 Use of the L-curve approach to find the optimal regularization parameter λ. 56
Figure 6.2 ^{1}H DQ NMR data treatment and tri-exponential fitting results. 60
Figure 6.3 ^{1}H DQ build-up curves and corresponding D_{res} distributions of PNVF hydrogels with varying DC. 61
Figure 6.4 Influence of a charged polymer backbone and swelling on the D_{res} distribution of PNVF and PVAm hydrogels. 63
Figure 6.5 Effect of surface-crosslinking on equilibrium swelling capacity. 65

Figure 6.6 Average T_1 magnetization build-up obtained by a saturation experiment. 66
Figure 6.7 T_2 relaxation curves and distributions for PVAm hydrogels with increasing degree of surface-crosslinking. 68
Figure 6.8 Geometric mean $GM(T_2)$ and coefficient of variation $CV(T_2)$ of the computed and T_2 distributions of PVAm_DC2 core-shell particles. 69
Figure 7.1 Photo of a DHR-3 rheometer with TD NMR attachment. 72
Figure 7.2 Technical outline of the low-field NMR magnet used as rheometer attachment. 72
Figure 7.3 Sol-gel transition. 74
Figure 7.4 Schematics of the Rheo-NMR device and experimental observables. 74
Figure 7.5 Small amplitude oscillatory time sweeps. 75
Figure 7.6 Kinetic analysis of normalized rheological gelation curves. 76
Figure 7.7 Final loss tangent $\tan\delta = G''_{\max}/G'_{\max}$ and the gelation rate exponent n as a function of DC. 77
Figure 7.8 Time-evolution and data analysis of T_2 relaxation curves during the gelation of the sample with $DC = 0.1$ mol% obtained by a MSE/CPMG pulse sequence. 78
Figure 7.9 a) Correlation plot of the elastic modulus G' against T_2 relaxation times. 79
Figure 7.11 Chemical structure of trimethylolpropane triacrylate. 80
Figure 7.10 T_2 relaxation times (a) and β (b) at constant $G' = 1$ kPa as a function of DC. 81
Figure 7.12 Time-evolution and kinetic analysis of NMR signal intensity during the gelation of the sample with $DC = 0.1$ mol%. 82
Figure 7.13 G' as a function of the normalized polymer NMR signal intensity I_{poly} obtained by Equation 7.5. 84
Figure 7.14 The confining tube of a polymer chain in a semi-dilute entangled polymer solutions. 84
Figure 8.1 Discontinuous three-step desalination process using SAP particles as separation medium. 88
Figure 8.2 Salt rejection of PAM particles in 1 wt% NaCl solution. 90
Figure 8.3 Schematic of the hydraulic press setup for the desalination of seawater using SAPs. 91
Figure 8.4 Photo of the hydraulic press setup. 92

Figure 8.5 Desalination of artificial seawater using cationic SAP particles. 92
Figure 8.6 Salt partitioning of salt ions during seawater desalination. 94
Figure 8.7 Concept of the osmotic engine to harness mechanical energy from natural salinity gradients using SAPs. 95
Figure 8.8 Syringe prototype of the osmotic engine. 96
Figure 8.9 Average maximum power output as a function of pressure exerted by the weight of the external load. The highest average power output of $\overline{P} = 0.39\ \mathrm{W\,kg^{-1}}$ was achieved for the external load of 5810 Pa (391 g). 97
Figure 8.10 Potential chemical postmodifications of PSA. 98
Figure A.1 Chemical structures of APTAC and AM. 105
Figure A.2 Chemical structure of BNVF. 107
Figure A.3 ^{1}H NMR spectrum of BNVF recorded in $CDCl_3$ at 400 MHz. 107
Figure A.4 ^{1}H NMR spectrum of PNVF and PVAm hydrogel particles with $DC = 1$ mol% swollen in D_2O. 109
Figure A.5 Chemical structure of AAc. 110
Figure B.1 Raw data of the combined MSE and CPMG data sets of sample PNVF_DC2. 113
Figure B.2 Comparison of the combined MSE and CPMG/XY16 pulse sequence with the FID after a $\pi/2$ pulse and a Hahn echo experiment. 114
Figure B.3 a) T_1 magnetization build-up of a fully gelled PAAc hydrogel sample with $DC = 0.1$ mol% measured by a saturation recovery pulse sequence. b) Time-evolution of the ^{1}H NMR signal intensity of a degassed (two freeze-pump-thaw cycles) and a non-degassed AAc sample with $DC = 0$ mol%. 116

LIST OF TABLES

Table 4.1 Overview of experimental microfluidic parameters and the resulting dry particle diameter. 33
Table 6.1 Calculated mean $GM(D_{res})$ and coefficients of variation $CV(D_{res})$ of log-transformed D_{res} distribution of PNVF and PVAm samples. 62

Table 6.2 Fitting results of the T_1 magnetization build-up of PNVF and PVAm samples. 67
Table A.1 Overview of the synthesized PAM hydrogel samples. 106
Table A.2 Overview of synthesized neutral PNVF, cationic PVAm and PVAm core-shell hydrogel samples with dry particle diameters sizes of ≈ 600 µm. 110

ACRONYMS AND ABBREVIATIONS

AAc	acrylic acid
AM	acrylamide
APS	ammonium persulfate
APTAC	(3-acrylamidopropyl) trimethylammonium chloride
BP	Baum-Pines pulse sequence
CPMG	Carr–Purcell–Meiboom–Gill pulse sequence
DC	degree of crosslinking
DQ NMR	double quantum NMR
FID	free induction decay
HE	Hahn echo pulse sequence
MBA	*N*,*N*′-methylenebis(acrylamide)
NVF	*N*-vinylformamide
PAAc	poly(acrylic acid)
PAM	poly(acrylamide-*co*-(3-acrylamidopropyl) trimethylammonium chloride)
PNVF	poly(*N*-vinylformamide)
PSA	poly(sodium acrylate)
PVAm	poly(vinylamine)
Q_{eq}	degree of swelling at equilibrium
RD	recycle delay

RO	reverse osmosis
SAP	superabsorbent polymer
SR	saturation recovery
TD NMR	time-domain NMR
TEMED	*N,N,N′,N′*-tetramethylethane-1,2-diamine
VAm	vinylamine

SYMBOLS

β	stretching parameter
C_0	monomer concentration (wt%)
Ca	capillary number
CV	coefficient of variation
D	diffusion coefficient ($m^2\,s^{-1}$)
DC	degree of crosslinking (mol%)
D_{dry}	dry particle diameter (m)
DI	degree of ionization (mol%)
D_{res}	residual dipolar coupling (Hz)
f	crosslink functionality
G'	elastic modulus (Pa)
G''	loss modulus (Pa)
G'_{max}	elastic plateau modulus (Pa)
γ_0	shear strain (%)
GM	geometric mean
$\hbar$	reduced Planck constant (J s)
I_{DQ}	double quantum signal intensity
I_{nDQ}	normalized double quantum signal intensity
I_{poly}	normalized polymer signal intensity
I_{ref}	double quantum reference signal intensity

I_{solv}	residual solvent signal intensity
kT	thermal energy (J)
λ_{B}	Bjerrum length (m)
λ_{D}	Debye length (m)
M_{c}	molecular weight between crosslinks ($\text{g}\,\text{mol}^{-1}$)
ν	number of network strands
ν_2	polymer volume fraction
ω_{L}	Larmor frequency (Hz)
ϕ_{shell}	degree of surface-crosslinking (vol%)
Q_{eq}	equilibrium swelling capacity
Re	Reynolds number
τ	recovery delay (s)
τ_{DQ}	double quantum evolution time (s)
τ_{echo}	echo time (s)
τ_{s}	swelling time (s)
θ_{NMR}	NMR gelation half time (s)
θ_{rheo}	rheological gelation half time (s)
ξ	cyclic rank

Part I

INTRODUCTION AND FUNDAMENTALS

1

RESEARCH OBJECTIVES AND OUTLINE

Highly swellable polyelectrolyte hydrogels, so-called superabsorbent polymers (SAPs), are hydrophilic polymer networks that contain charged monomer units along the polymer backbone [Buc98; Hor21]. Crosslinks inside the network can be formed by covalent bonds, polymer chain entanglements, hydrogen bonds, or electrostatic interactions [Kav98]. These crosslinking types vary in their bonding strength and the intriguing balance between them dictates application-relevant properties such as mechanical yield stress, permeability, and swelling capacity. The latter is particularly important for SAPs, which can absorb high amounts of solvent, up to a thousand times their own weight [QP11].

Poly(sodium acrylate) (PSA) is the most prominent SAP exhibiting an annual global production of ≈ 2 million metric tons [Cha21]. It is widely used as absorbent in disposable hygiene products with diapers claiming 74 % of the market [Cha21]. Other non-hygienic applications are as absorbent in wastewater treatments [Pak18a], as controlled-release systems of fertilizers in agriculture [Beh20], as hydration additive in cement-based materials [He19], and as sealing material in electric cables [ZM10]. Recent studies explored the use of PSA as a separation medium for the membrane-free desalination of salt water to overcome typical maintenance costs of membrane desalination techniques, such as reverse osmosis (RO), that arise from biofouling and clogging [Höp10; Are17a; Are19a].

The fundamental physical principle that enables the use of SAPs for desalination is the Gibbs–Donnan equilibrium, which describes partitioning of salt ions between a surrounding solution and a gel phase [Don32; Kat55]. The Gibbs-Donnan theory was originally developed to predict the electric potential along semipermeable membranes, such as dialysis and cell membranes. Low molecular weight ions, such as Na^+ and Cl^-, can permeate the cell membrane whereas large, charged protein structures and their counterions are impermeates located inside the cell. Owing to the covalently crosslinked network structure, SAPs act similarly as semipermeable membranes. When a SAP is surrounded by salt water, Na^+ and Cl^- diffuse into the SAP on average as ion pairs to satisfy electroneutrality. Presuming that Na^+ is the counterion of the polyelectrolyte, the counterion concentration gradient from the gel phase towards the surrounding solution counterbalances the diffusion of Na^+ and Cl^- ion pairs, as illustrated in Figure 1.1. As a result, the concentration of permeate ions (i. e., mobile ions) is always

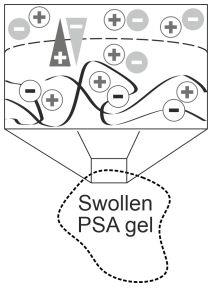

Figure 1.1: Asymmetric salt ion distribution leads to the Gibbs-Donnan equilibrium.

less inside the gel compared to the surrounding solution, leading to the so-called salt rejection [Höp10].

The strength of salt rejection increases with higher charge density of the SAP. Consequently, stepwise deswelling of swollen SAPs, for instance, induced by mechanical force or temperature, continuously increases salt rejection. This phenomenon has been exploited for an alternative membrane-free desalination method of salt solutions [Höp10; Ali15; Jan21]. Previous desalination attempts, relied on PSA based SAPs due to their high availability and rather low costs. However, PSA exhibits insignificant swelling capacities in seawater due to electrostatic interactions between the negatively charged polymer backbone and divalent cations, such as Mg^{2+} and Ca^{2+} [Horo1; Mus21]. Consequently, previous approaches have only used NaCl solutions as a proof of concept. Limited information is known on the swelling capacities of cationic SAPs in seawater and their use as separation medium in the desalination. Cationic SAPs do not exhibit attractive electrostatic interactions with divalent cations, and therefore, should have higher swelling capacities in seawater, overcoming thereby the aforementioned limitation of PSA based SAPs.

1. Research objective: designing cationic SAPs

This dissertation aims to synthesize two cationic SAP model systems with distinct functional groups to test the hypothesis that cationic SAPs exhibit higher swelling capacities in seawater. The acrylamide derivative (3-acrylamidopropyl) trimethylammonium chloride (APTAC) containing a cationic quaternary ammonium moiety serves as the charged repeating unit of the first model system. Vinylamine (VAm), which forms cationic ammonium groups at pH < 11 [Pel14], is the repeating unit of the second model system. SAPs from APTAC were synthesized according to the standard procedure, an aqueous free radical crosslinking copolymerization using *N*,*N*′-methylenebis(acrylamide) (MBA) as a crosslinker and acrylamide as a co-monomer. The formed SAP is referred to as PAM. APTAC is commercially available, which allows for rather simple up-scaling of the synthesis to ensure multigram scale desalination experiments. Figure 1.2 shows the chemical structure of the charged polymer repeating unit of both model systems. SAPs from VAm were prepared by acidic hydrolysis of *N*-vinylformamide (NVF) precursor hydrogels. In addition, a droplet-based microfluidic technique was used to fabricate monodisperse, spherical VAm SAPs. In contrast to the nonreactive quaternary ammonium group, the presence of highly reactive amine groups in VAm based SAPs enable facile postmodification reactions.

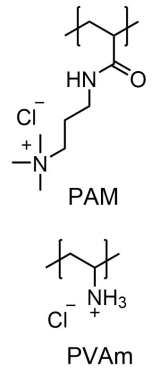

Figure 1.2: Cationic repeating units of the SAP model systems.

Despite numerous synthetic advances in SAP preparation and their industrial relevance, developing a consistent understanding of the impact of synthesis parameters on macroscopic properties, such as mechanical strength and swelling capacity, remains a longstanding challenge in SAP research [Wan16; Gu19]. The main factor preventing rational microscopic-macroscopic correlations is the multi-length scale

structural complexity of SAPs including functionality of crosslinks (< 1 nm), topological network defects ($1 - 10$ nm), and crosslinking density heterogeneity, so-called spatial inhomogeneity ($10 - 100$ nm) [Sei17b]. Topological network defects can be studied by time-domain NMR relaxometry (TD NMR), a non-invasive method that quantifies local mobility of polymer chains. This dissertation elucidates the impact of synthesis parameters on the distribution of local polymer chain mobility from which the extent of topological defects can be inferred. Narrow mobility distributions are characteristic for a homogeneous network whereas high amounts of topological defects lead to broad mobility distributions. In addition, this study develops a new SAP characterization method that can perform simultaneous rheological and TD NMR experiments. This Rheo-NMR device enables the direct correlation of mechanical properties with the nanoscopic network structure.

2. Research objective: advancing NMR based SAP characterization

This dissertation contributes to our understanding of the synthetic and physical principles dictating swelling behavior of SAPs in seawater as well as the intriguing relationship between mechanical properties and molecular dynamics of polymer gels. The latter advances the development of characterization methods that are able to measure mechanical properties of soft matter non-invasively. This dissertation further expands the fields of SAP application towards seawater desalination. Yet, the seawater applications addressed in this dissertation are considered as proof of concepts and should not be compared to industrially established, highly efficient alternatives but should be rather used as a guide for future developments. The outline of this dissertation is as follows.

Contributions and limitations

Chapter outline

Chapter 2, p. 7 introduces the fundamentals of polymer gels, including a classification and a historical perspective on the research. As the term polymer gel is not used consistently throughout the scientific literature, some phenomenological approaches to define polymer gels are discussed. Particular attention is paid to the structural complexity, introducing various characterization techniques for different length scales. This chapter concludes with the underlying physical principles of superabsorbency.

Chapter 3, p. 19 reviews the basics and applications of NMR relaxometry techniques. Quantum mechanical principles of NMR measurements and the relationship between NMR relaxation phenomena and molecular motions are discussed. This chapter closes with a consideration of common NMR pulse sequences and their application in polymer gel research.

Chapter 4, p. 31 discusses the synthesis of the proposed cationic SAP model systems. Synthetic parameters used throughout this dissertation, such as the degree of crosslinking *DC* are introduced. Particular attention is devoted to the description of the droplet-based microfluidic technique used to prepare spherical, monodisperse SAP particles.

Chapter 5, p. 41 explains water absorbency measurements of the synthesized cationic SAPs. The influence of synthetic parameters on the swelling behavior is assessed. The salt and seawater concentration dependency of the equilibrium swelling capacity is described with a consideration of theoretical predictions.

Chapter 6, p. 53 explores the application of time-domain NMR relaxometry for network structure analysis in SAPs. A mathematical algorithm used for the regularized inversion of TD NMR data sets is introduced. Data acquisition and evaluation of ^{1}H residual dipolar coupling measurements are discussed. This chapter concludes with the non-invasive, dynamic assessment of hydrogel core-shell topologies using T_2 relaxation curves.

Chapter 7, p. 71 elucidates the use of a novel portable TD NMR attachment for rheometers to obtain additional molecular insights into the gelation process of hydrogels. Technical details and data acquisition of this Rheo-NMR method are discussed. The direct time-dependent correlation of the elastic modulus with T_2 relaxation times and the polymer concentration are demonstrated with a consideration of theoretical predictions based on the tube model of semi-dilute entangled polymer solutions.

Chapter 8, p. 87 discusses two relevant seawater applications of the synthesized cationic SAPs. The membrane-free desalination of seawater and the estimation of the desalination efficiency are explained. A mechanochemical SAP based approach to harness sustainable mechanical energy from natural salinity gradients in the osmotic engine is explored. Further technical improvements of both applications are proposed.

2 POLYMER GELS

2.1 CLASSIFICATION AND HISTORICAL PERSPECTIVES

The field of polymer gels is an active, multidisciplinary area of research where scientists from different backgrounds work on several different types of gels. Providing a clear, consistent definition throughout multiple research disciplines remains challenging [Alm93]. This effort is further hindered by the large number of varying terms for gels that have been introduced in recent literature, such as xerogel [Lee09], aerogel [Koe12], microgel [Sau99], nanogel [Yin20], pseudo-gel [Kes04], and double network gel [Non15].

A first systematic description of structural characteristics of uncharged polymer gels were proposed by Flory and Stockmayer during their research efforts to develop a universal theory of polymer gelation [Flo42a; Sto44]. Statistical arguments formed the basis of their definitions, such as connectedness, three-dimensional and infinite network structure. Flory later subdivided gels into the following types: 1) well-ordered lamellar structures, 2) completely disordered covalent polymer networks, 3) polymer networks formed through physical aggregation, which are predominantly disordered with regions of local order, and 4) disordered particulates [Flo74]. He further emphasized that the solid-like behavior of gels is the most universal characteristic of a gel that exhibit a predominant, yet low elastic response during deformation [Flo74]. This statement, however, does not contain information about the number of components constituting a gel. Consequently, Ferry further specified this classification by defining gels as substantially diluted systems which exhibit no steady-state flow, emphasizing thereby that gels are crosslinked solutions where crosslinks are made by covalent bonds or morphologies, such as crystallites, excluding thereby viscoelastic liquids [Fer80]. The rigidity of these gels can be expressed by the frequency-independent elastic modulus [Fer80]. Burchard and Ross-Murphy noted that Ferry's definition may be overrestricted as it requires gels to be a true solid. They argue that many systems such as structured fluids behave as typical gels, but lack an equilibrium elastic modulus [Bur90]. They adjust Ferry's definition, stating that gels either posses a plateau in the elastic modulus over a wide range of frequencies or can be converted to viscoelastic solids under appropriate conditions.

Based on the aforementioned definitions of Flory, Ferry, and Burchard and Ross-Murphy, recent phenomenological definitions of polymer gels specify the following characteristics: 1) At least two com-

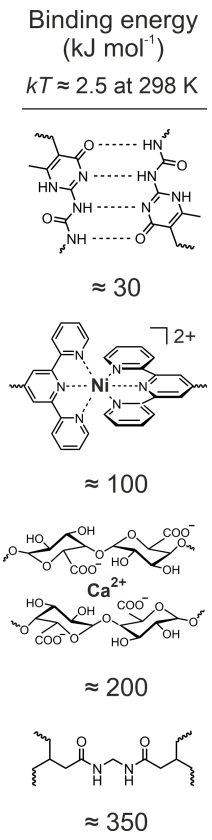

Figure 2.1: Binding energies of different crosslinks in polymer gels [Pot20].

ponents one of which is a liquid in substantial quantity comprise a gel. 2) Soft, solid-like or solid gels exhibit a pronounced plateau of the elastic modulus $G'(\omega)$, extending to frequencies at least on the order of 6.3 rad s^{-1} (i. e., one hertz), and a loss modulus $G''(\omega)$ that is substantially smaller than the elastic modulus in the plateau region [Alm93; Kav98; Rog08]. The authors were not able to find an upper limit for the term soft as it has different meanings in varying scientific fields. However, highly rigid materials with a mechanical modulus greater 10^8 Pa do not resemble characteristic gel features but rather that of glassy polymers, and therefore, were excluded from the definition.

Besides the general mechanical classifications, polymer gels can be subdivided into two main groups based on the crosslinking type, namely covalently crosslinked and physical gels [Kav98; Rog08; Pat22]. Covalently crosslinked gels are typically formed by free radical polymerization of a monomer and a divinyl crosslinker. They are macromolecules with a nominally infinite molecular weight that exhibit superior structural integrity in their most swollen state. The covalent crosslinks lead to high mechanical strengths but poor processability and lack of stimuli-responsiveness. Crosslinking density can be controlled by the concentration of crosslinker, which, however, can distinctly affect the homogeneity of the network [Nag96].

In contrast to covalent gels, physical interactions, such as electrostatic attractions, and hydrogen bonds, form crosslinks in physical gels. The binding energy of physical crosslinks is on the order of the thermal energy kT, and therefore, temperature can be used to break crosslinks, providing superior processability of the formed gels [Pat22]. Figure 2.1 shows some common crosslink types and their respective binding energy. The presence of dynamic physical crosslinks, however, complicates the physical description of the network as the number and position of crosslinks constantly fluctuates as a function of time and temperature [Kav98]. Consequently, predicting mechanical properties based on the gel composition remains a longstanding challenge in physical gel research.

First generation hydrogels

This dissertation predominantly discusses hydrogels, a specific type of polymer gels that can absorb substantial amounts of water without dissolution. The term hydrogel for water-swollen macromolecular networks appeared for the first in the groundbreaking work of Wichterle and Lim, who studied the use of poly(2-hydroxyethyl methacrylate) (PHEMA) gels as soft contact lenses [Wic60]. In the following decades, research of this so-called first generation hydrogels were limited to rather simple chemically crosslinked networks, mainly prepared by aqueous solution polymerization of monomers. Subsequently, hydrogel formation of synthetic poly(vinyl alcohol) and poly(ethylene glycol) polymer solutions received considerable attention due to their high biocompatibility and facile introduction of crosslinks using γ

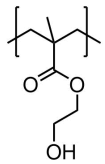

Figure 2.2: Repeating unit of PHEMA.

irradiation and reactive bi-functional crosslinker, such as dialdehydes [Pep80; Str96].

Second generation hydrogels

The innovative work of Katchalsky on the possibility of transferring chemical energy, induced, for instance, by pH and salt concentration variations, into mechanical work in the so-called mechanochemical engines inspired the research of the second generation hydrogels [Ste66]. The presence of physical crosslinks in these stimuli-responsive hydrogels depends on external parameters, such as temperature and pH values. An example of temperature sensitive hydrogels are aqueous solutions of poly(ethylene glycol) (PEG) – poly(propylene glycol) (PPG) – poly(ethylene glycol (PEG) triblock copolymers, commercially known as Pluronics (BASF) [CC81]. A phase transition from the liquid to the gel state can be triggered at low temperatures ($< 5\,^{\circ}\mathrm{C}$) when the concentration is above the critical gel concentration ($> 15\,\mathrm{wt\%}$) [Len87]. Other temperature responsive hydrogels are based on poly(*N*-isopropylacrylamide) (PNIPAM) that exhibit a rapid and reversible phase transition at $32\,^{\circ}\mathrm{C}$ due to an enhancement of hydrophobic interactions between isopropyl groups of the monomer unit [Wu92]. As the phase transition is close to the the body temperature, initial research was particularity aimed to use PNIPAM for biomedical applications [Hof12].

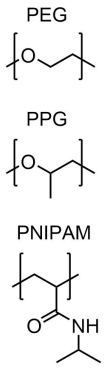

Figure 2.3: Repeating units of PEG, PPG, and PNIPAM.

Third generation hydrogels

The exploration of unique crosslinking chemistry including metal – ligand coordination, peptide interactions, and stereocomplexation sparked the development of the third generation hydrogels [Buw14]. Polymer stereocomplexation describes the interaction between at least two stereoregular polymers interlocking with each other, forming thereby a composite with altered mechanical properties. Stereocomplexation has been shown between enantiomeric poly(lactides) with opposite chirality [Ika87]. Poly(L-lactides) forms a left-handed helix while poly(D-lactide) forms a right-handed one. Van der Waals forces between those helices drive the formation of dense crystalline packing that functions as a physical crosslinking point [Fuk06]. The use of cyclic oligosaccharides, such as cyclodextrins, for the formation of physical gels through guest - host interactions have been extensively explored [Li94]. Large polymeric guests, such as poly(ethylene glycol), threads into the cyclodextrin host. Subsequent aggregation of these polypseudorotaxanes forms a supramolecular hydrogel. The first metallohydrogel contained reversible crosslinks based on bipyridine functionalized poly(oxazoline) and Co^{2+} metal-ligand coordination chemistry [Chu93].

Recent hydrogel breakthroughs

Recent design principles aim to introduce superior mechanical stability and self-strengthening properties or multi-stimuli responsive properties into the hydrogels. The exploration of different hydrogel architectures, such as interpenetrating networks, has led to unprecedented improvements of the fracture resistance (failure tensile stress of up to 10 MPa at strains of up to 2000 %) and mechanical strength (elastic

modulus up to 1 MPa) of hydrogels containing 90 wt% water [Gon10; Che15; Non15]. Great effort has been devoted to the development of the double network architecture, which consists of a highly crosslinked, rigid polyelectrolyte embedded into a loosely crosslinked, ductile neutral polymer matrix, mimicking thereby biological load-bearing tissue, such as cartilage [Gon03]. Double network hydrogels are typically synthesized by a two-step process. First, a tightly crosslinked polyelectrolyte single network is synthesized, which is subsequently immersed in an aqueous monomer solution of the second network [Gon03]. Subsequent photo-induced polymerization of the monomer solution yields the double network. The combination of poly(2-acrylamido-2-methyl-1-propanesulfonic acid) and poly(acrylamide) has been identified as the best performing double network [Gon03]. Other recent advances in hydrogel research include the development of composite hydrogels, where inorganic molecules, such as calcium phosphate, are incorporated into the network to enhance mechanical properties and biocompatibility.

Although the high material complexity of recent hydrogel compositions leads to substantial improvements of mechanical properties, it distinctly complicates any rational physical description of these intriguing properties. The understanding of structure-properties relationships is further restricted by the intrinsic multi-length scale complexity of hydrogels that is subject of the next chapter.

2.2 MULTI LENGTH-SCALE COMPLEXITY OF POLYMER GELS

The development of a consistent understanding of the interplay between molecular and macroscopic properties in hydrogels remains a longstanding challenge, complicating thereby a rational design of hydrogels for desired applications. The microscopic topology of the polymer network predominantly dictates mechanical properties [Di 15; Gu19]. Depending on the reactions conditions, complex network topologies over multiple length scales can be formed [Sei17b]. Therefore, a description of the polymer network topology requires at least three distinct length scales: < 10 nm, $10 - 100$ nm, and > 100 nm.

Branch functionality

As crosslinks typically consist of few chemical bonds, the branch functionality of crosslinks is a key sub-nanometer topological feature that governs mechanical properties. Branch functionality f can be directly derived from the chemical structure of precursors used to synthesize the hydrogel. For instance, commonly used divinyl crosslinker yield branch functionalities equal to four. However, a full conversion of the crosslinker is never reached, and therefore, the effective branch functionality can be reduced. The experimental quantification of unreacted functionalities is not trivial, which mainly relies on spectroscopic techniques, such as infrared spectroscopy.

1–10 nm length scale

At a length scale in the range $1 - 10$ nm, topological features involve the presence of one or multiple polymer chains. Unreacted chain ends can lead to dangling ends, whereas loops can be formed from intramolecular crosslinking reactions, as illustrated in Figure 2.4. These local inhomogeneities distinctly reduce the elastic properties of the hydrogel, yet their experimental quantification is challenging as they are chemically not distinguishable from elastic polymer chains between two crosslinks. A recent network disassembly spectrometry approach quantifies the amount and type of loops by systemically degrading chemically labeled networks and analyzing the degradation products [Zho16]. The degradation fingerprint of the networks has been used to correct the theoretical elastic modulus by considering the amount and types of loops [Zho16]. This has led to an optimized model for the elastic shear modulus of hydrogels, denoted as the real elastic network theory [Lin19]. It has been further shown that the systematic introduction of loops can significantly improve fracture resistance. Crack growth is reduced, since second order loops have to rapture twice to effectively cut elastic chains [Aro20]. Double quantum NMR (DQ NMR) measurements are another common technique that has been used to assess the amount of local defects in elastomers [Saa12; Saa18]. In this method, the fraction of elastic network polymer chains is distinguished from the fraction of topological defects based on subtle differences in the chain dynamics. The resulting DQ NMR signals can be evaluated in terms of multi-exponential fits that resemble dynamically different fractions [Cha12a]. This dissertation uses the low-field DQ NMR method to characterize the synthesized charged hydrogels, which is discussed in more detail in Section 3.3, p. 24.

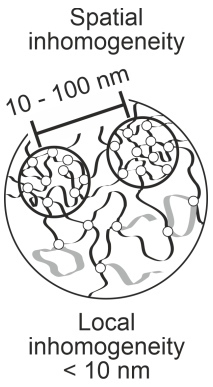

Figure 2.4: Nanoscopic topological defects in polymer gels.

10–100 nm length scale

At length scales in the range $10 - 100$ nm, mechanical properties are primarily dictated by spatial inhomogeneities, which result from thermal concentration fluctuations of the monomer solution at the gel point, leading to a heterogeneous distribution of crosslinking density. This heterogeneities have been further attributed to different reactivities of monomer and crosslinker, causing an initial growth of local nanogel clusters that subsequently interconnect [Oka94; Sei17b]. Conventional scattering techniques, such as dynamic light and small-angle neutron scattering, can be used to semi-quantitatively monitor spatial inhomogeneities [Sei17c].

Particle shape and size

Application-relevant properties, such as swelling capacity and absorption kinetics, of macroscopic particles with dry particle diameters on the order of hundreds of micrometers are mainly governed by their size, size distribution, and shape. The combination of a broad size distribution and an asymmetric particle shape promotes gel-blocking, a phenomenon that limits swelling kinetics and absorbency under load [Buc98]. Gel-blocking describes a swelling hindrance of SAP particles that are stacked in a confined space. SAPs of the first layers start to swell upon adding solution, reducing thereby any gaps between

particles. As a result, pathways for additional solution to other dry particles beneath the initial layers are blocked. It has been shown that surface-crosslinking and monodisperse, spherical particles can significantly reduce gel-blocking [Jan20]. Figure 2.5 illustrates the important design principles of SAPs at different length-scales.

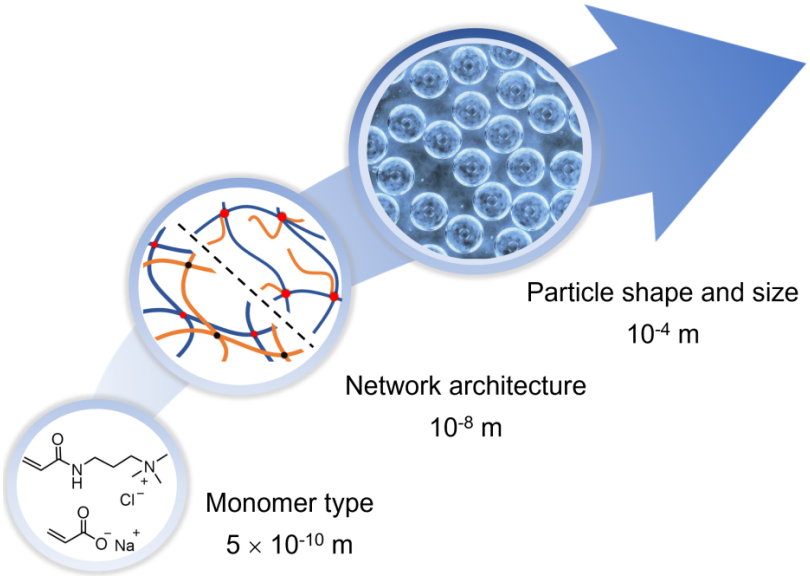

Figure 2.5: Designing SAPs requires the consideration of at least three different length scales.

Designing SAPs

Tailoring SAPs for the desired application requires the consideration of multiple length-scales. The chemical structure of the monomer units can, for instance, affect the electrostatic interactions with multivalent ions, and therefore, influence the swelling capacity [Hor21]. Altering hydrophilic and hydrophobic interactions between monomers can be used to introduce stimuli-responsive and self-strengthening properties in SAPs [Pot20]. Incorporating a complex network architecture, such as an interpenetrating network, into the SAPs can profoundly improve mechanical properties, such as fracture resistance, at the swollen state [Gon10]. On the macroscopic scale with dry particle sizes on the order of hundreds of micrometers, the preparation of monodisperse, spherical particles reduces drastically gel-blocking, increasing thereby swelling capacity and swelling kinetics under load [Jan20].

2.3 SWELLING THEORY OF SUPERABSORBENT POLYMERS

The high swelling capacity of SAPs is certainly their most characteristic property. Flow and convective mechanisms drive the swelling behavior of traditional absorbents, such as cotton and sponges, whereas the swelling of SAPs is predominantly a diffusion process. In traditional absorbents, open space in form of pores serves as a reservoir for water. When the pores are connected throughout the material, liquid can be transported. Principal factors affecting the flow of liquid through a porous medium can be described by Darcy's law. This general empirical relationship connects the steady volumetric flow rate $\mathrm{d}V/\mathrm{d}t$ in one direction to the specific permeability κ_D of the material by

$$\frac{\mathrm{d}V}{\mathrm{d}t} = -\frac{\kappa_\mathrm{D} A \Delta P}{\mu L}, \tag{2.1}$$

where A is the cross-sectional area of the medium, L is the length of the medium, μ is the dynamic viscosity of the fluid, and ΔP is the pressure difference driving the flow [Whi86]. κ_D of the medium can be specified by the void fraction and extent of connectedness of open space. Structural features affecting permeability are mainly limited to an effective pore size diameter based on diameters of fibers and particles that make up the absorbent. Hydrostatic and capillary forces can further drive the flow through porous media. The latter are particularly crucial in absorbent materials as capillary forces facilitate the initial wicking process by transporting liquid from the surface into the dry absorbent material. Considering a cylindrical tube with radius r_0, the maximum height of liquid h induced by capillary action can be determined from the force balance between the weight mg and surface tension γ of the liquid column given by

$$h = \frac{2\gamma\cos(\theta)}{\rho g r_0}, \tag{2.2}$$

where θ is the contact angle of liquid to the tube wall, ρ is the mass density, and $g_0 = 9.81\ \mathrm{m\,s^{-2}}$ is the standard gravity constant, as illustrated in Figure 2.6 [Geno4]. Consequently, capillary rise is inversely proportional to the tube radius.

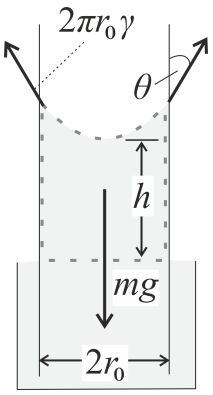

Figure 2.6: Illustration of the capillary effect.

In contrast, the absorption mechanism of SAPs is based on diffusion, and therefore, the random statistical motion of molecules in space towards regions with lower concentration. Water molecules spread out from the surface into the SAPs particles because the concentration is lower inside the particles. Simultaneously, polymer chains of the SAP network move in opposite direction, creating additional volume for the water molecules. Polymer chains are larger than water molecules, and diffuse slower. Moreover, in SAPs polymer chains are interconnected through covalent bonds, enforcing thereby cooperative movement

which further reduces diffusion. Consequently, the slow diffusion of polymer chains is the rate-limiting process during swelling. The absorption process is ultimately counterbalanced by elastic forces of the elongated polymer network when the equilibrium swelling capacity is reached.

The basic model of the equilibrium swelling capacity originated in the pioneering work of Flory and Rehner [Flo43]. The Flory-Rehner theory and its modern adaptation the Flory-Erman model describe the equilibrium swelling state by means of thermodynamic interactions of free energies between different components of the network. Free energies of the gel can be expressed by the chemical potentials μ_{i} of the systems. For compressible gels at constant pressure and temperature, the change in Gibb's energy $\mathrm{d}G_{T,p}$ is given by

$$\mathrm{d}G_{T,p} = \sum_i \mu_i \, \mathrm{d}n_i \ , \tag{2.3}$$

where n_i is the amount in moles of each component i in the system. Dividing the chemical potentials by the molar volume $V_{\mathrm{m},i}$ of each component, yields the osmotic pressure

$$\Pi = -\frac{\mu_i - \mu_i^0}{V_{\mathrm{m},i}} \, , \tag{2.4}$$

where μ_i^0 is the chemical potential at the reference state. To account for the intriguing balance between different competing thermodynamic forces, the total osmotic pressure Π_{tot} can be expressed as the sum

$$\Pi_{\mathrm{tot}} = \Pi_{\mathrm{mix}} + \Pi_{\mathrm{el}} + \Pi_{\mathrm{ion}} \, , \tag{2.5}$$

where Π_{mix}, Π_{el}, and Π_{ion} are pressure contributions arising from polymer and solvent mixing, elastic deformations of the network, and the presence of counter ions, respectively. This three principle components are based on the Flory-Huggins theory of mixing, the Flory-Erman description of the elastic response, and the Donnan equilibrium added by Hooper and coworkers to consider ionic contributions [Buc98]. According to the theories, for a fully swollen polymer network, the osmotic pressure is defined as

$$\begin{aligned} \Pi_{\mathrm{tot}} = & -\frac{RT}{V_{\mathrm{m,solv}}}[\ln(1-\nu_2) + \nu_2 + \chi\nu_2^2] \\ & - RT\nu_2^{1/3}\left(\frac{\xi}{V_0}\right)\left[1 + \left(\frac{\mu_{\mathrm{e}}}{\xi}\right)K(\nu_2)\right] \\ & + RT\sum_j^N (c_j^{\mathrm{gel}} - c_j^{\mathrm{ext}}) \, , \end{aligned} \tag{2.6}$$

where $V_{\mathrm{m,solv}}$ is the molar volume of solvent ($\approx 18\ \mathrm{cm^3\,mol^{-1}}$ for water), ν_2 is the volume fraction of polymer, typically determined as the

inverse of the equilibrium swelling capacity, χ is the polymer-solvent interaction parameter, μ_e is the molar number of crosslinks, ξ is the cyclic rank of the network, and $K(\nu_2)$ is a function that describes the magnitude of constraints on crosslinks, calculated from an entanglement parameter κ [Erm97]. Ionic contributions are included by the concentration of mobile ions in the gel phase c_j^{gel}, and the concentration of mobile ions in the liquid phase c_j^{ext}. N is the total amount of mobile ions in the system. The equilibrium state is reached when the sum of contributions equals zero.

Mixing contribution

The Flory-Huggins theory describes the mixing free energy based on a lattice model incorporating a random distribution of polymer chains and solvent molecules on the sites, as illustrated in Figure 2.7 [Flo42b]. The entropy is given by the number of possible configurations whereas the enthalpic contribution of mixing is described by the interaction parameter χ, a dimensionless quantity normalized to kT that is on the order of 0.5. χ can be used as a measure of solvent quality. At values > 0.5 demixing is favored, which is characteristic for a poor solvent. Despite being developed for uncrosslinked polymer chains, the Flory-Huggins formalism holds for network swelling, yet has to be refined for more complex systems where, for instance, hydrogen bonds are present. Since χ resembles the average noncovalent and nonionic nature between polymer and solvent, it does not, for instance, account for hydrogen bonds between polymer chains. Prange and coworkers reported an extension of the conventional lattice theory that accounts for strong specific interactions, such as hydrogen bonds, by using three interaction parameters [Pra89]. Moreover, structural and chemical influences of crosslinking can affect the affinity of polymer to solvent. McKenna and Horkay found, using a combination of swelling and mechanical experiments, that χ differs in crosslinked poly(vinyl alcohol) networks compared to uncrosslinked poly(vinyl alcohol) chains [McK94]. A conclusive description of the mechanisms driving this difference in χ, however, has yet to be found and confirmed with other hydrogel systems.

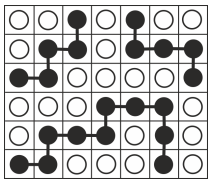

Figure 2.7: Thermodynamic lattice model for polymer - solvent mixing [Rub03].

Elastic contribution

When hydrogels swell and imbibe water, the network chains extend and pull on each other creating an elastic response. The underlying mechanism of rubber elasticity has primarily entropic origins. During extension, coiled polymer chains reduce their number of available conformations, decreasing thereby the entropy, which generates an elastic force counterbalancing the extension. In the classical Flory-Rehner description of swelling, elastic contributions were derived from an affine deformation of the network, since it was initially developed for solvent-free rubber networks. In the affine model, all crosslinks are fixed in space and are displayed isotropically with respect to the macroscopic deformation (i. e., swelling) [Flo77]. In real networks, crosslinks are attached to other crosslinks through polymer chains, and therefore, they can fluctuate around their average positions. These

Hydrogels behave as phantom-like networks.

fluctuations reduce the net free energy of the system as some of the macroscopic deformation leads to changes of the relative position of crosslinks. As a result, polymer chains extend lesser than the macroscopic deformation. These fluctuations of crosslinks were incorporated in the phantom network model developed by James and Guth [Jam53]. The second term of Equation 2.6, p. 14, the Flory-Erman description, incorporates both the affine and phantom networks concepts by introducing a function $K(\nu_2)$ that enables a transition from the affine to the phantom model by constraining the motion of crosslinks through chain entanglement effect via the parameter κ in the so-called constraint junction model [Erm97]. In the limit of vanishing constraints $\kappa \to 0$, the presence of network chains do not constraint the fluctuation of junctions. Consequently, entanglements are excluded from the model. The phantom model is more appropriate for highly swollen networks as the low polymer volume fraction, typically $< 20\,\mathrm{wt\%}$, facilitates fluctuations of crosslinks due to the low concentration of entanglement points. An important result of the phantom model is that the elasticity of the network scales with the cyclic rank

$$\xi = (1 - \frac{2}{f})\nu\,, \tag{2.7}$$

instead of the total number of network strands ν. f is the functionality of crosslinks. The cyclic rank has been used in graph theory and defines the number of chains that must be cut to form an acyclic network, as illustrated in Figure 2.8.

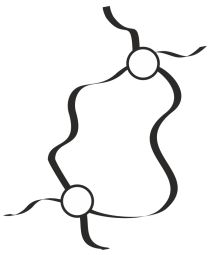

Figure 2.8: Cyclic rank ξ for a network with functionality f and number of network strands ν.

In SAPs, the polyelectrolyte backbone consists of charges including counter ions, which enhance the equilibrium swelling capacity due to increasing osmotic pressure differences between the polymer network and surrounding solution [Phi11]. These ionic effects are considered in the third term of Equation 2.6, p. 14 in terms of the Gibbs-Donnan equilibrium. Concentration of ions in the gel phase c_j^{gel} include the counterions of the polyelectrolyte and mobile ions that can move freely between the external solution and the gel. The gel behaves as a semipermeable membrane in an osmotic experiment. The difference of mobile ion concentration between the gel phase and the surrounding liquid arises from the requirement to satisfy electroneutrality given by

$$c_{\mathrm{Na}^+}^{\mathrm{gel}} c_{\mathrm{Cl}^-}^{\mathrm{gel}} = c_{\mathrm{Na}^+}^{\mathrm{ext}} c_{\mathrm{Cl}^-}^{\mathrm{ext}} \tag{2.8}$$

for a monovalent NaCl solution. Presuming an infinite bath of the external solution, the total salt concentration of the liquid is $c^{\mathrm{ext}} = c_{\mathrm{Na}^+}^{\mathrm{ext}} = c_{\mathrm{Cl}^-}^{\mathrm{ext}}$. During the swelling of PSA hydrogels in a NaCl solution, both Na^+ and Cl^- diffuse into the gel phase. Consequently, the sum of Cl^- ions entering the gel, thereby dragging Na^+ with them, is $c_{\mathrm{Cl}^-}^{\mathrm{gel}}$.

Ionic contribution

PSA has Na^+ counter ions, and therefore, the total concentration of Na^+ ions in the gel phase is given by

$$c^{\text{gel}}_{Na^+} = c^{\text{gel}}_{Cl^-} + \frac{i\nu_2}{V_{\text{m,mon}}}, \tag{2.9}$$

where i is the degree of ionization and $V_{\text{m,mon}}$ is the molar volume of the monomer. Plugging Equation 2.9 into the third term of Equation 2.6, p. 14 yields the ionic contribution of the osmotic pressure

$$\Pi_{\text{ion}} = 2RT\{[(c^{\text{ext}})^2 + (\frac{i\nu_2}{2V_{\text{m,mon}}})^2]^{1/2} - c^{\text{ext}}\} \tag{2.10}$$

for PSA based SAPs [BP91; Horoo]. Note that this description is only valid for small ion concentrations where electrostatic repulsions between monomer units are neglected and the activity of ions is equivalent in the gel phase and external solution.

3

NMR RELAXOMETRY

3.1 ENERGY EXCHANGES OF A NUCLEUS IN A MAGNETIC FIELD

A fundamental result of the quantum mechanical description of atomic nuclei is that protons and neutrons posses a spin as an intrinsic quantum property. The spin describes the intrinsic angular momentum of nuclei, analogue to the classical description of a spinning sphere. The total net spin, however, does not result from spinning but rather from the intriguing interaction between quarks, the building blocks of protons and neutrons that are hold together by gluons [Levo8]. The spin $\hat{I}$ is a quantum mechanical operator where the eigenvalue of $\hat{I}^2$ is $I(I+1)$ with I the spin quantum number [Blüoo].

The presence of a spin depends on the number of protons and neutrons inside the nucleus and can be either integer or half-integer multiples of the reduced Planck constant $\hbar = 1.1 \times 10^{-34}$ J s. As a general rule, nuclei with an even number of protons and neutrons, such as ^{16}O and ^{12}C, have $I = 0$, nuclei with an even mass number have integer values, and nuclei with an odd mass number, such as ^{1}H have half integer values. The spin is quantized into $2I + 1$ possible orientations relative to an external magnet field in z direction. The orientations are expressed by the magnetic quantum number

$$m_I = -I, -I+1, ..., I-1, +I\,. \tag{3.1}$$

Correspondingly, a ^{1}H with $I = 1/2$ has two independent spin states with $m_I = +1/2$ and $-1/2$ relative to an external magnetic field B_z, as illustrated in Figure 3.1. The presence of a non-zero nuclear spin leads to a magnetic moment

$$\mu = \gamma\hbar(I(I+1))^{1/2}\,, \tag{3.2}$$

where γ is the gyromagnetic ratio ($\gamma/2\pi = 42.6$ MHz T^{-1} for a ^{1}H nucleus), a characteristic constant for every nucleus [Blü19]. Without an external magnetic field, all spin states are energetically equivalent. Along a strong magnetic field, however, the energy levels of the spin states split into two characteristic energy levels for a spin $-1/2$ nucleus, referred to as the Zeeman effect [Abr83]. The magnetic moment can align parallel or antiparallel to the external magnetic field, which are typically denoted as α and β states, respectively. Both spins precess with a characteristic angular Larmor frequency $\omega_L = \gamma B_z$ around B_z. The energy difference between these states is given by

$$\Delta E_m = E_\beta - E_\alpha = \gamma\hbar B_z\,. \tag{3.3}$$

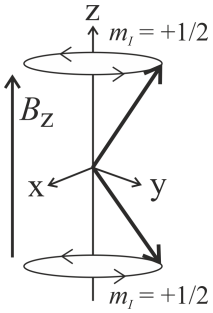

Figure 3.1: Spin states of a spin-1/2 nucleus in a static magnetic field B_z.

Irradiation of the spins with electromagnetic waves in the Larmor frequency induces transitions between the energy states. The relevant range of the proton resonance frequency is between the earth magnetic field $\approx$ 2 kHz, 50 µT and 1 GHz, 23.5 T.

The macroscopic net magnetization $\vec{M}_0$ for an ensemble of n nuclei is the sum of all individual magnetic moments μ_i according to

$$\vec{M}_0 = \sum_i^n \mu_\mathrm{i} \,. \tag{3.4}$$

The population between the ground energy state α and excited energy state β of a spin$-1/2$ ensemble follows the Boltzmann distribution

$$\frac{N_\beta}{N_\alpha} = \exp\left(-\frac{\Delta E_\mathrm{m}}{kT}\right) \approx 1 - \frac{\hbar\omega_\mathrm{L}}{kT} \,, \tag{3.5}$$

where kT is the thermal energy. The signal intensity of a NMR experiment increases as a function of the population difference, which determines the total net magnetization. N_β/N_α can be lowered by either reducing the temperature of the measurement or increasing ΔE_m. Modern high-field NMR spectrometers use superconducting permanent magnets with $B_\mathrm{z} = 10 - 20$ T, reaching a population difference only on the order of ppm for protons at room temperature.

3.2 RELAXATION PHENOMENA BASED ON MOLECULAR MOTION

NMR relaxation refers to processes in which the thermodynamic equilibrium magnetization M is restored after electromagnetic pulses perturbated the spin system. The equation of motions of the macroscopic magnetization vector were first described by Bloch, who identified that any magnetization component not parallel to the static magnetic field B experiences a torque $\tau = M \times B$ [Blo46]. Analogue to a spinning top in a gravitational field, these magnetization components precess around the direction of B. The change of magnetization in time is given by the Bloch equation

$$\frac{\mathrm{d}M}{\mathrm{d}t} = \gamma M(t) \times B_z(t) - \mathrm{R}[M(t) - M_0] \,, \tag{3.6}$$

where M_0 is the thermodynamic equilibrium value obeying the Curie law. The second term incorporates relaxation with the relaxation matrix

$$\mathrm{R} = \begin{pmatrix} 1/T_2 & 0 & 0 \\ 0 & 1/T_2 & 0 \\ 0 & 0 & 1/T_1 \end{pmatrix} . \tag{3.7}$$

where T_1 and T_2 are the longitudinal and transverse relaxation times, respectively. Accordingly, T_1 is the characteristic time constant of the

equilibrium magnetization build up parallel to the external magnetic field in z given by

$$M_z(t) = M_0(1 - \exp(-\frac{t}{T_1}))\,. \tag{3.8}$$

T_2 is the characteristic time constant of the magnetization decay orthogonal to the magnetic field given by

$$M_{x,y}(t) = M_{x,y}\exp(-\frac{t}{T_2})\,. \tag{3.9}$$

The presence of a finite transverse magnetization means that the ensemble of spins precess coherently around the external magnetic field. In NMR experiments, this motions induces a voltage (free induction decay) in a detector coil perpendicular to the static magnetic field. T_2 relaxation results from the presence of an inhomogenous magnetic field, which leads to a distribution of Larmor frequencies. Eventually, transverse magnetization fades due to destructive superposition of the progressively dephased spin coherences.

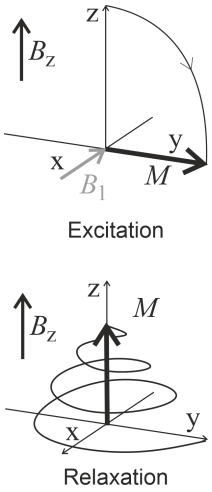

Figure 3.2: Relaxation of the magnetization according to the Bloch equations in a NMR experiment after excitation with a $\pi/2$ pulse.

The T_1 relaxation is an energetic exchange between the environment (lattice) and the excited nuclear spins, and therefore, it is often referred to as spin-lattice relaxation. The build up of the z magnetization component depends on the population difference between the degenerate spins states. Consequently, the energy exchange back to thermal equilibrium can be induced by local magnetic field fluctuations close to the Larmor frequency. Although both T_1 and T_2 relaxation processes are fundamentally different physical concepts, their magnitude can be related to magnetic field fluctuations. Since nuclear moments are physically located in molecules via ^{1}H, the statistical thermal molecular motion of molecules is the origin of these fluctuating fields responsible for dipolar relaxation.

Molecular motions cause local magnetic field fluctuations.

Fast molecular thermal motions include rotational reorientations and translational motion. In polymers, intramolecular motions, such as rotations around chemical bonds and segmental motions of the polymer backbone, can significantly affect relaxation processes. The combination of these motions can be expressed quantitatively by the rotational correlation time τ_c, the average time a molecule needs to rotate one radian. A relationship of τ_c to the bulk property viscosity of the surrounding medium can be described by the Stokes–Einstein–Debye theory of the liquid state [Bako4]. Presuming molecules as a spherical rigid body, τ_c is proportional to the viscosity by

$$\tau_c = \frac{4\pi a^3}{3kT}\,, \tag{3.10}$$

where a is the radius of the sphere and k the Boltzmann constant. Accordingly, τ_c increases advancing from small organic molecules ($\tau_c \leq 10^{-11}$ s) to polymer chains ($\tau_c \geq 10^{-9}$ s) in solution.

The BPP model

More precisely, τ_c can be derived from local field fluctuations by an autocorrelation function, connecting thereby molecular motions to nuclear NMR relaxation phenomena [Blo48; Red57]. Bloembergen, Purcell, and Pound derived in the so-called BPP model NMR relaxation from the autocorrelation function

$$G(\tau) = G_0 \exp\left(-\frac{|\tau|}{\tau_c}\right). \tag{3.11}$$

In accordance to the Wiener–Khinchin theorem, the Fourier transformation of $G(\tau)$ yields the frequency-dependent spectral density

$$J(\omega_L, \tau_c) = \frac{2\tau_c}{1+\omega_L^2\tau_c^2}, \tag{3.12}$$

which contains information about the magnitude of certain frequencies at varying τ_c.

Accounting for dipol-dipol interactions, the BPP model relates NMR relaxation times to the spectral density by

$$\frac{1}{T_1} = K_{1/2}\left[\frac{\tau_c}{1+\omega_L^2\tau_c^2} + \frac{4\tau_c}{1+4\omega_L^2\tau_c^2}\right] \tag{3.13}$$

and

$$\frac{1}{T_2} = \frac{K_{1/2}}{2}\left[3\tau_c + \frac{5\tau_c}{1+\omega_L^2\tau_c^2} + \frac{2\tau_c}{1+4\omega_L^2\tau_c^2}\right]. \tag{3.14}$$

The homonuclear dipol-dipol interaction of spin-1/2 nuclei is introduced by the constant

$$K_{1/2} = \frac{3}{160}\left(\frac{\mu_0}{\pi}\right)^2 \frac{\gamma^4\hbar^2}{r^6}, \tag{3.15}$$

where r is the distance between two interacting spins [Bov96]. Based on these equations, a slow and fast motion regime can be distinguished by the T_1 minimum at $\omega_L\tau_c = 1$. In the extreme narrowing limit where $\omega_L\tau_c \ll 1$, molecular motions are fast on the NMR timescale. T_1 and T_2 relaxation times coincide as typically observed in low viscous liquids. In highly viscous liquids and polymers well above the glass transition temperature, motions are slow compared to ω_L. The relaxation times diverge with T_1 increasing and T_2 decreasing. Short T_2 times lead to a fast FID decay while long T_1 times require longer recycle delays for signal averaging. This combination makes the slow motion regime particularly challenging to measure and indicates the need for solid state NMR techniques.

Restricted motion effects

In polymer networks, a proton spin is permanently perturbated by the magnetic field of another proton in close proximity. As a result, it

experiences different local magnetic fields, and therefore, homonuclear dipolar relaxation. Complex materials exhibit many interdependent spin-spin interactions, causing a broad range of Larmor frequencies and a broad peak in the spectral domain on the order of up to several kilohertz. In a simplified picture, protons can be approximated as bar magnets, as illustrated in Figure 3.3. The magnitude of the spin-spin interaction between neighboring protons is consequently a function of the distance r between the interacting spins and their angle θ with respect to the static magnetic field B_z. In terms of the bar magnet analogy, two limiting cases for magnet configurations exist. Bar magnets attract each other when placed on top with the same north/ south configuration, but repel each other when placed side by side [Saa12]. This angular dependent magnetic interaction is described by the second Legendre polynomial

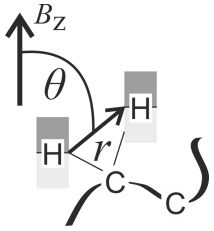

Figure 3.3: Dipolar coupling of two neighboring proton spins depends on the distance r and angle θ.

$$P_2(\cos(\theta)) = \frac{3\cos^2(\theta) - 1}{2}\,. \tag{3.16}$$

Note that $P_2(\cos(\theta))$ equals zero at an angle of $54.74\,^\circ$, which is referred to as the magic angle [And58]. This angle is exploited in the magic-angle spinning technique, a solid state NMR method to reduce dipolar couplings of solid samples by spinning the sample on the order of kilohertz at the magic angle, obtaining thereby narrow spectral lines. The dipolar coupling frequency ω_D between two interacting ^1H spins at a typical distance of $r_{HH} = 1.8$ Å for a CH_2 group along a polymer backbone is given by

$$\begin{aligned} \omega_D/2\pi &= \frac{\hbar\gamma_H^2\mu_0}{4\pi r_{HH}^3}\left(\frac{3\cos^2(\theta) - 1}{2}\right) \\ &= 21\text{ kHz}\left(\frac{3\cos^2(\theta) - 1}{2}\right), \end{aligned} \tag{3.17}$$

where μ_0 is the permeability of the vacuum [Pre04]. In highly mobile liquids with isotropic motion, all possible orientations are reached within the time scale of the NMR experiment. Consequently, the average of $P_2(\cos(\theta))$ equals zero and a dipolar coupling is not observed. In contrast, crosslinks in polymer networks are topological constraints and prevent this motional averaging of all polymer chain conformations. As a result, a residual diplor coupling D_{res} persists that can be quantified by double quantum (DQ) NMR experiments [Saa07]. D_{res} is proportional to the number of possible polymer chain conformations, and therefore, is proportional to the molecular weight of polymer chains between crosslinks. The assessment of D_{res} provides unique quantitative insights into the topology of crosslinked soft matter, such as elastomers [Saa12].

3.3 TD NMR PULSE SEQUENCES IN SOFT MATTER ANALYSIS

Owing to the intrinsic relationship between NMR relaxation times and the local molecular mobility of materials, NMR relaxometry techniques play a pivotal role in unraveling molecular origins of macroscopic properties. Since the measurements of relaxations times does not necessarily require Fourier transformation of the FID, and therefore, high magnetic fields, they are commonly performed on low-field benchtop NMR setups ($\omega_L = 20 - 40$ MHz) operating in the time domain. TD NMR measurements have been extensively used in polymer and food science that particularly benefit from the non-invasive nature of the measurements [Hilo6; Bes19]. Common applications of TD NMR include the routine quality control of elastomers and foods [Lito4; Gut16], the monitoring of crystallization kinetics in fats and semi-crystalline polymers [van73; Rat17; Rän18], the fundamental exploration of polymer molecular dynamics [Vac11], and the quantification of crosslinking density and network heterogeneity of charged and uncharged elastomers [Saa12; Höp14].

Due to the rather simple setup, TD NMR experiments on low-field devices suffer from long instrument dead times, pronounced magnetic field inhomogeneities, and low signal to noise ratios [Bes19]. Consequently, great effort has been devoted to adapt many traditional high-field pulse sequences to the benchtop devices. Some common pulse sequences are discussed in the following.

Longitudinal T_1 relaxation time

The T_1 relaxation time describes the recovery of the magnetization component along the static magnetic field B_z. Consequently, it is sensitive to fast motions close to the Larmor frequency, such as molecular rotations of polymer side groups, that induce transitions between spin energy states. The assessment of T_1 relaxation times is particularly useful to quantify the content of low molecular weight components, such as solvent, that have long T_1 relaxation times on the order of seconds compared to the bulk material [Todo6; Bai14]. Another application is the quantitative component analysis of solid mixtures, for instance, in pharmaceutical blends containing components with sufficiently separated T_1 relaxation times [Stu17]. The saturation recovery (SR) pulse sequence is commonly used to measure T_1 relaxation times, as shown in Figure 3.4 [Mar71]. The SR pulse sequence comprises a saturation time consisting of a nonuniform $\pi/2$ pulse train to zero the longitudinal z component of the magnetization. After a waiting period, the recovery delay τ, a $\pi/2$ is applied to flip the magnetization into the xy plane and record the initial FID signal intensity. The initial FID signal intensity is plotted against τ, which exhibits a characteristic mono-or multi-exponential build-up curve from which the T_1 relaxation times can be inferred. The inversion recovery pulse sequence is another common technique. Instead of a saturation time, it applies an initial π pulse to invert the longitudinal magnetization, and subsequently,

uses $\pi/2$ pulse to record the FID after varying recovery delay times [Car54].

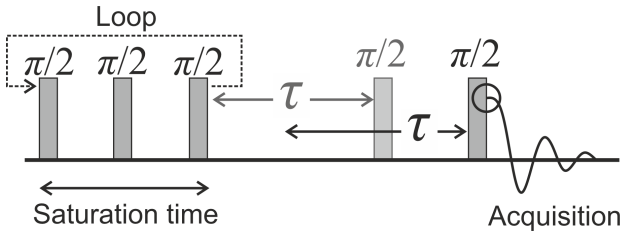

Figure 3.4: Saturation recovery pulse sequence to obtain T_1 relaxation times. The saturation time is a nonuniform $\pi/2$ pulse train used to zero the longitudinal z component of the magnetization. After the recovery delay τ, a $\pi/2$ is applied to acquire the initial FID signal intensity, highlighted by the circle within the acquisition. The initial FID signal intensity is plotted against the recovery delay to obtain the characteristic T_1 relaxation build-up curves.

Transverse T_2 relaxation times

The T_2 relaxation time is the characteristic time constant of the FID decay, and therefore, can be simply measured by a $\pi/2$. However, in low-field NMR devices, this simple FID decay is, in addition to molecular dynamics, governed by the pronounced magnetic field inhomogeneity, which leads to a much shorter so-called T_2^* relaxation time. Complex pulse sequences have been designed to extract the true T_2 relaxation time of the sample. The Hahn echo (HE) and CPMG (Carr – Purcell – Meiboom – Gill) pulse sequences measure the T_2 relaxation of the sample by the formation of spin echoes [Hah50; Mei58]. Upon an initial $\pi/2$ pulse, the spin phase coherence is gradually lost over time causing the FID decay. The application of a subsequent π pulse after a waiting period, the echo time τ_{echo}, leads to a time-reversal and phase coherence is re-obtained even in inhomogenous magnetic fields in a form of a spin echo with a characteristic amplitude that is a function of τ_{echo}. HE is a two pulse sequence, which is repeated for increasing τ_{echo} [Hah50]. The CPMG pulse sequence applies a $\pi/2$ pulse followed by a sequence of π pulses, and therefore, is substantially faster than the HE as it obtains the whole T_2 relaxation curve in one experiment [Mei58]. Figure 3.5 illustrates both the HE and CPMG pulse sequences. Plotting the echo amplitude signal intensity against τ_{echo} reveals an exponential decay curve, which resembles the characteristic T_2 relaxation curve of the sample. The shape of the exponential T_2 decay function highly depends on the studied system. Highly mobile systems exhibit a mono-exponential decay. Systems with highly restricted mobility, such as crystalline domains in semi-crystalline polymers, can be represented by a Gaussian type decay ($I \propto \exp(-(\tau_{\text{echo}}/T_2)^2)$ [Mau06; Rän18]. Vulcanized rubbers above T_g exhibit a compressed exponential decay ($I \propto \exp(-(\tau_{\text{echo}}/T_2)^n)$ with

$1 < n < 2$) whereas T_2 relaxation curves of heterogeneous materials, such as swollen SAPs, follow a stretched exponential Kohlrausch – Williams – Watts (KWW) decay function ($I \propto \exp(-(\tau_{\text{echo}}/T_2)^{\beta})$ with $0 < \beta < 1$) [Höp14; Nie21]. The stretching parameter β is inversely proportional to the width of the T_2 relaxation time distribution [Böh94; Edh00; Luk19], and therefore, resembles the superposition of dynamically different, yet indistinguishable topologies in the material.

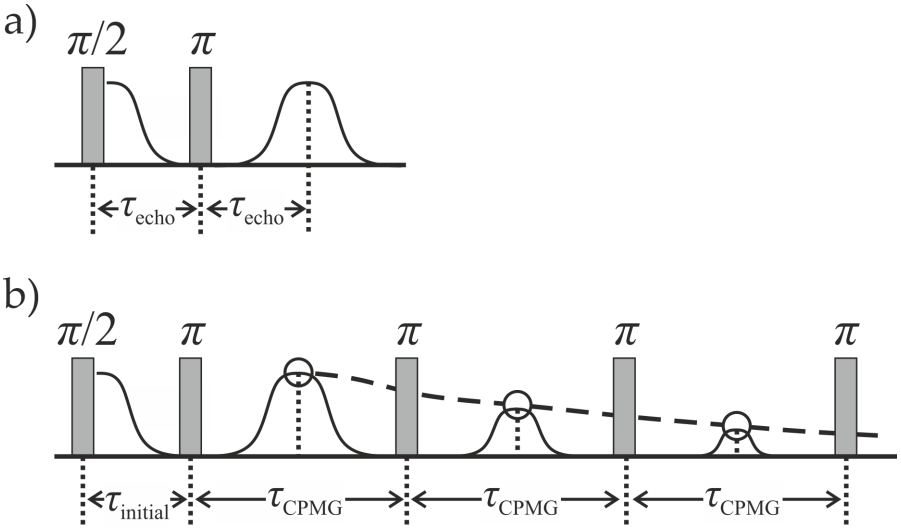

Figure 3.5: Hahn echo (a) and CPMG (b) spin echo pulse sequences to measure T_2 relaxation times of soft matter [Hah50; Mei58]. The dashed line highlights the obtained T_2 relaxation curve from the echo maxima of the CPMG experiment.

Residual dipolar coupling

In crosslinked materials, such as rubbers, the motion of polymer chains between crosslinks is restricted. This topological constraint prevents the complete motional averaging of dipolar couplings between neighboring protons. As a result, a small, yet finite residual homonuclear dipolar coupling constant D_{res} persists on the NMR time scale that is directly related to the mesh size of the polymer network. D_{res} can be assessed by the Baum-Pines (BP) pulse sequence, which has been recently adapted to low-field benchtop NMR spectrometers [Saa07; Bau86]. This rather long pulse sequence comprises an excitation period to generate DQ (or higher order) coherences and a subsequent reconversion period that converts the generated coherences into a detectable magnetization, as illustrated in Figure 3.6. The converted coherences can then be detected by the FID after a single $\pi/2$ pulse. The most intriguing advantage of current BP implementations is that by adjusting the receiver phase during signal acquisition, one can selectively measure both the reconverted DQ coherence I_{DQ} and a single-quantum reference signal I_{ref} from isotropically, mobile species. The appropriate normalization of the two data sets yields the characteristic DQ build-up curves of the sample from which D_{res} can

be inferred. This normalization procedure is discussed in Section 6.2, p. 57.

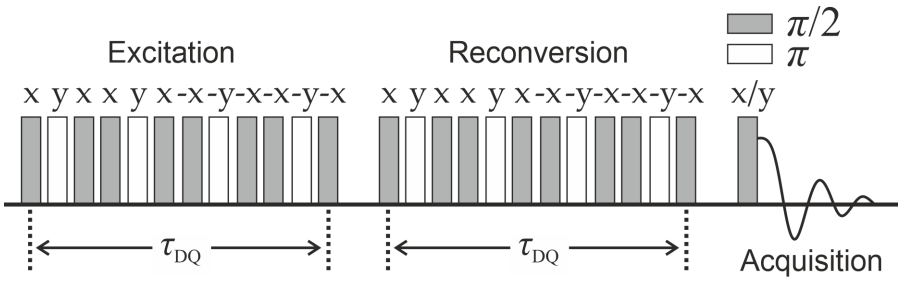

Figure 3.6: Adapted Baum-Pines pulse sequence to measure residual dipolar couplings in low-field benchtop NMR spectrometers [Bau86; Saa07]. The first twelve pulses with a DQ mixing length τ_{DQ} in the excitation period generate DQ (or higher order) coherences that are subsequently converted with the similar pulse train into a detectable magnetization. The signal of the single-quantum reference and the DQ coherences evolve orthogonal in the FID. By consecutively adjusting the receiver phase, both signals can be acquired simultaneously.

Part II

RESULTS AND DISCUSSION

4

SYNTHESIS OF CATIONIC HYDROGEL MODEL SYSTEMS

Abstract Despite the substantial industrial importance of SAPs, only a limited number of positively charged SAPs are known. This chapter introduces the synthetic routes of two cationic amine based SAPs with distinct functional groups. The first model system resembles common industrial approaches and relies on the free radical copolymerization of acrylamide (AM) and (3-acrylamidopropyl) trimethylammonium chloride (APTAC). The second model system is based on poly(vinyl amine) (PVAm), which comprises highly versatile amine groups that can be used for subsequent postmodification reactions. Relevant synthetic parameters, namely the degree of crosslinking (DC) and the degree of ionization (DI) are defined. Particular attention is paid to the droplet-based microfluidic technique, which enables the synthesis of spherical, monodisperse SAP samples with dry particle sizes on the order of hundreds of micrometers.

4.1 MONODISPERSE PARTICLES VIA DROPLET MICROFLUIDICS

High-throughput analysis drives microfluidics research.

Microfluidics deals with precise manipulation of fluid flow at the microscopic level. This concept appeared initially in the 1990s from a need to miniaturize chemical analysis systems [Rap17]. The use of single-phase microfluidics allowed for integration of various analytical techniques, such as chromatography, electrophoresis, and flow injection analysis, into a time-efficient miniaturized chemical analysis system, reducing thereby the need of fully-equipped chemical laboratories and specialized operators [Man90]. Owing to the rise in demand for quantitative high-throughput analysis in life sciences, droplet microfluidics emerged as a subbranch of microfluidics in the early 2000s [Tho01; Nis02; Tho02].

Droplet microfluidic techniques use water-in-oil emulsions to create discrete volumes of fluids that compartmentalize reaction steps and minimize cross-contamination. Each droplet can be seen as a microreactor that can be independently analyzed, transported, and processed in a controlled manner, achieving higher throughput than conventional single-phase microfluidics [Teh08; Vla12; Gue20]. The emulsions can be further used to create various uniform, monodisperse particle topologies, such as core-shell structures, hollow spheres, Janus and non-spherical particles [Uta05; Kim07; Wan19; Vla12; She13; Sei17a].

Droplet microfluidic devices are typically either fabricated by photolithography using elastomeric poly(dimethylsiloxane) material or glass capillaries with channel diameter sizes ranging from micrometers to millimeters [Teho8].

Principal factors that dictate flow through the channels and droplet formation can be described by a set of dimensionless quantities related to fluid mechanics [Tra18]. The ratio of inertial to viscous forces predicts the magnitude of laminar and turbulent flow inside the channels. This ratio is known as the Reynolds number

Relevant dimensionless numbers in microfluidics.

$$\mathrm{Re} = \frac{\rho v l}{\eta}\,, \tag{4.1}$$

where ρ is the fluid density, v is the fluid velocity, l is the characteristic length and η is the dynamic viscosity [Rey83]. As a general rule, Re values approximately < 2000 are characteristic for laminar flow [Pur77]. Above that threshold, turbulent flow dominates, producing random vortices and other chaotic fluctuations.

A critical parameter in water-in-oil emulsions that governs droplet dynamics, such as fission or droplet break off, is the capillary number

$$\mathrm{Ca} = \frac{\eta v}{\gamma_{\mathrm{oil/water}}}\,, \tag{4.2}$$

where $\gamma_{\mathrm{oil/water}}$ is the interfacial tension between oil and water phases [Teho8]. Ca typically ranges from 10^{-3} to 10 and can be used to predict the size and shape of the droplets [Tra18]. Spherical droplets are formed at low Ca where the interfacial surface area is minimized by the dominating interfacial tension. Viscous forces dominate at higher Ca causing asymmetric morphologies.

Glass capillary device for hydrogel synthesis

This work uses the glass capillary approach to generate monodisperse water-in-oil emulsions as it is sufficient for the synthesis of hydrogel particles with sizes on the order of hundreds of micrometers in their dry state. Therefore, a flow-focusing geometry that consists of two coaxially aligned glass capillaries was constructed. Section A.3.2, p. 108 describes the technical details more thoroughly. In general, emulsion drops are created by forcing two immiscible fluids into a narrow orifice. The inner fluid stream of the dispersed phase is focused by the outer fluid stream of the continuous phase as they converge at the inner-capillary tip [Coho1; Anno3]. Figure 4.1 shows the principle of the flow-focusing geometry and an in-situ photo of droplet formation inside a constructed glass capillary device.

For hydrogel synthesis, an aqueous pre-gel solution consisting of monomer, photo-initiator and crosslinker was used as the dispersed phase. A mixture of mineral oil and surfactant (ABIL EM 90, Evonik) served as continuous phase. Both phases were continuously injected with syringe pumps into the glass-capillary device. Flow rates and sizes of glass capillaries were fine-tuned to produce uniform droplets

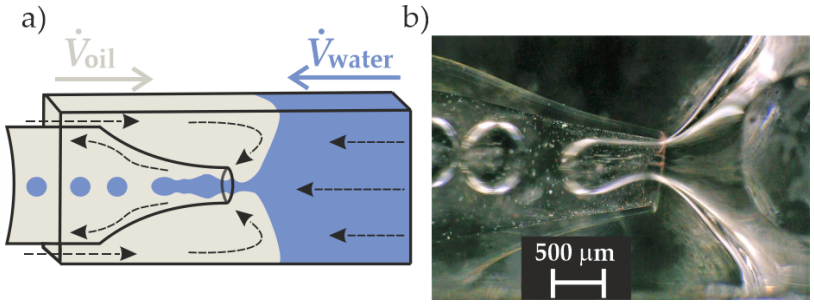

Figure 4.1: Glass capillary microfluidic device. a) Scheme of a flow-focusing geometry that uses a reversed inner fluid stream with flow rates of the aqueous dispersed phase $\dot{V}_{water}$ and continuous oil phase $\dot{V}_{oil}$. Both phases converge at the inner-capillary tip, creating monodisperse emulsion drops. b) Photo of in-situ droplet formation inside a constructed glass-capillary device. Figure adapted from [Fen22b].

with varying diameter sizes. The monomer containing droplets were collected in a beaker and photo-polymerized. Section A.3.2, p. 108 describes the microfluidic synthesis in detail. Table 4.1 summarizes the chosen parameters. To avoid an early gelation of the pre-gel solution inside the glass-capillary device, the flow rate of the dispersed phase was $\geq 4.3\,\mathrm{mL\,h^{-1}}$.

Table 4.1: Overview of experimental microfluidic parameters and the resulting dry particle diameter D_{dry}. $\dot{V}_{water}$ denotes the flow rate of the aqueous phase and $\dot{V}_{oil}$ refers to the continuous oil phase. Glass capillary sizes are specified by the width w and diameter d of the outer square and inner round capillary, respectively. The Reynolds number Re was calculated for the flow of the continuous oil phase inside the round capillary.

D_{dry} (µm)	w (mm)	d (mm)	$\dot{V}_{oil}$ ($\mathrm{mL\,h^{-1}}$)	$\dot{V}_{water}$ ($\mathrm{mL\,h^{-1}}$)	Re
≈ 800	2.2	1.4	60	17	1.1
≈ 600	2.2	1.4 (tip: 0.4)	60	17	1.1
≈ 200	1.1	0.6	17	4.3	0.7

4.2 POLY(ACRYLAMIDE) - THE DORMANT FRAMEWORK

Only a limited number of cationic chemical functional groups can be used in polymer synthesis. Common moieties include ammonium, phosphonium, and sulfonium cations. Quaternary ammonium based compounds are by far the most prominent in polymer synthesis because of their rather easy accessibility and superior chemical and thermal stability compared to the alternatives. Moreover, their hydrophilicity is particularly desirable for aqueous applications [Jae10].

Consequently, the first cationic hydrogel model system represents a standard, widely available composition and was synthesized from commercially available AM and APTAC. This model system is termed the dormant framework, which refers to the fact that quaternary ammonium compounds are intrinsically inert functional groups, preventing thereby any facile postmodification reactions for property enhancement. Analogue to the standard preparation of anionic PSA hydrogels, the cationic AM hydrogels were prepared by free radical crosslinking copolymerization of the aforementioned monomer species and MBA as divinyl crosslinker [Mat96; Buc98; Bar08]. Figure 4.2 illustrates the synthetic route.

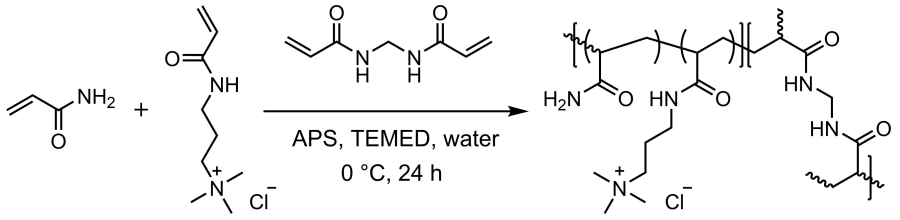

Figure 4.2: Synthesis of cationic poly(acrylamide-*co*-(3-acrylamidopropyl) trimethylammonium chloride) (PAM) hydrogels through aqueous free radical crosslinking copolymerization initiated by ammonium persulfate (APS) and the accelerator *N*,*N*,*N*′,*N*′-tetramethylethane-1,2-diamine (TEMED).

Synthetic parameters

As Section 2.2, p. 10 concludes, the pre-gel monomer composition profoundly affects network structure, and therefore, mechanical and swelling properties of the hydrogels [Buc98]. To elucidate the interplay between synthetic factors and network structure, this dissertation specifies three characteristic synthetic parameters that were systematically varied, namely the degree of crosslinking (DC), degree of ionization (DI), and monomer concentration (C_0).

The molar ratio of crosslinker to monomer defines

$$DC = \frac{n(\text{crosslinker})}{n(\text{monomer}) + n(\text{co-monomer})}\,, \tag{4.3}$$

where $n(\text{monomer})$, $n(\text{co-monomer})$, and $n(\text{crosslinker})$ refer, for this model system, to AM, APTAC, and MBA, respectively. The composition was varied to target $DC = 1$, 3, and 5 mol%.

Charge density along the polymer backbone inside the hydrogel network was adjusted by the amount of APTAC in the pre-gel mixture given by

$$DI = \frac{n(\text{APTAC})}{n(\text{AM}) + n(\text{APTAC})} \,. \tag{4.4}$$

This ratio was adjusted to target $DI = 25$, 50, and 75 mol%. The total monomer concentration was varied in the range $C_0 = 13 - 50$ wt%. Section A.2, pp. 105–106 gives a detailed description of the synthetic procedure. Table A.1, p. 106 gives an overview of the synthesized PAM samples.

4.3 POLY(VINYLAMINE) - THE VERSATILE FRAMEWORK

Poly(vinylamine) (PVAm) represents an interesting candidate for cationic hydrogels due to its high charge density and the pH sensitive content of primary amine groups that are able to undergo a large number of efficient postmodification reactions [Pel14]. The resulting excellent water solubility, metal binding capacity, and adhesive properties have been used in various applications including wastewater treatment [Che11], separation-membranes [Kra01], coatings in paper production [Fen06], chromatography stationary phases [Cha04], and surface functionalization [Pel14].

Despite its rather simple chemical structure, PVAm has been widely available only for two decades [Pin10]. Great effort has been devoted to the development of a facile synthetic route mainly due to the inherent stability of vinylamine as a result of enamine-imine tautomerism, as shown in Figure 4.3 [Jon44]. Consequently, polymerizable precursor monomers are required. Subsequent acid or basic hydrolysis of the precursor polymers yields the desired PVAm backbone structure. Nowadays, several synthetic routes for linear PVAm are known which use a variety of precursor monomers, such as *N*-vinylacetamides [Pin10], *N*-vinylformamide (NVF) [Krö00], and *N*-vinylphthalimides [Mak07], yet only few studies demonstrate the synthesis of cationic PVAm hydrogels. Despite the fact that previous studies have shown the synthesis of pH responsive PVAm microgels (diameter < 1 µm) dispersions [Tha13; Sue13; McC14], the potential use of PVAm as highly charged SAP remains unexplored.

Figure 4.3: Ethenamine - ethanimine tautomerism.

Designing a hydrolysis-resistant crosslinker

This gap in PVAm hydrogel research presumably results from the lack of suitable crosslinker, since common acrylamide-based crosslinker, such as MBA, are not stable during the hydrolysis step of the polymer precursors. This dissertation resolved the drawback by synthesizing a hydrolysis-resistant crosslinker based on NVF. Nucleophilic substitution of two NVF monomer units to bis(2-bromoethyl) ether (BBE) yielded the desired divinyl bis-NVF crosslinker (BNVF), which was

subsequently used in the PVAm hydrogel synthesis. Figure 4.4 shows the synthesis procedure of the crosslinker.

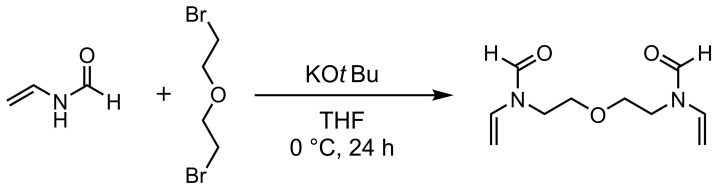

Figure 4.4: Synthesis of the *N*-vinylformamide (NVF) based hydrolysis-resistant crosslinker *N*,*N*′-(oxybis(ethane-2,1-diyl))bis(*N*-vinylformamide) (BNVF) using bis(2-bromoethyl) ether (BBE) for the synthesis of PVAm hydrogels.

The synthesis of cationic PVAm hydrogels was realized in a two-step process. First, monodisperse spherical PNVF precursor particles were synthesized by a copolymerization of NVF and BNVF using the droplet microfluidic technique. The spherical particle shape ensures a more systematic and uniform postmodification of the particles. Three different particle sizes with mean diameter values approximately of 200, 600, and 800 µm were synthesized. Crosslinking density was varied according to Equation 4.3, p 34 to target the values $DC = 1$, 2, and 3 mol%. Figure 4.5 shows the size distribution of dry PNVF particles with $DC = 2$ mol%. The narrowest size distribution was achieved using the smallest microfluidic device that targets a diameter of 200 µm. The standard deviation increases almost tenfold for larger particles sizes, which presumably arises from both the use of higher flow rates and larger glass capillary sizes, resulting in an increase of the dimensionless quantities Re and Ca.

PVAm particle size distributions

The synthesized PNVF hydrogels were subsequently hydrolyzed under acidic conditions to yield the desired highly charged PVAm hydrogels. The synthetic procedure is shown in Figure 4.6.

This dissertation terms PVAm hydrogel networks as versatile frameworks, since their high primary amine content enables various, efficient postmodification reactions, for instance, with epoxides [Pel14], aldehydes [Pin10], ketones [Tro19], or electron-deficient aromatics [Hof10]. In SAP research, the most common postmodification is surface-crosslinking, which combines a loosely crosslinked core with a rigid surface. As a result, surface-crosslinked particles exhibit both an increase in absorbency under load and a reduction in gel-blocking effects, which is beneficial for typical SAP applications [Ram13; Joc09; MJ20; Hua06].

Common surface-crosslinking techniques use hazardous crosslinker, such as diepoxides and dialdehydes, at elevated temperatures (> 70 °C) to facilitate the reactivity of functional groups, mainly carboxylates, along the polymer backbone [Jan20; Moi15; Moi17; Kim20]. In contrast, it has been shown that PVAm can react under mild conditions

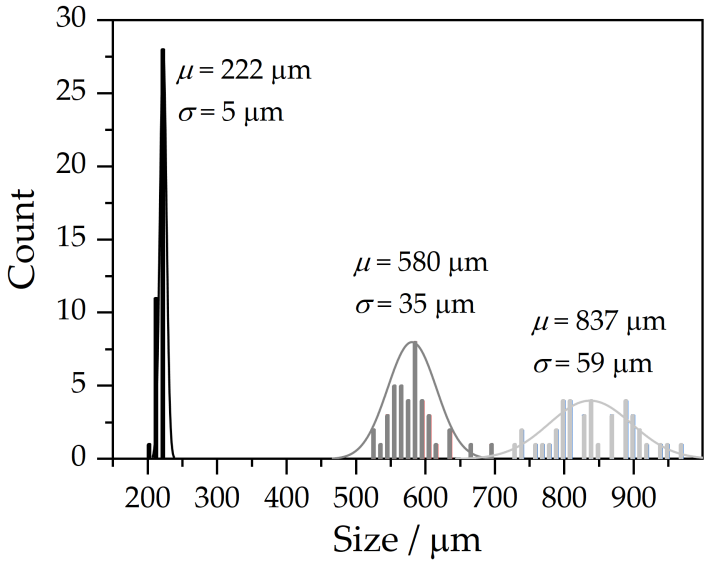

Figure 4.5: Size distribution of dry monodisperse PNVF hydrogels with $DC = 2\,\text{mol\%}$ obtained by droplet microfluidics using BNVF as crosslinker. Each particle size batch contains 40 particles. The diameter of the dry particles was determined by the digital light microscope Keyence VHX 900F using the internal software. For the histogram, a bin width of 10 was used. Solid lines are least-squares normal distribution fits, yielding mean values (μ) and standard deviations (σ) of the size distributions.

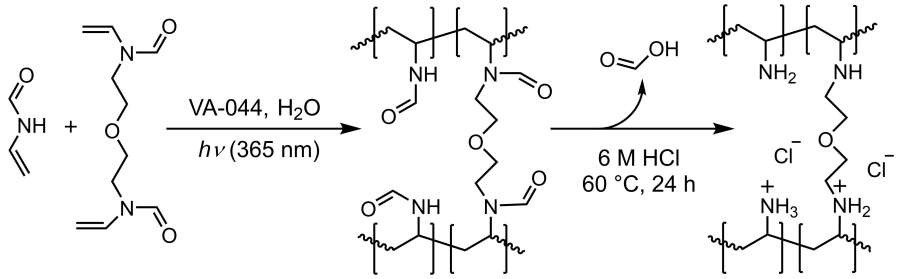

Figure 4.6: Two-step synthesis of monodisperse PVAm hydrogels. Spherical precursor PNVF hydrogels were prepared by the crosslinking copolymerization of NVF and BNVF using droplet microfluidics and 2,2′-azobis[2-(2-imidazolin-2-yl)propane] dihydrochloride (VA-044) as photo-initiator. Acidic hydrolysis of PNVF with HCl yields PVAm hydrogels by releasing formic acid.

with ketones that are generally considered less harmful, but also less electrophilic than aldehydes [Li18; Tro19]. This intriguing reactivity is unique for PVAm and cannot be reproduced by low molecular weight

amines in water, yet application of this reactivity for PVAm network formation through ketone linkages remains widely unexplored.

It has been shown that PVAm can undergo rapid crosslinking with water-soluble bis(*N*-acylpiperidinone)s where the *N*-acyl moiety increases electrophilicity of the piperidinone carbonyl group [Uhl21]. NMR studies of the gels have revealed that crosslinks are formed exclusively through hemiaminal and aminal linkages (see Figure 4.7 for chemical structures), which can be reversibly adjusted with varying pH values [Uhl21]. At low pH values < 2 crosslinking was fully reversed, suggesting dynamic network formation. This dissertation exploits the PVAm – bis(*N*-acylpiperidone) chemistry for efficient surface-crosslinking. Therefore, dry PVAm hydrogel particles were partially swollen in aqueous crosslinker solution under room temperature. Figure 4.8 shows the synthesis of PVAm core-shell particles using 1,2-bis(4-oxo-piperidin-1-yl)ethane-1,2-dione (OBP) as crosslinker.

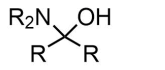

Hemiaminal

Aminal

Figure 4.7: Chemical structure of hemiaminal and aminal functional groups.

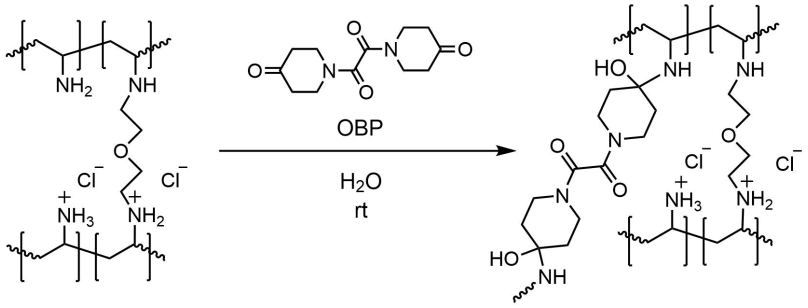

Figure 4.8: Reaction of PVAm hydrogels with water-soluble 1,2-bis(4-oxo-piperidin-1-yl)ethane-1,2-dione (OBP) used for surface-crosslinking.

Shell thickness of the core-shell particles was varied by systematically changing the volume fraction ϕ_{shell} that is penetrated by surface-crosslinker solution with respect to the gravimetrically determined equilibrium swelling capacity Q_{eq} given by

$$\phi_{\text{shell}} = \frac{m_{\text{water}}}{Q_{\text{eq}} m_{\text{particles}}}, \tag{4.5}$$

where m_{water} is the mass of water used to dissolve the surface-crosslinker and $m_{\text{particles}} = 50$ mg is the mass of dry PVAm particles. Consequently, ϕ_{shell} defines a fraction of the water required to fully swell the particles. This fraction is used to dissolve the surface-crosslinker OBP. ϕ_{shell} was varied in the range $1 - 10$ vol%. Presuming that OBP reacts quantitatively and immediately with two vinylamine n_{VAm} units along the polymer backbone, the molar amount of OBP n_{OBP} for surface-crosslinking is given by

$$n_{\text{OBP}} = \frac{n_{\text{VAm}} \phi_{\text{shell}}}{2}. \tag{4.6}$$

To validate the assumption that OBP reacts within the timescale of swelling, gelation kinetics of the crosslinking reactions was compared to the swelling kinetics. Gelation kinetics was measured by a rheological time sweep at a constant shear rate of $\dot{\gamma} = 1\ s^{-1}$ using a vane-cup geometry. An aqueous 6.6 wt% PVAm ($M_w = 340$ kDa) solution was poured into the cup, and subsequently, OBP crosslinker solution, corresponding to $DC = 5$ mol%, was added. Application of a constant shear rate ensures that the crosslinker solution distributes through out the geometry after addition. Swelling kinetics of a spherical dry PVAm hydrogel particles was measured with a digital light microscope monitoring the time evolution of the particle diameter during swelling. Section B.1.1, p. 111 and Section B.2, p. 112 describe more thoroughly the experimental procedures of the rheological measurement and swelling kinetics, respectively. Figure 4.9 shows both the time evolution of the apparent viscosity during gelation and swelling in deionized water.

The drop in viscosity at 75 s marks the addition of aqueous crosslinker solution that dilutes the PVAm solution. Within 20 seconds the viscosity rapidly increases several orders of magnitude from 40 mPa s to 10 Pa s, suggesting a rapid crosslinking reaction. The second drop in viscosity at 120 s presumably arises from wall-slips and rapture of the crosslinked structure as a fully crosslinked gel had been formed at this stage. In contrast, swelling of dry PVAm hydrogel particles in deionized water is distinctly slower. The time evolution of the particle volume during swelling follows a first-order kinetic equation with a characteristic swelling time $\tau_s = 151 \pm 9$ s. Ten volume percent of the maximum swelling capacity was reached within 40 s, which supports the assumption of shell formation as the reactivity of OBP is within the time evolution of swelling. Moreover, PVAm hydrogel particles are always partially swollen up to 10 vol% of the equilibrium swelling capacity during the synthesis of the core-shell particles. Consequently, a significant portion inside the hydrogel particles, defined as the core, remains in its glassy state unable to be penetrated by surface-crosslinker during the synthetic time period.

Table A.2, p. 110 gives an overview of the synthesized neutral PNVF, cationic PVAm and PVAm core-shell hydrogel samples.

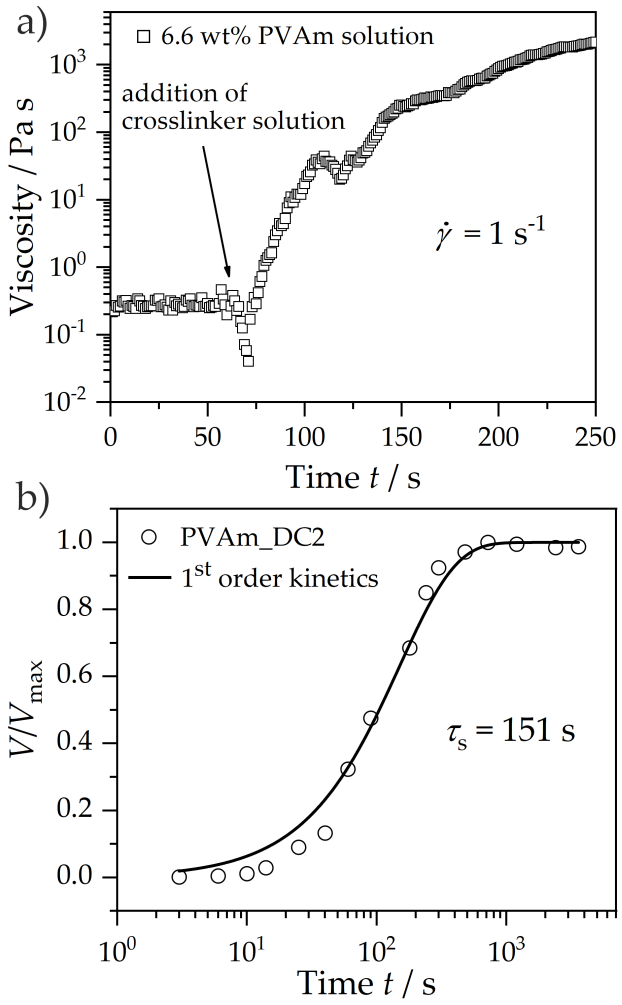

Figure 4.9: Crosslinking reaction of PVAm with OBP compared to PVAm hydrogel swelling kinetics. a) Time evolution of the apparent viscosity during crosslinking of a 6.6 wt% PVAm (M_w = 340 kDa) solution with OBP (DC = 5 mol%) measured at room temperature. b) Time evolution of normalized volume of the PVAm_DC2 hydrogel sample during swelling in deionized water. The solid line is a least-squares first-order kinetic fit with a characteristic swelling time constant $\tau_s = 151 \pm 9$ s. Reactivity of OBP is almost instantaneously compared to the swelling process, supporting the assumption of shell formation during PVAm core-shell particle synthesis.

5

SWELLING PROPERTIES

Abstract The high water swelling capacity of SAPs is certainly their most relevant property. This chapter elucidates the influence of synthetic parameters on the equilibrium swelling capacity Q_{eq} of the synthesized cationic hydrogels. The measured Q_{eq} as a function DC in PAM hydrogels decreases according to a power law of the form $Q_{eq} \propto DC^{-3/5}$. The influence of particle size and charge density on the swelling kinetics of spherical PNVF and PVAm are discussed. Acidic hydrolysis of PNVF to form PVAm hydrogels decreases the characteristic swelling time constant by a factor of ≈ 3 from 440 s to 150 s. This increase in swelling rate is attributed to electrostatic repulsions of neighboring charged monomer units. Seawater profoundly affects Q_{eq} of PSA and PVAm that exhibit an ion-induced volume transition in Mg^{2+} and SO_4^{2-} solutions, respectively. In contrast, seawater does not influence the swelling behavior of cationic PAM hydrogels.

5.1 INFLUENCE OF SYNTHETIC PARAMETERS ON SWELLING

Differences in the osmotic pressure between the gel and the surrounding liquid drives the swelling of SAPs. Opposing elastic forces from the elongation of the network polymer chains counterbalances the swelling. Consequently, the underlying chemical and topological structure of the network profoundly affects the equilibrium swelling capacity Q_{eq}. The synthetic methodology dictates the network structure, yet understanding the exact influence of pre-gel compositions on Q_{eq} remains a challenge as it highly depends on the chosen system, and therefore, general physical models capable of quantitatively predicting macroscopic properties based on synthetic parameters do not exist [Wan16]. Since Q_{eq} is the most application-relevant property of SAPs, quantifying the influence of synthetic properties is crucial for developing rational material design principles.

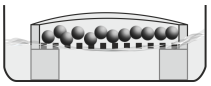

Figure 5.1: Experimental setup for swelling measurements.

In this work, Q_{eq} was measured gravimetrically simply by weighing the gel. Dry hydrogel particles were placed on a wire gauze lying on a metal rack. The metal rack was then placed into a Petri dish, as shown in Figure 5.1. The swelling of the dry particles was induced by filling the Petri dish with aqueous solution. The particles were swollen overnight to reach the equilibrium state. A detailed description is

given in Section B.1, p. 111. The mass ratio of absorbed water to dry hydrogel particles gives

$$Q_{\text{eq}} = \frac{m_{\text{water}}}{m_{\text{poly}}} . \tag{5.1}$$

To ensure accurate measurements, excess water from the gel surface has to be removed carefully by gently pressing the wire gauze onto paper tissue. After solvent removal, evaporation of water at ambient conditions (25 °C and 40 % relative humidity) with an estimated rate of 1 mg min^{-2} cm^{-1} might further dry the particles [His93]. This weight loss is particularly significant for thin gel films where a large surface to volume ratio potentially skews the results.

The influence of synthetic parameters introduced in Section 4.2 were studied for the cationic PAM hydrogels. Figure 5.2 shows that the initial monomer concentration C_0 distinctly affects the equilibrium swelling capacity.

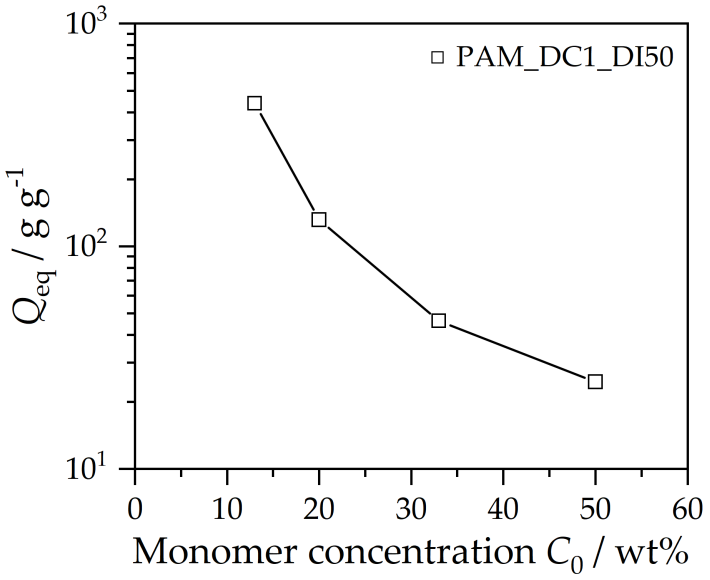

Figure 5.2: Influence of pre-gel monomer concentration on equilibrium swelling capacity. The solid line serves as a guide to the eye. Error bars are within symbol size.

Q_{eq} decreases by more than 90 % from 440 at $C_0 = 13$ wt% to 25 at $C_0 = 50$ wt%. This drastic change in Q_{eq} can be explained by mechanical and kinetic considerations of the crosslinking copolymerization. C_0 defines the relaxed reference state of the polymer network from which a further extension of the polymer chains generates an opposing elastic force counterbalancing the swelling process. Consequently, high C_0 values resemble a reference state with low water content (i. e., high polymer concentration), and therefore, reduce the swelling capacity.

In addition, measurements of the pendant vinyl bond conversion suggest that kinetics of the crosslinking copolymerization plays a

pivotal role in governing Q_{eq} [Kiz03; Ell04]. Pendant vinyl bonds are unreacted vinyl bonds of the divinyl crosslinker along the polymer backbone. They mainly undergo either intermolecular radical crosslinking reactions with other propagating polymer chains or intramolecular cyclization reactions [Nag96]. Consequently, the influence of C_0 on the formation of pendant vinyl bonds and their subsequent reactions in either crosslinking or cyclization reactions profoundly affects Q_{eq}. Figure 5.3 illustrates some possible pendant vinyl group reaction pathways in a crosslinking copolymerization [Nag96].

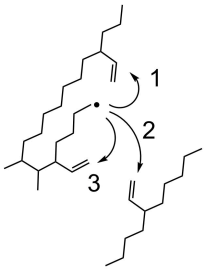

Figure 5.3: Reaction pathways of pendant vinyl groups along an arbitrary polymer chain:
1) Multiple crosslinking,
2) crosslinking,
3) cyclization.

Kinetic models account for effects of C_0 on the aforementioned reactions types based on statistical assumptions. At high C_0 the propagating polymer chain is predominantly surrounded by unreacted monomers, offering multiple reactions sites for the propagating polymer chain that quickly reacts away from the pendant vinyl group. As a result, the probability for primary cyclization reactions is reduced [Ell01]. At low C_0, solvent molecules predominantly surround the propagating polymer chain. The propagating polymer chain has more time to react with the pendant vinyl group due to its close proximity, facilitating thereby cyclization reactions. Consequently, the increase of Q_{eq} at low C_0 is partially due to the higher concentrations of primary loops that do not contribute to the elasticity of the network [Ell01; Oka94].

Theoretically, C_0 can be used to adjust hydrogel properties, however, this parameter is typically held constant at $C_0 \approx 20\,\text{wt\%}$ mainly due to practical reasons [Buc98]. High water content ensures that crosslinker, such as MBA, can be fully dissolved and that the exothermic free radical polymerization reaction can be properly controlled. Yet, monomer concentration should be high enough to reduce the content of extractables, such as linear polymer chains, oligomers, and unreacted monomers, which have to be rigorously removed in subsequent steps. Consequently, the elastic and swelling properties of hydrogels are commonly tuned by DC and DI to the desired application. Figure 5.4 shows the influence of DC and DI on Q_{eq} of PAM hydrogels in 1 wt% NaCl solution. The 1 wt% NaCl solution corresponds approximately to the concentration of human urine and is commonly used in SAP research as a reference solution to compare Q_{eq} [Buc98].

Higher DC values increase the molar ratio of crosslinker to monomer. Consequently, DC effectively reduces the molecular weight between crosslinks M_c by introducing shorter and more elastic polymer chains. For large $Q_{eq} > 10$, the dependency of Q_{eq} on M_c can be approximated by

$$Q_{eq} = \beta_q M_c^{3/5}\,, \tag{5.2}$$

where β_q is a constant related to the specific volume of the polymer, the specific volume of the solvent, and the Flory-Huggins polymer - solvent interaction parameter [Oye14]. The decrease of Q_{eq} follows a

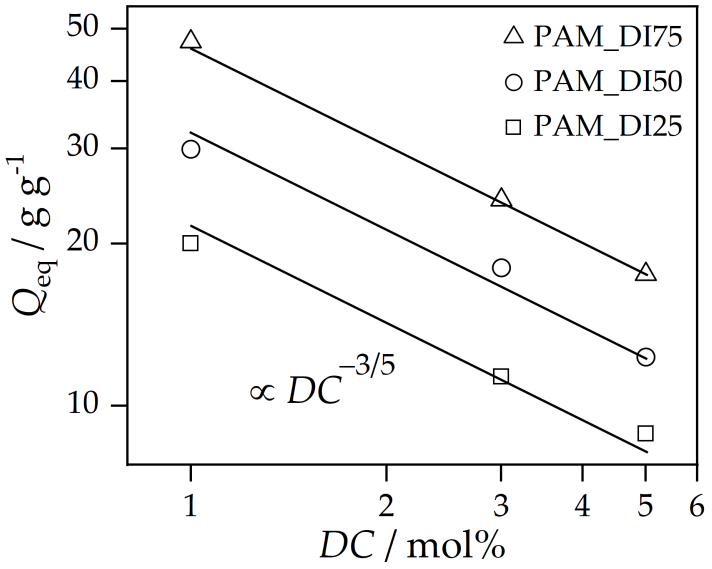

Figure 5.4: Equilibrium swelling capacity Q_{eq} as a function of the degree of crosslinking DC at varying degrees of ionization DI in 1 wt% NaCl solution, displayed on a log-log scale. Solid lines highlight a power law decay of the form $Q_{eq} \propto DC^{-3/5}$ based on the swelling theory (see Equation 5.2). Error bars are within symbol size.

characteristic power law of the form $Q_{eq} \propto DC^{-3/5}$, indicating that DC is inversely proportional to M_c. Consequently, higher crosslinker concentration reduce the average mesh size of the hydrogels.

Variation of DI changes the ratio of monomer to charged co-monomer in the pre-gel composition, controlling thereby the charge density of the formed hydrogel network. This increase is independent of DC and rises linearly by a factor of two from $DI = 25$ to 75 mol%. A convergence of Q_{eq} to a plateau value as a function DI, as typically observed in PSA based hydrogels at approximately $DI > 75$ mol%, was not observed. This convergence arises from the condensation of counterions onto the polyelectrolyte backbone above a certain charge density threshold. This phenomenon was first described by Manning, who introduced the threshold value of counterion condensation by the dimensionless Coulomb coupling strength

$$\Gamma = \frac{\lambda_B}{l_m} > 1\,, \tag{5.3}$$

where λ_B is the Bjerrum length and l_m is the distance between neighboring monomer units [Man69]. The Bjerrum length describes the length at which the magnitude of electrostatic interactions are on the order of the thermal energy kT given by

$$\lambda_B = \frac{e^2}{4\pi\epsilon_0\epsilon_r kT}\,, \tag{5.4}$$

where e is the elementary charge, ϵ_0 is the vacuum permittivity and ϵ_r is the relative dielectric constant of the medium (≈ 80 for water at room temperature) [Owe61; Yan03]. Coulomb interactions dominate over thermal interactions when $\Gamma > 1$, favoring counterion condensation as a result. In water, the Bjerrum length is $\lambda_B \approx 7$ Å. Since the cationic group of PAM hydrogels is sufficiently separated from the polymer backbone over six chemical bonds, the distance between cationic charges is still beneath this threshold. Consequently, a flattening of the Q_{eq} curve as a function of DI was not observed even at high charge densities.

Note that in context of anionic PSA based hydrogels, charge density is often denoted by the degree of neutralization DN as a synthetic parameter. DN is calculated similarly to DI (see Equation 4.4, p. 35), except that the molar amount of NaOH is used instead of the charged co-monomer. NaOH deprotonates AAc forming in-situ the charged sodium acrylate co-monomer that undergoes crosslinking copolymerization with AAc.

Neutralization refers here to the chemical reaction of an acid and base.

In addition to Q_{eq}, the swelling rate is an another application-relevant property. The spherical shape of the synthesized PNVF and PVAm hydrogel particles allows for rather simple monitoring of swelling kinetics using a digital microscope, which measures the time-evolution of the diameter during swelling. The influence of particle size and charge density on the swelling rate of PNVF and PVAm hydrogels was studied. Section B.1.1, p. 111 describes the measurement technique in detail.

Figure 5.6 shows the time-evolution of the normalized PNVF particle volume during swelling for three different dry particle radii. Swelling of the particles can be described by an exponential first-order kinetic function. The characteristic swelling constant τ_s increases with larger initial dry particle sizes from 140 s to 920 s for a dry particle radius of 100 µm and 380 µm, respectively.

Swelling in SAPs is predominantly a diffusion process, and therefore, is governed by the random statistical motion of molecules in space towards regions with lower concentraiton. Water molecules spread out from the surface into the SAPs particles because the concentration is lower inside the particles. Simultaneously, polymer chains of the SAP network move in opposite direction, creating additional volume for the water molecules, as illustrated in Figure 5.5 [Tan79]. Polymer chains are larger than water molecules, and therefore, they diffuse slower. [Buc98]. Moreover, in SAPs polymer chains are interconnected through covalent bonds which further reduces diffusion by forcing cooperative movement. Consequently, the slow diffusion of polymer chains is the rate-limiting process during swelling. The absorption process is ultimately counterbalanced by elastic forces of the elongated polymer network when Q_{eq} is reached.

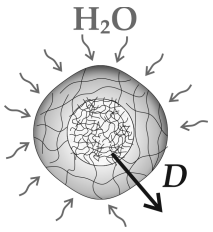

Figure 5.5: Spherical particle swelling with D the diffusion coefficient of expanding polymer chains.

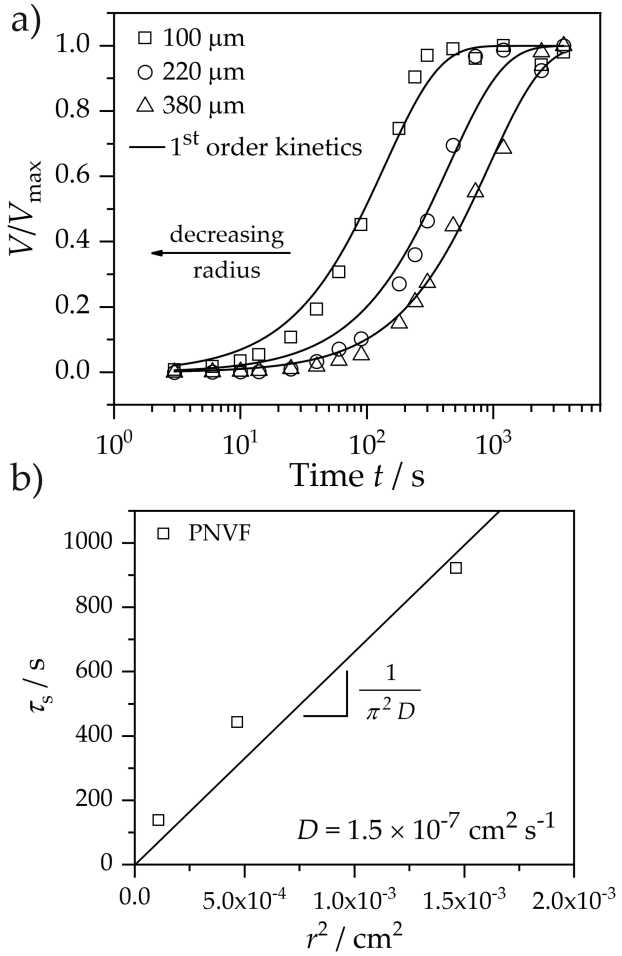

Figure 5.6: Swelling kinetics of PNVF hydrogels with $DC = 2\,\text{mol\%}$ and varying dry particle sizes. a) Normalized particle volume as a function of swelling time in deionized water. Solid lines are least-squares first-order kinetic fits with characteristic swelling times of $\tau_s = 140$, 440, and 920 s for dry particle sizes 100, 220, and 380 µm, respectively. b) Dependence of the characteristic swelling constant τ_s on the dry PNVF particle radius. The solid line is a least-squares linear fit with zero intercept (slope $= 663\,000 \pm 72\,000\ \text{s cm}^{-2}$; $R^2 = 0.98$). Diffusion coefficient D was calculated from the slope according to Equation 5.6, yielding a value of similar order of magnitude as common PSA based hydrogels [Buc98].

The concentration-dependent diffusion process can be described by Fick's law according to which the diffusion flow rate f is related to the concentration gradient $\mathrm{d}c/\mathrm{d}x$ by

$$\frac{f}{A} = -D\frac{\mathrm{d}c}{\mathrm{d}x}\,, \tag{5.5}$$

where A is the cross-sectional area of the sample and D is the diffusion coefficient. D is assumed to be constant and depends on the polymer network structure, such as the crosslinking density and extent of ionization [Buc98].

The characteristic swelling constant τ_s obtained by the first-order kinetic expression relates to D by

$$\tau_s = \frac{r^2}{\pi^2 D}, \tag{5.6}$$

where r is the radius of the dry, unswollen hydrogel particle [Buc98]. Figure 5.6 further shows the dependence of τ_s on the quadratic radius of the dry PNVF particles. In accordance to Equation 5.6, this dependency follows a linear trend. From the slope obtained by linear regression analysis, D was roughly estimated to 1.5×10^{-7} cm^2 s^{-1}, which is a similar order of magnitude as common PSA based hydrogels [Buc98].

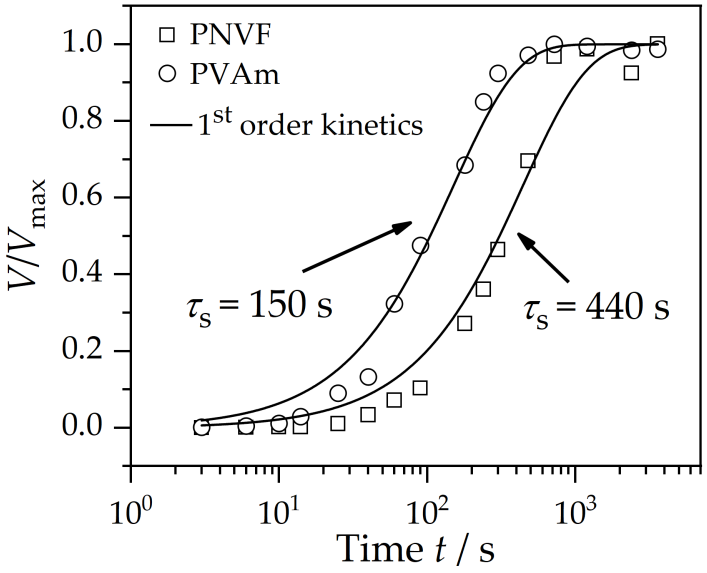

Figure 5.7: Influence of charged polymer backbone on swelling kinetics. Normalized particle volume of a PNVF and PVAm particle as a function of swelling time. PNVF and PVAm particle radius is similar with $\approx$ 220 µm. Solid lines are least-squares first-order kinetic fits with characteristic swelling time constants of τ_s = 440 s and 150 s for PNVF and PVAm particles, respectively.

To elucidate the influence of the charged polymer backbone on swelling, the swelling rate of PNVF precursor particles was compared to the subsequently formed cationic PVAm particles, avoiding thereby any influences of the underlying network structure as the hydrolysis of PNVF to PVAm only affects the chemical structure of the side groups. Figure 5.7 compares the swelling kinetics of PNVF and PVAm gels with similar particle radius of 220 µm. The characteristic swelling time constant decreases by a factor of ≈ 3 from 440 s to 150 s for PNVF and PVAm hydrogels, respectively. This distinct reduction arises from the presence of cationic charges in PVAm hydrogels, facilitating thereby the diffusion of polymer chains towards the surrounding solution by electrostatic repulsions of neighboring cationic charges.

5.2 EFFECT OF SALT CONCENTRATION AND ION VALENCY ON SWELLING

In addition to studies of topological and morphological influences on the swelling capacity, it is essential to understand whether the ionic composition of the surrounding solution can lead to distinct changes of Q_{eq}. To elucidate whether Q_{eq} of the synthesized cationic hydrogels is affected by seawater, water absorbency measurements were performed for varying seawater concentrations and compared to NaCl solution. The seawater composition was adopted from the standard procedure given by ASTM International, containing the most prominent salts NaCl (24.5 $g\,L^{-1}$), $MgCl_2$ (5.2 $g\,L^{-1}$), Na_2SO_4 (4.1 $g\,L^{-1}$), and $CaCl_2$ (1.2 $g\,L^{-1}$) [Cai21]. The concentration was adjusted by diluting the stock solution, maintaining thereby the ratio of different salts throughout the concentration series. Figure 5.8 shows the dependency of Q_{eq} on NaCl solutions and seawater at varying salt concentrations for anionic PSA, cationic PAM and PVAm hydrogels.

Monovalent ions screen electrostatic interactions.

In NaCl solution, increasing salt concentration decreases Q_{eq} independent of the chemical structure of the hydrogel according to a characteristic power law decay of the form $Q_{eq} \propto c_{NaCl}^{-0.4}$, highlighted by the solid lines in Figure 5.8. This power law dependence resembles the concentration dependency of the Debye length $\lambda_D \propto c_{salt}^{-1/2}$, suggesting that screening of electrostatic repulsive interactions between neighboring monomer units by monovalent ions predominantly affects Q_{eq}. At higher salt concentration, Na^+ and Cl^- ions diffuse into the gel phase, increasing thereby the concentration of mobile ions inside the gel phase, which results in a reduction of λ_D. The salt concentration dependency of λ_D is, however, strictly valid only for linear polyelectrolytes and at high dilution. Therefore, the slight deviation from the theoretical value of the exponent $-1/2$ presumably arises from the highly crosslinked network structure [Are19a; Mus19a].

In contrast to NaCl solutions, the effect of seawater on Q_{eq} highly depends on the chemical structure of the hydrogel. While PAM hydro-

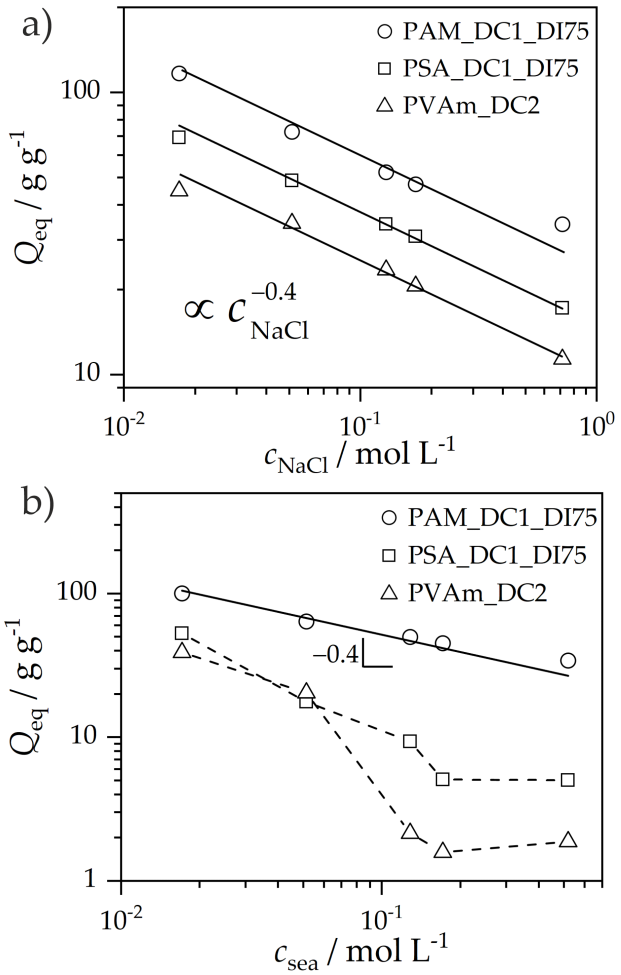

Figure 5.8: Salt concentration dependency of the equilibrium swelling capacity Q_{eq} in sodium chloride solution (a) and seawater (b). Solid lines highlight a power law dependency of the form $Q_{eq} \propto c_{NaCl}^{-0.4}$ resembling the theoretical description of the screening of electrostatic interactions based on the Debye length $\lambda_D \propto c_{salt}^{-1/2}$. The theory is only strictly valid for long linear polyelectrolytes, and therefore, slight deviations are expected for crosslinked networks [Are19a]. Seawater has no effect on the swelling of cationic PAM based hydrogels, whereas induces a rapid decrease for PSA and PVAm hydrogels. Dashed lines are a guide to the eye. Error bars are within symbol size.

gels exhibit the same swelling behavior in seawater and NaCl solution, PSA and PVAm hydrogels show a facilitated decrease of Q_{eq} in seawater. At 0.13 mol L^{-1} salt concentration, the switch from NaCl solution to seawater reduces Q_{eq} by a factor of 4 and 10 for PSA and PVAm hydrogels, respectively. This seawater induced deswelling of PSA and PVAm hydrogels implies that divalent ions, such as Mg^{2+}, Ca^{2+}, and

SO_4^{2-} ions, interact with the polymer backbone, leading to a reduction of Q_{eq}.

To further specifically study the role of divalent ions, PSA and PVAm hydrogels were swollen in pure $MgCl_2$ and Na_2SO_4 solutions with varying salt concentrations, as shown in Figure 5.9. The $MgCl_2$ molar concentration in seawater exceeds the concentration of $CaCl_2$ fivefold and was therefore chosen to represent cationic divalent ions.

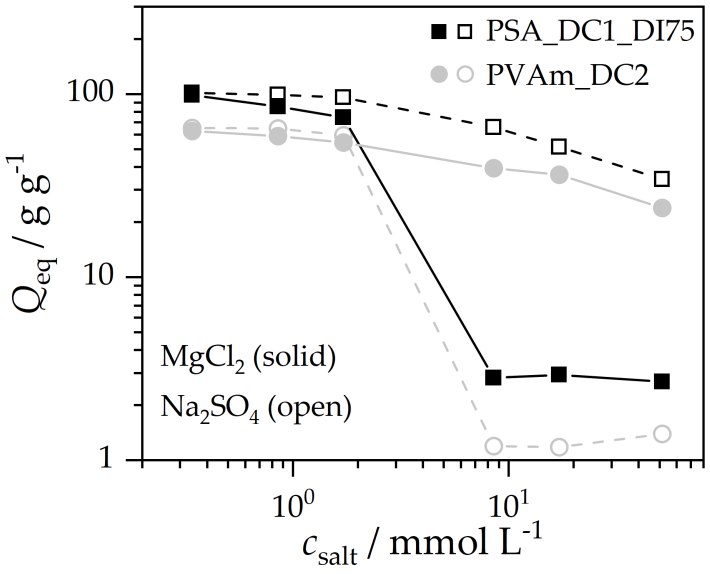

Figure 5.9: Equilibrium swelling capacity of PSA and PVAm hydrogels as a function of divalent ion concentration. Dashed and solid lines are a guide to the eye, representing Na_2SO_4 and $MgCl_2$ solutions, respectively. Error bars are within symbol size. Anionic PSA hydrogels are sensitive towards Mg^{2+} ions and cationic PVAm hydrogels towards SO_4^{2-} ions. Both show a rapid volume transition at $c_{salt} = 2$ mmol L^{-1}, suggesting attractive electrostatic interactions between the polymer backbone and divalent counterions.

Divalent ion-induced volume transition

Divalent salt ions with similar charge as the polymer backbone induce a gradual decrease of Q_{eq}, which can be attributed to the reduction of λ_D. Addition of multivalent counterions, however, induces a rapid volume transition of the hydrogels at a certain critical concentration of $c_{cr} = 2$ mmol L^{-1} to a Q_{eq} plateau value in the range $1 - 3$ g g^{-1}. This counterion-induced volume transition suggests attractive electrostatic interactions between the polymer backbone and divalent ions.

Ca^{2+} ions promote PSA polymer chain aggregation.

Structural studies on PSA hydrogels using anomalous small-angle X-ray scattering have shown that divalent Ca^{2+} ions have a stronger affinity towards the negatively charged PSA polymer backbone compared to monovalent Na^+ ions. Essentially, Ca^{2+} ions occupy the immediate neighborhood of the charged carboxylate groups [Horo6],

reducing the ion cloud around the polymer backbone. Furthermore, small-angle neutron scattering measurements have revealed structural changes induced by the Ca^{2+} / Na^{+} ion exchange in PSA hydrogels. Accordingly, increasing Ca^{2+} ion concentrations increase the correlation length of polymer chains from 19 Å to 81 Å, which implies enhanced polymer chain aggregation until the onset of phase separation [Mus19a]. These findings are consistent with other charged materials, such as DNA strands, where divalent counterions form a partially localized cloud around the DNA strand that is thinner than the effective Debye screening length [Mor04].

In terms of thermodynamic properties, it has been shown by osmotic pressure experiments that the addition of Ca^{2+} ions predominantly affects the polymer-solvent interaction parameter χ within the osmotic pressure mixing term (see Equation 2.6, p. 14), reducing thereby both the solubility of polymer chains and the solvent quality of the surrounding solution [Hor00; Hor01; Mus19b]. The effect of Ca^{2+} ion-induced volume transition is reversible and depends on the ratio of monovalent to divalent ions [Mus19a]. The ion-induced volume transition is attenuated in seawater that consists primarily of monovalent Na^{+} and Cl^{-} ions, as shown in Figure 5.8. This attenuation of the phase transition indicates that monovalent ions compete with divalent ions for the charged side groups of the polymer backbone.

Transition metals form ionic crosslinks.

In contrast to divalent alkaline earth metal cations, divalent transition metal cations, such as Co^{2+} and Ni^{2+} ions, induce an irreversible network collapse of swollen PSA hydrogels [Hor01]. Rheological measurements have shown that Co^{2+} increases the elastic modulus of the swollen PSA hydrogels [Hor01]. The existence of partially filled d-orbitals in transition metal ions allows for the formation of coordination complexes consisting of a central metal atom, which binds to several donor ligand atoms. In PSA gels, carboxylate groups function as ligands that can form intermolecular crosslinks (i. e., ionic bridges) between neighboring polymer chains. Therefore, the increase of the elastic modulus as a function of transition metal ion concentration arises from the formation of intermolecular metal complexes that increase the crosslink density of the hydrogel. Consequently, the PSA polymer network acts as a polychelate, resembling an intrinsic property of polyelectrolytes that has been extensively exploited in wastewater treatment applications [Roy11; Pak18b; Pak18a].

The effect of monovalent, divalent, and transition metal salt counterions on the swelling behavior of polyelectrolyte hydrogels can be classified into three characteristic mechanisms. Monovalent ions screen the repulsive electrostatic interactions between neighboring charged monomer units by reducing the Debye length. Monovalent ions move freely according to Brownian motion throughout the gel phase, which has been quantified by ^{23}Na NMR relaxation studies [Guo19b; Guo19a].

Divalent alkaline earth metal counterions form a dense cloud around the polymer chain, promoting thereby polymer chain aggregation. Figure 5.9 suggests that this behavior is universal for highly charged polyelectrolytes as cationic PVAm hydrogels are similarly affected by divalent SO_4^{2-} anions. Transition metal ions form coordination complexes with the polyelectrolyte backbone, affecting both the elastic and mixing term of the osmotic pressure function.

Interestingly, the PAM hydrogels with the cationic quaternary ammonium side group do not show an ion-induced volume transition in seawater. This resistance to seawater presumably arises from the bulkiness of the trimethylammonium group that prevents an effective charge neutralization by divalent SO_4^{2-} anions. Future work could systematically postmodify PVAm hydrogels, for instance, with glycidyl trimethylammonium chloride (see Figure 5.10 for chemical structure) to elucidate the relationship between cationic side group functionality and swelling capacity. The amine groups of the PVAm backbone exhibit a high reactivity with the epoxide group [Hug01], and therefore, dry PVAm can be simply swollen in aqueous glycidyl trimethylammonium chloride solution for the postmodification. The swelling capacity of this modified PVAm hydrogels in seawater should gradually increase with the concentration of the glycidyl trimethylammonium chloride solution when the trimethylammonium functionality plays the pivotal role in the seawater resistant properties.

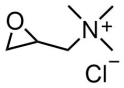

Figure 5.10: Chemical structure of glycidyl trimethylammonium chloride.

6

DYNAMIC-BASED ASSESSMENT OF NETWORK STRUCTURE USING NMR RELAXOMETRY

Abstract Understanding the polymer network structure over multiple length and time scales is essential for the development of advanced hydrogel materials. This chapter explores the application of both ^{1}H double quantum (DQ) and T_2 relaxation NMR techniques to assess the crosslinking density and network heterogeneity of the synthesized hydrogels. The analysis of network heterogeneity requires the inversion of DQ build-up and T_2 relaxation curves, which is a mathematical ill-posed problem. A regularization approach based on the CONTIN algorithm to obtain the respective distributions is discussed. Particular attention is paid to the topological analysis of the synthesized PVAm core - shell particles. The obtained regularized T_2 distributions indicate the gradual formation of rigid domains at higher degrees of surface-crosslinking. This finding implies that the rigid shell and flexible core of the PVAm particles exhibit a distinct molecular mobility, which can be quantified by T_2 relaxation curves.

6.1 IMPROVED PROTOCOL FOR THE REGULARIZED INVERSION OF TIME-DOMAIN NMR DATA

Using free radical crosslinking copolymerization for the synthesis of hydrogels leads to a pronounced nanoscopic network heterogeneity with characteristic topological features, such as dangling ends and loops (see Section 2.2, p. 10) [Lit01; Höp14; Sei17b]. Understanding synthetic origins of those inhomgeneities and their effect on mechanical properties, such as optical clarity, mechanical strength, and permeability, is essential for establishing rational synthetic design principles of hydrogels.

Low-field TD NMR has been used as non-invasive technique to obtain nanoscopic insights into the network structure by probing the local molecular mobility of polymer segments. Two important application of NMR techniques have been used in hydrogels. During hydrogel formation three different domains with characteristic molecular dynamics are formed that can be classified into rigid mesh structure consisting of polymer chains between crosslinks, mobile network defects consisting of loops and dangling ends, and extractables consisting of oligomers, linear polymer chains, and residual solvent. These characteristic domains are typically reflected in multi-exponential T_2 relaxation curves

and DQ build-up curves, and therefore, ^{1}H TD NMR can be used to quantify the relative fraction of those components

In T_2 relaxation curves, the heterogeneity of samples can be represented by a weighted sum of exponential decays, a stretched exponential function, and their combination, that capture the varying relaxation behavior of network strands. In the limit of a large number of relaxation behavior as observed in free radical polymerized hydrogels, the T_2 relaxation times can be more precisely described by a distribution funciton $f(T_2)$. The unknown $f(T_2)$ can be calculated from the measured exponentially decaying NMR signal $g(\tau)$ using a first-kind Fredholm integral equation given by

$$g(\tau) = \int_0^\infty \exp(-\frac{\tau}{T_2}) f(T_2)\, \mathrm{d}T_2 \quad f(T_2) \geq 0\,. \tag{6.1}$$

The numerical solution of Equation 6.1 is not trivial as it is strongly related to the inverse Laplace transformation (ILT), which is a mathematical ill-posed problem. Consequently, for a given data set with finite noise, a large set of solutions exist that describe the measured data within the noise level. To resolve this ill-posed problem and reduce overfitting, regularization procedures can be applied. Regularizations add further fitting constraints that have to be simultaneously satisfied, narrowing down the set of potential solutions by adjusting the strength of the regularization parameter. A common regularization algorithm used in NMR data analysis is the CONTIN algorithm [Pro82; Kro86; Bor94; Bar01; Day11]. Inspired by previous attempts to emulate this algorithm in other programming languages, such as MATLAB [Sco15], this dissertation aims to design a MATLAB emulation of the CONTIN algorithm for the regularized inversion of T_2 relaxation and DQ build-up curves.

The first step of the CONTIN algorithm discretizes Equation 6.1 by

$$\mathrm{g_m} = A_{\mathrm{m,n}} \mathrm{x_n}\,, \tag{6.2}$$

where $\mathrm{g_m}$ is a vector of size m containing the measured NMR signal, $\mathrm{x_n}$ is a vector of size n representing the unknown T_2 relaxation time distribution, and $A_{\mathrm{m,n}} = \exp(-\tau_\mathrm{n}/T_{2,\mathrm{m}})$ is the kernel matrix. $A_{\mathrm{m,n}}$ maps the T_2 distribution $\mathrm{x_n}$ onto the observed NMR signal. Solving a classic least-squares minimization problem yields $\mathrm{x_n}$. The CONTIN algorithm further regularizes this minimization problem by adding a second term, so-called regularizor, to impose a priori knowledge of the solution. Based on the principle of parsimony, the curvature of the solution, computed by the discretized second differential operator matrix L_2, can be used as a side constraint. The addition of this regularizor leads to the least-squares minimization-problem

$$\mathrm{x}_\lambda = \arg\min\{\|\mathrm{g_m} - A\mathrm{x_n}\|_2^2 + \lambda^2 \|L_2 \mathrm{x_n}\|_2^2\}\,, \tag{6.3}$$

where x_λ is the regularized solution for a certain λ, λ is the regularization parameter, and $\|\cdot\|_2$ is the Euclidean norm. The first term is the residual norm, which is regularized by the second term. Highly erratic solutions will significantly contribute to the second term, and therefore, are more likely to be rejected from the set of solutions. The strength of this regularizor is controlled by λ, which essentially functions as a smoothing parameter and has to be chosen appropriately to balance the minimization of the residual norm and the regularizor. At $\lambda = 0$ a classic least-squares minimization is performed with a high tendency towards erratic solutions (i. e., under-fitting), which will likely lead to an overinterpretation of the data. In contrast, large λ values over-smooth the solution, resulting in a loss of valuable information.

The designed MATLAB implementation of the CONTIN algorithm determines optimal λ-values by the L-curve approach, a convenient technique that proved to be successful in related inversion problems, such as in diffusion NMR and light scattering data analysis [Han93; Baro1; Day11; Sco15]. In the L-curve approach, the (semi)norm of the regularized solution $\|L_2 x_\lambda\|_2$ is plotted against the residual norm $\|g_m - A x_\lambda\|_2$ for an array of λ values typically ranging from 10^{-3} to 10^2. This relationship yields a characteristic L-shaped curve when displayed as a log-log scale. At the vertical part, $\|L_2 x_\lambda\|_2$ is sensitive towards small variations of λ, indicating that perturbation errors dominate the regularized solution. In contrast, at the horizontal part, $\|g_m - A x_\lambda\|_2$ is sensitive towards λ variations, suggesting that regularization errors dominate the solution. The optimal λ value is located at the corner of the L-curve, and therefore, serves as a compromise between the erratic and over-smoothed solution. Figure 6.1 shows an example of the L-curve and T_2 distributions for different λ values, emphasizing the balance between erratic and over-smoothed solutions. The data was obtained from sample PVAm_DC2.

Solving the aforementioned regularized minimization problem and determination of the optimal λ value by the L-curve approach was realized by a MATLAB algorithm. The designed algorithm consists of three distinct sections. The structure of the algorithm has been previously described in detail by Scotti and coworkers [Sco15].

Section 1 normalizes raw data.

Section 1 reads and normalizes the raw data of the measured T_2 relaxation curves. If desired, a mono-exponential fit at long $\tau_{echo} \geq 100$ ms can be performed to quantify highly mobile components, such as residual solvent. This tail is subtracted first from the raw data, which is subsequently re-normalized to the maximum value. The T_2 relaxation curves of hydrogels are typically measured by a combination of multiple experiments with varying pulse spacing (see Section B.3.2, p. 112) [Höp14; Are19b]. The experiments are combined in one data set, which leads to regions with high data point densities due to the overlapping of data sets. To ensure an even distribution

of data points, and therefore, avoid the statistical over-weighting of this high point density regions, section 1 interpolates the T_2 relaxation curves using logarithmic equally spaced τ_{echo}.

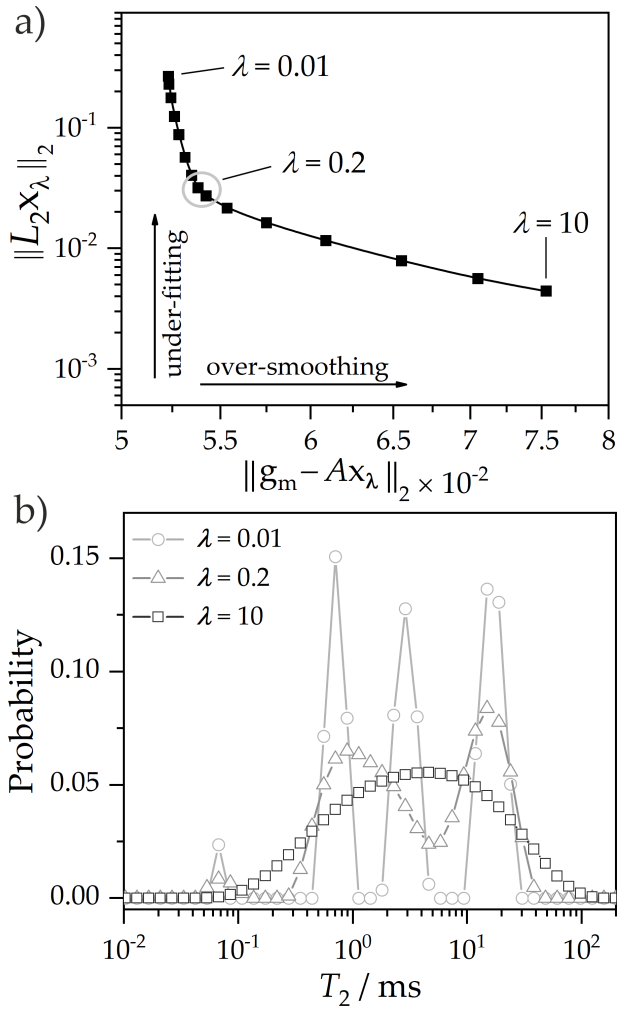

Figure 6.1: Use of the L-curve approach to find the optimal regularization parameter λ. Exemplary for sample PVAm_DC2 to highlight the importance of the regularization parameter λ. a) Solution norm as a function of the residual norm for varying λ values obtained by solving Equation 6.3, p. 54, displayed on a log-log scale. Red circle marks the optimal $\lambda = 0.2$. b) Corresponding T_2 distributions obtained by regularized inversion of T_2 relaxation curves with varying λ, indicating the need to balance between erratic and over-smoothed solutions. Figure adapted from [Fen22b].

Section 2 solves minimization problem.

Section 2 sets the initial regularization parameters, such as the number of points and range of the T_2 distribution, the array of λ values, and the kernel matrix. Subsequently, it performs the regularized inversion for varying λ values by solving Equation 6.3, p. 54 with the Nelder-Mead algorithm [Nel65]. It further calculates the residual

norm and solution norm for every λ value, which are then used in the L-curve method.

Section 3 finds regularization parameter.

Section 3 plots the L-curve and calculates the optimal λ value at the corner using the l_corner algorithm inside the Matlab regularization tool package developed by Hansen, as illustrated in Figure 6.1 [Han94]. It then performs the regularized inversion with the optimized λ value and generates the output file consisting of all the used data sets, parameters, and results.

Inversion of DQ build up curves

The aforementioned sections of the regularized inversion algorithm were described for T_2 relaxation curves as an example. However, the algorithm is not limited to T_2 relaxation curves and can be easily adjusted towards other related inversion problems by switching the kernel matrix. In addition to the classic T_2 relaxation measurements, proton double quantum NMR has significantly advanced the quantitative use of TD NMR techniques in elastomers [Saa05; Saa07; Guo18]. ^{1}H DQ NMR measures the intensity build-up of DQ coherences, which are only excitable in the presence of ^{1}H–^{1}H dipolar couplings that are related to the orientation of polymer chain segments and their dynamics [Saa12]. While the time-averaged dipolar couplings of isotropic mobile polymer chains approach zero on the timescale of the NMR experiment, a finite residual dipolar coupling D_{res} persists in crosslinked networks. D_{res} depends on the molecular weight between crosslinks, and therefore, is related to the crosslink density [Lan11; Cha12b]. The distribution of D_{res} can be used as measure of network heterogeneity [Cha11]. It has been shown that a modified inverted Abragamian-like function (A-l kernel)

$$K(\tau_{\text{DQ}}, D_{\text{res}}) = 0.5(1 - \exp(-(0.378 D_{\text{res}} \tau_{\text{DQ}})^{1.5}) \times \cos(0.583 D_{\text{res}} \tau_{\text{DQ}})) \tag{6.4}$$

can be used for regularized DQ build-up curve fits, where τ_{DQ} is the DQ evolution time [Cha11]. The aforementioned Matlab algorithm was adjusted for the calculation of D_{res} distributions using the A-l kernel. The general algorithm structure of the regularized inversion remains the same.

6.2 NETWORK STRUCTURE ANALYSIS BY DOUBLE QUANTUM NMR

The quantification of the nanoscopic network structure and topology remains a longstanding challenge in hydrogel research. While scattering techniques are useful to elucidate network heterogeneities beyond the nanometer scale [Sei17c], they cannot reveal the local network structure on length scales ≤ 10 nm. This length scale directly relates to the mesh size of the polymer network and topological defects, such as loops and dangling ends, and therefore, the local network structure ties greatly to mechanical properties. Its quantification is essential

to advance our molecular understanding of the hydrogel network structure.

In the last two decades, the use of proton DQ NMR to assess chain dynamics and topological constraints in polymeric soft matter has been extensively explored [Saa07; Höp14; Guo18]. For soft matter analysis, DQ pulse sequences are commonly performed on low-field time-domain NMR setups addressing homonuclear ^{1}H–^{1}H dipolar couplings of neighboring protons (≈ 1.8 Å). The orientation of neighboring protons of a monomer unit with respect to the external magnetic field primarily dictates the magnitude of their dipolar coupling. As a result, dipolar couplings reflect segmental orientation fluctuations of the polymer backbone from which information about local molecular mobility and topological constraints can be inferred. Dipolar couplings in chemically crosslinked networks are not averaged to zero within the timescale of the NMR experiments as spatial constraints imposed by chemical crosslinks lead to an anisotropic motion. As a result, a finite residual dipolar coupling D_{res} is observed, which is directly related to the crosslink density of the polymer network.

This dissertation explores the effect of synthetic parameters on the mesh size distribution using DQ NMR. Therefore, the recorded DQ build-up curves are inverted using the aforementioned regularization method. Monodisperse, spherical PNVF particles serve as a model system, since their spherical shape allows for uniform swelling during sample preparation. Moreover, the acid hydrolysis of PNVF particles incorporates charges into the backbone structure without affecting the underlying crosslink density, ensuring thereby the systematic study of charge density on the segmental mobility.

DQ NMR data treatment

An advantage of DQ NMR is that the DQ pulse sequence acquires two different signal functions, a reference decay curve I_{ref} and a double quantum signal I_{DQ} measured as a function of the DQ evolution time τ_{DQ}. I_{ref} typically exhibits a long time tail I_{tail} following a mono- or bi-exponential decay that can be associated with isotropically mobile components, such as defects and solvent [Saa18]. Crosslinked polymer chains are encoded in I_{DQ} with D_{res} as a characteristic rate constant. I_{DQ} exhibits a long time relaxation that is removed by normalizing the defect-corrected sum intensity that yields the DQ build-up curve

$$I_{\text{nDQ}} = \frac{I_{\text{DQ}}}{I_{\text{DQ}} + I_{\text{ref}} - I_{\text{tail}}}\,. \tag{6.5}$$

I_{nDQ} approaches the intensity 0.5 and is only governed by the magnitude and distribution of D_{res}. Note that the experimentally obtained I_{DQ} decays towards the noise level within 20 ms, leading to highly scattered data of I_{nDQ} beyond this point. It has been shown that I_{tail} can be reliably inferred from a tri-exponential fit on a reduced data set $I_{\text{ref}} - I_{\text{DQ}}$, which only considers single-quantum coherences related to uncoupled mobile components and network defects [Guo18].

Compared to a commonly performed stepwise fitting approach where arbitrary fitting ranges are selected manually by the researcher, this tri-exponential function allows for an automation of the data analysis, reducing thereby potential subjective errors in the data treatment. The tri-exponential function

$$I_{\mathrm{ref}} - I_{\mathrm{DQ}} = A_{\mathrm{net}} \exp(-a\tau_{\mathrm{DQ}}) + B_{\mathrm{def}} \exp(-b\tau_{\mathrm{DQ}}) + C_{\mathrm{sol}} \exp(-c\tau_{\mathrm{DQ}}) \tag{6.6}$$

was used to infer $I_{\mathrm{tail}} = B_{\mathrm{def}} \exp(-b\tau_{\mathrm{DQ}}) + C_{\mathrm{sol}} \exp(-c\tau_{\mathrm{DQ}})$. B_{def} is the defect fraction, and C_{sol} is the sol fraction with b and c the respective decay rate constants. $A_{\mathrm{net}} = 1 - B_{\mathrm{def}} - C_{\mathrm{sol}}$ is the network fraction. The term sol refers to highly mobile uncrosslinked components, such as linear polymer chains, oligomers, residual monomer, and solvent as HDO. As $I_{\mathrm{ref}} - I_{\mathrm{DQ}}$ considers only single-quantum coherences, A_{net} does not provide the actual fraction of crosslinked polymer chains but serves rather as a rough estimate of rigid components in the network. Section B.3.3, p. 114 explains experimental parameters and data acquisition of the used ^{1}H DQ NMR pulse sequence. Figure 6.2 shows the fitting and normalization procedure used to acquire the DQ build-up curve of sample PNVF_DC2.

The tri-exponential fit on sample PNVF_DC2 yields relaxation rates $b = 169\ \mathrm{s}^{-1}$ and $c = 27\ \mathrm{s}^{-1}$ for the defect and sol fraction, respectively. $b \gg c$ supports the assumption that defects, such as loops and dangling ends, relax faster than mobile sol components as their mobility is stronger constrained due to at least one chemical crosslinking point. Similar relaxation rates have been found in PSA based hydrogels [Guo18]. Figure 6.2 further shows the obtained structural parameters A_{net}, B_{def}, and C_{sol} as a function of DC. A_{net} increases linearly from 22 % at $DC = 1$ mol% to 45 % at $DC = 3$ mol% while B_{def} decreases from 51 % to 39 %. This increase of the A_{net} to B_{def} ratio indicates an increase of crosslinking-efficiency at higher crosslinker concentrations.

The fraction of C_{sol} is $\approx$ 20 %. This value is very high compared to PSA based hydrogels where C_{sol} values of $\approx$ 5 % have been found [Guo18]. C_{sol} has been mainly associated with HDO solvent, formed by the hydrogen–deuterium exchange between carboxylic acid groups and D_2O solvent. This exchange, however, cannot solely explain the high C_{sol} value found in PNVF hydrogels. Additional contributions to C_{sol} presumably arise from uncrosslinked linear polymer chains, oligomers, and unreacted monomers. The synthesized PNVF hydrogels were swollen in an excess of deionized water over four days to extract the sol. The water was changed daily, yet the chosen time-interval was presumably not long enough to ensure full extraction. Further NMR experiments could monitor C_{sol} as a function of washing time over several weeks to obtain extraction kinetics of low-molecular weight components, testing thereby the aforementioned hypothesis.

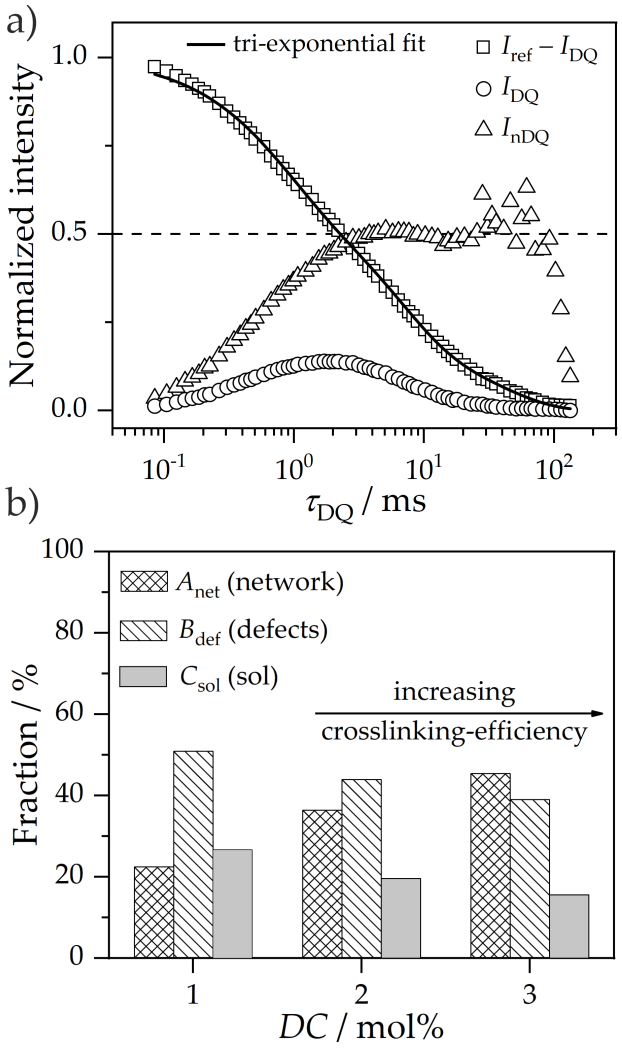

Figure 6.2: a) ^{1}H DQ raw signal I_{DQ}, reduced reference signal $I_{ref} - I_{DQ}$, and normalized I_{nDQ} signal of sample PNVF_DC2 as a function of DQ evolution time τ_{DQ}. The solid line is a least-squares tri-exponential fit according to Equation 6.6 with structural parameters $A_{net} = 36\,\%$, $B_{def} = 44\,\%$, $C_{sol} = 20\,\%$, $a = 1385\ s^{-1}$, $b = 169\ s^{-1}$, and $c = 27\ s^{-1}$. I_{nDQ} was calculated by Equation 6.5. Dashed line highlights intensity at 0.5 as reference. b) Structural parameters for varying *DC*. The ratio of network to defect fraction increases with higher *DC*, suggesting an increase of crosslinking-efficiency.

The commonly used gravimetric quantification of sol content in SAPs is a highly intricate procedure which requires at least several grams of materials and proper filtering techniques to ensure enough sensitivity. The NMR based approach could provide a rather simple non-invasive alternative to assess sol extraction kinetics time-efficiently, advancing the design and quality standard assessment of commercial SAPs.

^{1}H DQ NMR measurements were performed to study the effect of DC on D_{res} distributions of PNVF hydrogels from which the nanoscopic network heterogeneity can be inferred. Figure 6.3 shows the I_{nDQ} build-up curves and respective D_{res} distributions obtained by regularized fits using the CONTIN algorithm with an Abragamian-like (A-l) kernel (see Equation 6.4, p. 57).

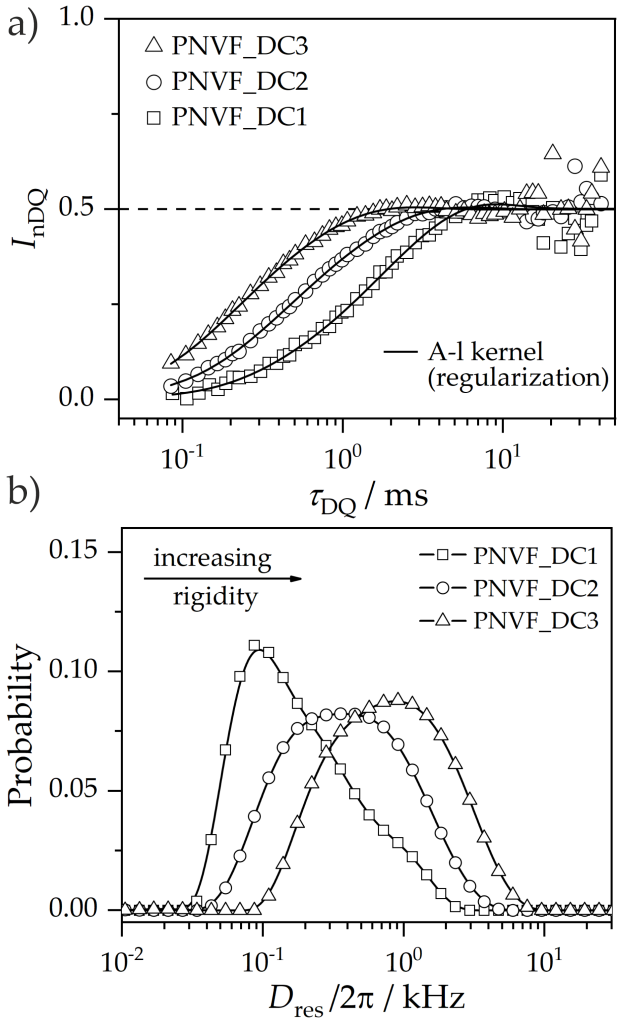

Figure 6.3: a) Normalized I_{nDQ} build-up curves of PNVF hydrogels with varying DC. Solid lines are regularized fits using the CONTIN algorithm with an Abragamian-like (A-l) kernel according to Equation 6.4, p. 57. b) Corresponding residual dipolar coupling D_{res} distributions. Solid lines are a guide to the eye. Discrete sum of D_{res} probabilities equals 1. Table 6.1 shows the geometric mean values and coefficient of variation (i. e., relative standard deviation) CV of the obtained D_{res} distributions.

The DQ build-up curves increase faster and steeper with increasing DC. Higher crosslinker concentrations increase the formation of chemical crosslinks, reducing the mesh-size of the polymer network. This additional crosslinks reduce the conformational flexibility of polymer chains between crosslinking points, which leads to stronger dipolar couplings between neighboring protons of the monomer units.

Evaluation of D_{res} distribution curves

The corresponding D_{res} distributions follow a log-normal distribution function and shift towards higher D_{res} values as a function of DC, confirming the presence of stronger dipolar couplings. The skewness of log-normal distributions can highly distort the arithmetic mean due to the presence of exceptionally large values. Consequently, the geometric mean

$$GM(D_{res}) = e^{\mu}\,, \tag{6.7}$$

which is obtained by antiloging the arithmetic mean μ of the log-transformed D_{res} variable, was used to compare the distributions of different samples. The coefficient of variation (i. e., relative standard deviation) CV of the distributions was used as a measure of network heterogeneity. CV of a log-transformed data set is given by

$$CV(D_{res}) = \sqrt{\exp(\sigma^2_{log}) - 1}\,, \tag{6.8}$$

where σ^2_{log} is the variance of the log-transformed D_{res} variable [Qua03; Nel05; Oli08]. Table 6.1 summarizes $GM(D_{res})$ and $CV(D_{res})$ of the measured samples.

Table 6.1: Calculated mean $GM(D_{res})$ and coefficients of variation $CV(D_{res})$ of log-transformed D_{res} distributions of PNVF and PVAm samples.

Sample	$GM(D_{res})$ (kHz)	$CV(D_{res})$
PNVF_DC1	0.18	1.12
PNVF_DC2	0.38	1.23
PNVF_DC3	0.78	1.14
PVAm_DC1	0.24	1.17

$GM(D_{res})$ of PNVF hydrogels increases by a factor of ≈ 4 from 0.18 kHz at $DC = 1\,\text{mol\%}$ to 0.78 kHz at $DC = 3\,\text{mol\%}$. Higher crosslinker concentrations introduce more chemical crosslinks into the network, reducing thereby the average mesh size of the polymer network. Introducing electric charges into the network by acidic hydrolysis of PNVF_DC1 increases $GM(D_{res})$ to 0.24 kHz for PVAm_DC1, as shown in Figure 6.4. As the crosslinking density of the hydrogels is not influenced by the acidic hydrolysis, this finding suggests that

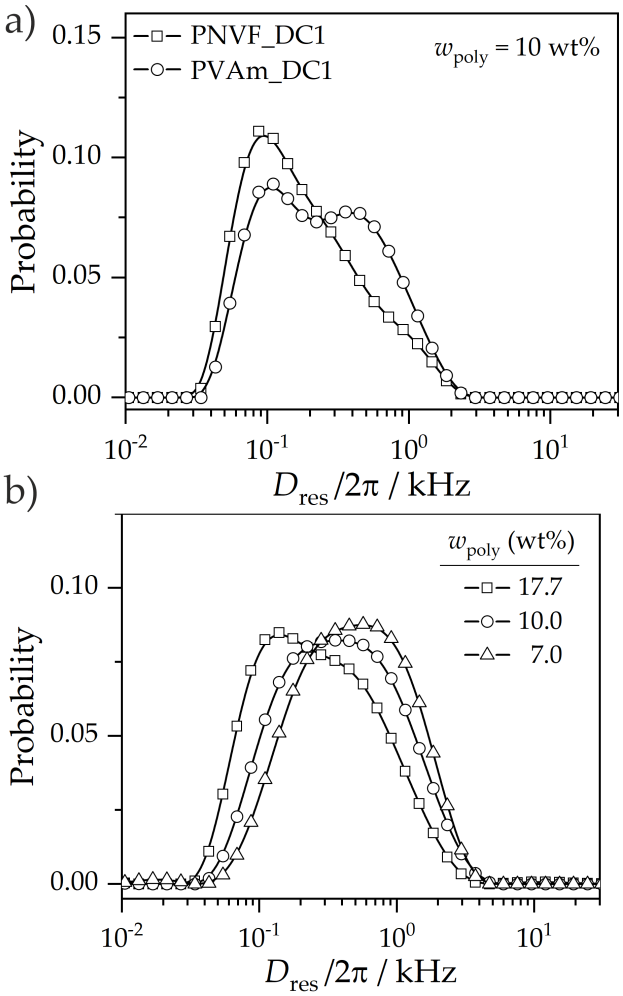

Figure 6.4: Influence of a charged polymer backbone (a) and swelling (b) on the D_{res} distribution of PNVF and PVAm hydrogels. The polymer mass fraction $w_{poly} = 7.0$, 10.0, and 17.7 wt% refer to to the swelling ratios of 1 to 13, 1 to 9, and 1 to 5 in D_2O, respectively.

the reduction in the local mobility of polymer chains arises from electrostatic repulsions between neighboring monomer units.

Figure 6.4 further shows that the extent of swelling during sample preparation affects $GM(D_{res})$. The polymer mass fraction w_{poly} of the hydrogel–D_2O mixture was used to represent the degree of swelling. Slightly swollen PNVF_DC2 particles with $w_{poly} = 17.7$ wt%, resembling a polymer to solvent ratio of 1 to 5, exhibit $GM(D_{res}) = 0.27$ kHz. Increasing swelling of the same sample shifts $GM(D_{res})$ to 0.47 kHz at $w_{poly} = 7.0$ wt%. This finding suggests that the expansion of the network during swelling reduces the conformational flexibility of polymer chains, reflected in higher $GM(D_{res})$ values.

Note that the long length of $\approx$ 100 µs the DQ pulse sequence prevents the quantification of highly rigid components where the

magnetization decay is faster than the shortest DQ cycle time. This phenomenon is already observed for sample PNVF_DC3, as shown in Figure 6.3. The first data point of the DQ build-up starts at an intensity of $\approx 10\,\%$. As a result, the contribution of highly rigid structures with $\tau_{DQ} < 100$ µs is not considered. This exclusion of data points inherently flattens the D_{res} distribution, and therefore, prevents a reasonable comparison of the D_{res} distribution width. Consequently, the here presented DQ pulse sequence cannot be used to study highly rigid topologies, such as surface-crosslinked particles. To overcome this limitation, the use of T_2 relaxation measurements, instead, is subject of the next chapter.

6.3 TOPOLOGICAL INSIGHT INTO CORE-SHELL HYDROGELS

An important postmodification of SAPs is surface-crosslinking. The combination of a loosely crosslinked core with a rigid surface increases application-relevant properties, such as absorbency under load. In common surface-crosslinking methods, SAPs are partially swollen in a crosslinker solution consisting of hazardous chemicals, such as diepoxides and dialdehydes in organic solvents. Moreover, elevated temperatures ($> 70\,^{\circ}C$) are required to facilitate the reactivity of side groups along the backbone, typically carboxylates [Hua06; Moi17; Kim20].

The characterization of this core-shell topology (i. e., extent of surface-crosslinking) is, however, not trivial. Scattering techniques, such as SANS, SAXS, and DLS, and transmission microscopy, have been widely used to determine the core-shell topology of micro-and nanogels with diameters < 100 µm [Nor04; Sei17c]. The topological analysis of macroscopic SAP particles with non-invasive techniques is widely unexplored. This dissertation aims to find an empirical correlation between T_2 relaxation times and the synthetic degree of surface crosslinking ϕ_{shell} (see Equation 4.5, p. 38) from which the core-shell topology can be inferred.

Surface-crosslinking distinctly affects the swelling behavior of hydrogels. Figure 6.5 shows the equilibrium swelling capacity Q_{eq} of neutral PNVF, cationic PVAm, and surface-crosslinked PVAm particles. Q_{eq} of neutral PNVF is in the range $40 - 12\,g\,g^{-1}$ and decreases as a function of *DC*. At higher *DC* more crosslinks are introduced into the network that increase the elastic forces of the network. Acidic hydrolysis of the PNVF network distinctly increases Q_{eq} by a factor of 10 up to $400\,g\,g^{-1}$ due to the incorporation of positively charged ammonium groups. From titration curves, it has been inferred that approximately 70 % of the amine groups are cationic ammonium groups at $pH = 7$ [Pel14]. The high concentration of counterions increase the osmotic pressure difference between the gel and the surrounding solution, enhancing thereby the swelling capacity. Q_{eq} decreases gradually as a

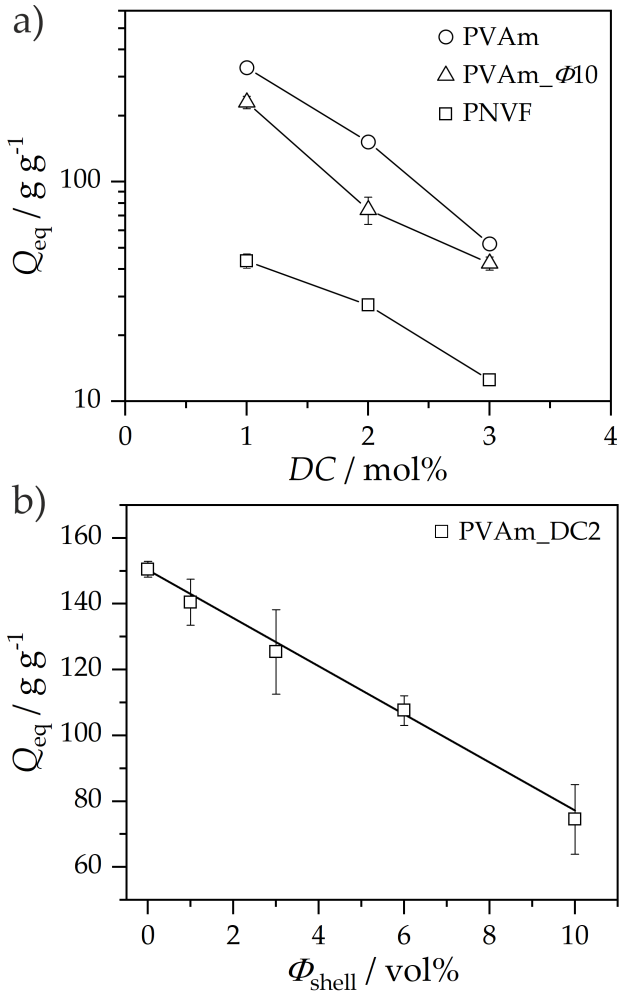

Figure 6.5: a) Equilibrium swelling capacity of neutral PNVF, cationic PVAm, and surface-crosslinked PVAm hydrogels. Solid lines are a guide to the eye. b) Dependency of Q_{eq} on the increasing degree of surface-crosslinking of sample PVAm_DC2. The solid line is a least-squares linear fit yielding $Q_{eq} = -7.3\,\phi_{shell} + 150$ with $R^2 = 0.99$. Figure adapted from [Fen22b].

function of ϕ_{shell} as more elastic chains are introduced at the surface of the particles.

Swelling capacity only provides insights about the average degree of crosslinking and cannot be used to monitor particle topology, such as the core-shell structure. TD NMR can be used to overcome this limitation by providing further molecular insights. Saturation recovery measurements were performed on PNVF and PVAm hydrogels to determine the recycle delay for the T_2 relaxation measurements, as

shown in Figure 6.6. The T_1 relaxation build-up curves were evaluated by the bi-exponential fit

$$\frac{I(\tau)}{I_{\max}(\tau)} = A_{\text{short}} \left(1 - \exp(-\frac{\tau}{T_{1,\text{short}}})\right) + (1 - A_{\text{short}}) \left(1 - \exp(-\frac{\tau}{T_{1,\text{long}}})\right) \tag{6.9}$$

where τ is the recovery delay and T_1 is the longitudinal relaxation time ranging from milliseconds to seconds as denoted by the subscript short and long, respectively. Table 6.2 summarizes the fitting results. Section B.3.1, p. 112 explains the saturation recovery experiment and data acquisition in more detail.

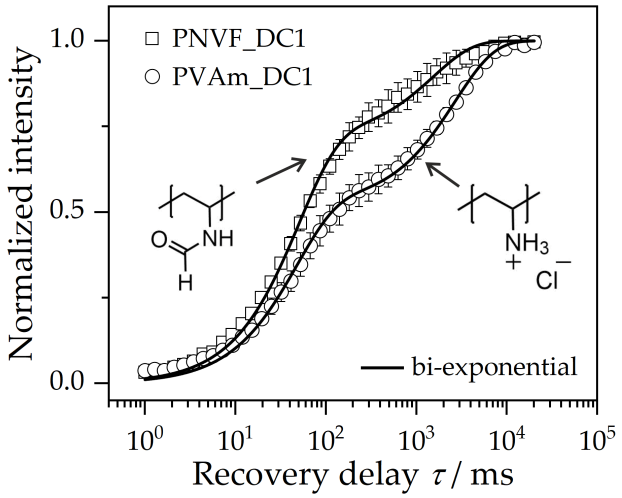

Figure 6.6: Average T_1 magnetization build-up obtained by a saturation experiment for three samples with varying $DC = 1$, 2, and 3 mol% to determine the recycle delay for the T_2 relaxation measurements. Error bars represent one standard deviation. Solid lines are least-squares bi-exponential fits using Equation 6.9. Fitting results are displayed in Table 6.2. Chemical structures refer to PNVF and PVAm where hydrogen atoms that can exchange with deuterium in the D_2O solvent are highlighted in red. Figure adapted from [Fen22b].

The longitudinal magnetization build-up curves have two characteristic components exhibiting T_1 relaxation times in the range $1 - 3$ s and ≈ 50 ms. The latter short component is assigned to the polymer network, which is within the margin of error constant, and therefore, is not influenced by the chemical structure of the backbone when switching from PNVF to PVAm. $T_{1,\text{long}}$ is assigned to highly mobile residual solvent, such as H_2O and HDO, that are mainly formed by the hydrogen deuterium exchange between the D_2O solvent and the

Table 6.2: Fitting results of the longitudinal T_1 magnetization build-up of PNVF and PVAm samples obtained by Equation 6.9.

Sample	A_{short} (%)	$T_{1,\text{short}}$ (ms)	$T_{1,\text{long}}$ (s)
PNVF	71.7 ± 1.1	49.6 ± 1.7	1.5 ± 0.1
PVAm	52.3 ± 0.7	46.4 ± 1.7	2.7 ± 0.1

side groups of the polymer backbone, as highlighted by the chemical structures displayed in Figure 6.6. This exchange is further reflected in the prefactor A_{short} that resembles the polymer network fraction. For PNVF, A_{short} is $\approx 72\,\%$, suggesting a polymer to solvent ratio of roughly 4 : 1. This value is consistent with the chemical structure of PNVF, considering the four hydrogen atoms (i. e., three C-H bonds and one aldehyde bond) along the polymer backbone that cannot undergo a hydrogen deuterium exchange. In contrast, A_{short} in PVAm hydrogels suggests a 1 : 1 ratio due to the formation of an ammonium bond consisting of three hydrogen atoms that exchange with deuterium.

As the low standard deviation suggests, the T_1 magnetization build-up is not influenced by DC. T_1 is sensitive to fast motions, such as intramolecular rotations of side groups, close to the Larmor frequency, as quantified by Equation 3.13, p. 22 of the BPP model. Therefore, weak constraints imposed by chemical crosslinks do not substantially influence T_1 relaxation times. In addition, $T_{1,\text{long}}$ of the solvent increases from 1.5 to 2.7 s switching from PNVF to PVAm, indicating that chemical structure affects water dynamics. Increasing $T_{1,\text{long}}$ suggests higher mobility of the water molecules and a less ordered water structure. Presuming a high chloride concentration in PVAm hydrogels as a result of the acidic hydrolysis of PNVF with HCl, an increase in $T_{1,\text{long}}$ presumably arises from the chaotropic nature of chloride ions that reduce water structure formation by disrupting hydrogen bond formation in analogy to the Hofmeister series [Col97; Hri02; Moe04; Con15; Kou15].

Segmental mobility of the PVAm core-shell particles was studied by ^{1}H transverse relaxation measurements. Section B.3.2, p. 112 explains the used pulse sequence in more detail. Figure 6.7 shows the obtained T_2 relaxation curves and the respective T_2 distributions of PVAm particles with varying degrees of surface-crosslinking obtained by regularized inversion using the MATLAB implemented CONTIN algorithm. The apparent T_2 distributions follow multi-modal lognormal distributions. With increasing ϕ_{shell} the contribution of highly rigid domains with T_2 relaxation times on the order of 100 µs rises. This rigid domains are attributed to increasing shell formation. To quantitatively compare the samples, the geometric mean $GM(T_2)$ and

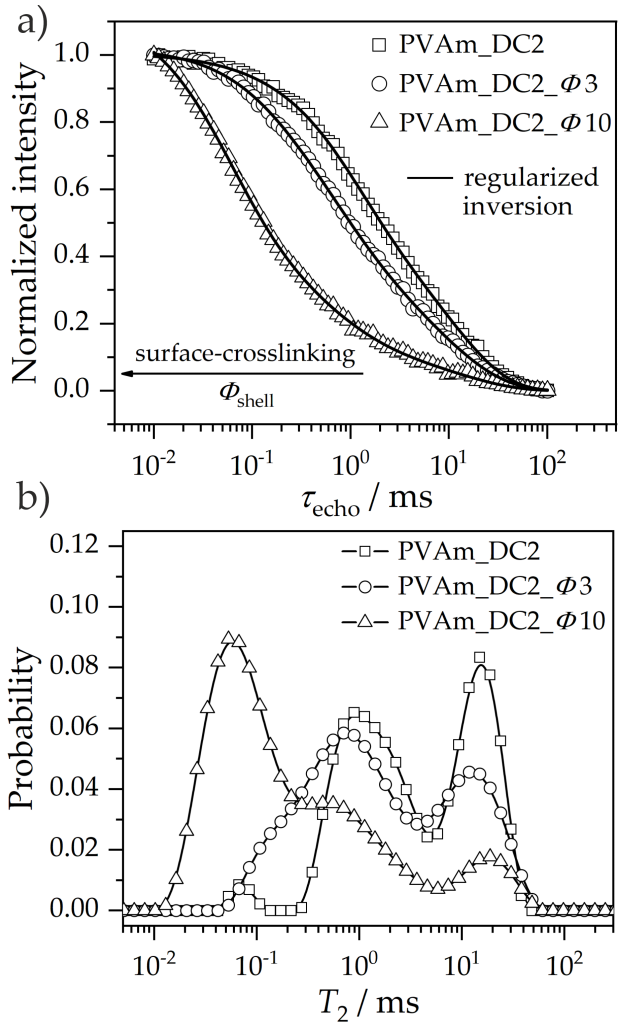

Figure 6.7: a) T_2 relaxation curves of PVAm hydrogels with increasing degree of surface-crosslinking. Solid lines represent the results of the regularized inversion obtained by the MATLAB implemented CONTIN algorithm. b) Corresponding computed T_2 distribution curves. Discrete sum of T_2 probabilities equals 1. Solid lines are a guide to the eye. Figure adapted from [Fen22b].

coefficient of variation $CV(T_2)$ of the distributions was calculated according to Equation 6.7, p. 62 and Equation 6.8, p. 62, respectively.

The calculated $GM(T_2)$ and $CV(T_2)$ are shown as a function of ϕ_{shell} in Figure 6.8. $GM(T_2)$ is indicative for the average degree of crosslinking and decreases gradually from 3.4 ms at $\phi_{\text{shell}} = 0$ vol% to 0.2 ms at $\phi_{\text{shell}} = 10$ vol%. More crosslinks are introduced into the hydrogel at higher ϕ_{shell}. $CV(T_2)$ is used as a measure of network heterogeneity. $CV(T_2)$ increases linearly from 2.7 ms at $\phi_{\text{shell}} = 0$ vol% to 8.1 ms at $\phi_{\text{shell}} = 10$ vol%. This finding implies that the dynamic contrast of the rigid shell and flexible core increases at higher ϕ_{shell},

indicating that the core-shell topology is reflected in the T_2 relaxation time distribution. Since both Q_{eq} and $GM(T_2)$ depend on the average degree of crosslinking in the sample, their correlation should exhibit a characteristic relationship. This relationship could then be used to infer the macroscopic Q_{eq} from the molecular mobility measured by non-invasive NMR techniques.

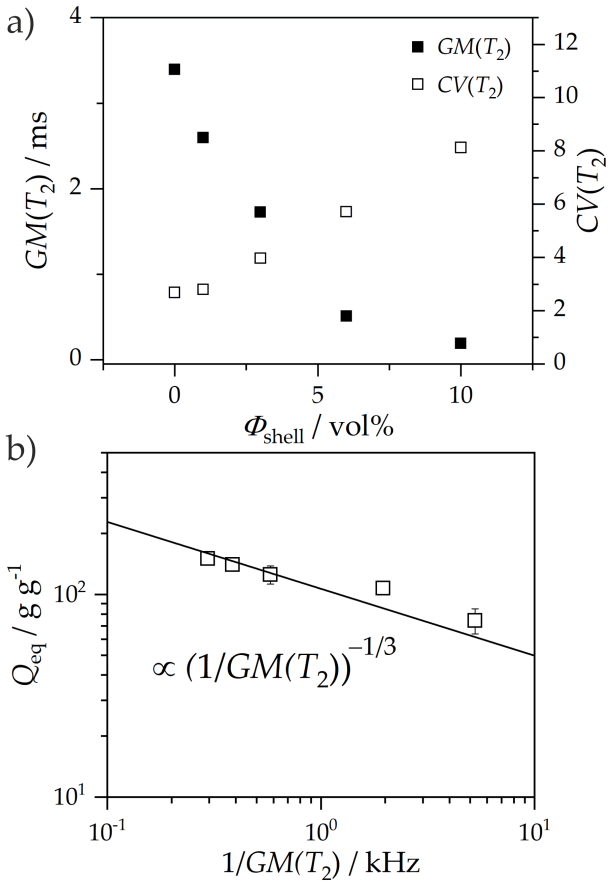

Figure 6.8: a) Geometric mean $GM(T_2)$ and coefficient of variation $CV(T_2)$ of the computed T_2 distributions of PVAm_DC2 core-shell particles. Higher $CV(T_2)$ values as a function of surface-crosslinking indicate an increasing network heterogeneity. b) Equilibrium swelling capacity Q_{eq} as a function of $1/GM(T_2)$ relaxation rate, displayed on a log-log scale. The solid line highlights the thermodynamic prediction of Q_{eq} based on the elastic term of Equation 2.6, p. 14, presuming a direct proportionality between the elastic modulus G' and the $1/T_2$ relaxation rate and that Q_{eq} is the inverse of the polymer volume fraction ν_2.

Figure 6.8 further shows Q_{eq} as a function of $1/GM(T_2)$ relaxation rate. Q_{eq} decreases as a function of $1/GM(T_2)$ according to a characteristic power low decay of the form $Q_{eq} \propto (1/GM(T_2))^{-1/3}$, highlighted by the solid line. This power law is based on the thermodynamic prediction of Q_{eq} (see the elastic osmotic pressure term of Equation 2.6, p. 14), presuming that Q_{eq} is inversely proportional to the polymer volume fraction ν_2. Essentially, SAPs swell until a characteristic concentration is reached where their osmotic pressure is counterbalanced by the elastic modulus [Rub96]. At the equilibrium swelling capacity, the elastic modulus equals the osmotic pressure [Rub96]. Therefore, Equation 2.6, p. 14 gives the relationship

$$G' \propto Q_{eq}^{-1/3} \tag{6.10}$$

between the elastic modulus G' and Q_{eq}. The experimentally obtained relationship $Q_{eq} \propto (1/GM(T_2))^{-1/3}$ implies that the T_2 relaxation rate is directly proportional to G'. An unique approach to further empirically verify this intriguing relationship between molecular mobility of polymer network chains and the macroscopic mechanical properties is subject of the next chapter.

7

RHEO-NMR: CORRELATION OF MOLECULAR DYNAMICS WITH MECHANICAL PROPERTIES DURING GELATION

Abstract Establishing a consistent understanding of mechanical properties and their molecular origins is essential to develop rational design principles of hydrogels. This chapter introduces an advanced rheological method that can simultaneously measure the mechanical response and molecular dynamics of hydrogels. Molecular dynamics is measured by ^{1}H T_2 relaxation measurements using a portable NMR magnet that is integrated into a rheometer. The application of this Rheo-NMR device for monitoring acrylic acid (AAc) gelation kinetics is discussed with a consideration of theoretical predictions of the elastic modulus G' based on the confining tube model of semi-dilute entangled polymer solutions. The Rheo-NMR measurements reveal an inverse relationship between the elastic plateau modulus and T_2 relaxation times. Consequently, macroscopic properties of hydrogels can be inferred from molecular dynamics, advancing the further development of non-invasive and forceless mechanical characterizations using TD NMR techniques.

7.1 TECHNICAL DETAILS OF THE RHEO-NMR DEVICE

Polymer gels are viscoelastic, exhibiting simultaneous liquid- and solid-like behaviors which depend on the time scale and frequency of the applied mechanical deformations. Rheology is a branch of physics that studies flow and deformation of materials in response to mechanical forces governed by the theoretical framework of continuum mechanics [Mac94; Mor01; Dea18]. Hence, polymer gels are ideal candidates for the application of rheological measurements to quantify viscoelasticity and determine application-relevant properties, such as mechanical strength, yield stress, and fracture resistance [Mez20].

From Greek
-rheo 'flow'
-logia 'study of'

Macroscopic rheological measurements, however, only provide averaged mechanical properties of the bulk material and cannot reveal molecular insights, which are essential to fully understand structure-properties relationships. Consequently, great effort has been devoted to advance standard rheometer setups by integrating other molecular characterization techniques, creating the so-called Rheo-X devices, where X typically refers to sub-micrometer characterization techniques, such as small-angle X-ray scattering [Pan03], dielectric spectroscopy

Figure 7.1: DHR-3 rheometer with TD NMR attachment.

[Capo7; Mei12], IR spectroscopy [BA11; Rad21], and TD NMR relaxometry [Rat17; Rän19].

The recently developed combined Rheo-NMR device used in this dissertation consists of a portable low-field ($\omega_L/2\pi = 25$ MHz for ^{1}H) NMR magnet integrated into a DHR-3 rheometer (TA Instruments). Neodymium-iron-boron based permanent magnet positioned in a Halbach array create the magnetic field around the rheometer geometry. Several rheometer geometries are available including plate-plate, cone-plate, vane-in-cup, and bob-in-cup geometries. A Dewar shields the magnets from the sample compartment, allowing a broad temperature control in the range -15 – 210 °C. A Bruker minispec unit (NF series) performs pulsing and data acquisition of the NMR experiments. The NMR probe has a dead time of 10 µs and pulse lengths of 2.2 µs (90°) and 4.4 µs (180°). Figure 7.1 shows a photo of the current portable NMR magnet prototype (2020) integrated into a DHR-3 rheometer and Figure 7.2 shows the technical outline of the NMR probe.

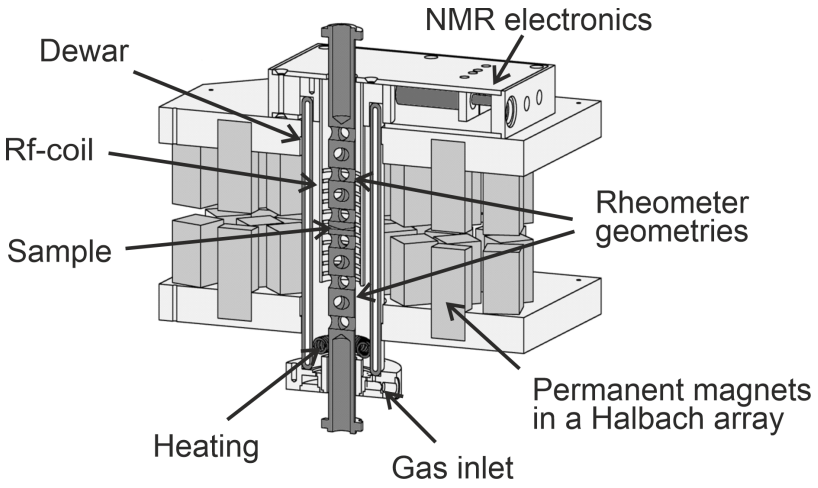

Figure 7.2: Technical outline of the low-field NMR magnet used as rheometer attachment. Reprinted with permission from Ratzsch and coworkers [Rat17]. Copyright 2017, The Society of Rheology.

The Rheo-NMR device has been used to study shear-induced crystallization kinetics of isotactic poly(propylene) (iPP) [Rat17; Rän19]. This semi-crystalline polymer exhibits both crystalline and amorphous domains which exhibit distinct T_2 relaxation times on the order of microseconds and milliseconds, respectively. Consequently, T_2 relaxation curves of iPP follow typically a bi-exponential decay. By considering the relative NMR signal intensity of the crystalline and amorphous domains, the mass crystallinity X_c can be inferred from the measured bi-exponential T_2 relaxation curves. Therefore, Rheo-NMR measurements of i-PP crystallization kinetics enable the online assessment of the crystallization-dependent absolute complex viscosity $|\eta^*(X_c)|$ using oscillatory time sweeps. By converting X_c into a volume fraction

Φ_c using the densities of the crystalline and amorphous domains, the crystallization curves can be evaluated in terms of common viscosity models of solid-particle suspensions, such as the Einstein and Krieger-Dougherty equation [Mew11]. It has been found that $|\eta^*(\Phi_c)|$ correlation plots during crystallization of i-PP can be described by the semi-empirical extended Einstein equation

$$\frac{|\eta^*|}{|\eta^*|_0} = 1 + 2.5\,\phi_{\text{cryst.}} + D\,\phi^c_{\text{cryst.}}\,, \tag{7.1}$$

where $|\eta^*|/|\eta^*|_0$ is the normalized absolute complex viscosity and $\phi_{\text{cryst.}}$ is the volume fraction of crystalline domains. Variables D and c are fitting parameters with D representing the dynamic range of $|\eta^*|/|\eta^*|_0$ over the studied interval. Parameter c is in the range $4-5$ and has been associated with the coordination number of interacting spherulites [Rän19]. The universality of this scaling exponent, however, has yet to be confirmed for a broader range of semi-crystalline polymers.

7.2 ADVANCED MONITORING OF ACRYLIC ACID GELATION

The correlation of swelling capacity with the average T_2 relaxation time of PVAm hydrogels, discussed in the previous TD NMR chapter, implies an inverse relationship between the elastic plateau modulus and T_2 relaxation time. Empirical investigations of this correlation remain a longstanding challenge in hydrogel research due to the inherent experimental design differences between rheological and TD NMR methods. Characteristics of hydrogels, such as the low polymer concentration, the structural complexity, and the intricate gelation process, further distinctly limit a reliable assessment of this correlation. Consequently, current research lacks consistent empirical data regarding the relationship between G' and T_2 relaxation times as well as its time-evolution during gelation, indicating the need for advanced methodologies.

The Rheo-NMR device can measure G' and T_2 simultaneously, and therefore, was used to elucidate the aforementioned research gap. Owing to its availability and high importance in research and industry, the aqueous free radical crosslinking copolymerization of AAc and MBA serves as a model system for the Rheo-NMR experiments [Sco97; Buc98; Ell04; Mag18]. D_2O was used as a solvent to prepare the pre-gel solution with a total monomer concentration of 20 wt%. The molar ratio of MBA to AAc was varied to target DC = 0, 0.05, 0.1, 0.2, 0.5, and 1 mol%. The water-soluble azo initiator VA-044 was used to start the copolymerization at constant 40 °C.

Synthetic parameters

Small amplitude oscillatory time sweeps were performed to study macroscopic gelation kinetics applying a low strain of $\gamma_0 = 0.5\,\%$ and an angular frequency of $\omega = 6.3\ \text{rad}\,\text{s}^{-1}$. A vane-in-cup geom-

Rheological and NMR parameters

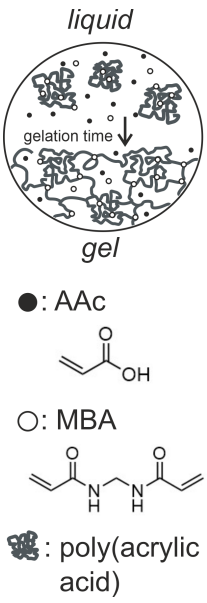

Figure 7.3: Liquid - gel transition during AAc gelation. Figure adapted from [Fen22a].

etry was used to ensure repeatability as wall slips were minimized throughout the gelation of all pre-gel compositions. In addition, the vane-in-cup geometry allows for more sample, increasing thereby the signal-to-noise ratio of the TD NMR experiments. T_2 relaxation curves were recorded by a combination of a MSE and CPMG (Carr, Purcell, Meiboom, Gill) pulse sequence using a XX4 phase cycle to avoid spin locking effects [Mei58; Rhi71; Gul90]. The pulse sequence ends with a recycle delay (RD) of 300 ms, which is > 5 times the T_1 of PAAc hydrogel (see Figure B.3, p. 116 in the appendix). 8 scans were used for signal averaging, which leads to a total experiment time of ≈ 5 s, and therefore, ensures sufficient time resolution for monitoring gelation kinetics. A Bruker VTU unit controlled the temperature to 40 °C using a low air flow rate of 270 $\mathrm{L\,h^{-1}}$. Section B.4, p. 114 provides a detailed explanation of the sample preparation, rheometer settings, and the used pulse sequences.

Liquid-gel transition during the copolymerization started within 15 minutes and exhibits a typical sigmoidal curve in the rheological data. Figure 7.4 illustrates the Rheo-NMR device and summarizes the essential rheological and TD NMR observables.

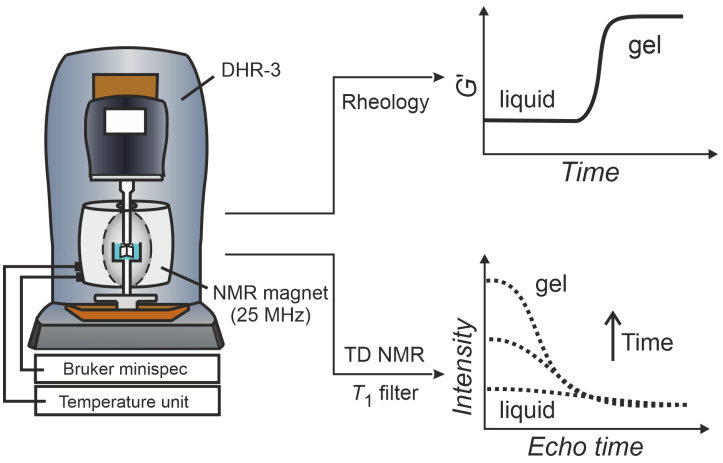

Figure 7.4: Schematics of the Rheo-NMR device and experimental observables. A portable low-field NMR magnet is integrated into a DHR-3 stress-controlled rheometer. The combined setup monitors the liquid - gel transition of the free radical crosslinking copolymerization of AAc and MBA to obtain the direct, in-situ correlation of the elastic modulus G' with the T_2 relaxation time. T_2 relaxation measurements use a low recycle delay of 300 ms as a T_1 filter to suppress signal intensity of highly mobile species, such as HDO and monomer. Figure adapted from [Fen22a].

Gelation kinetics of AAc hydrogels was measured for varying DC values. Figure 7.5 shows the time-evolution of the elastic G' and loss modulus G'' as a function of gelation time exemplary for three

DC values. The pre-gel composition with $DC = 0\,\text{mol\%}$ does not contain MBA, and therefore, is a physical gel where crosslinks are only formed by polymer chain entanglements. The mechanical response

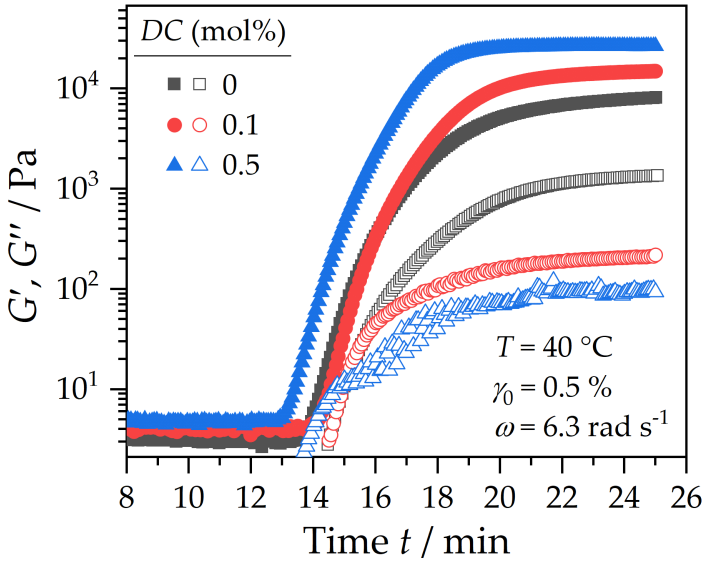

Figure 7.5: Small amplitude oscillatory time sweeps. Elastic G' (solid symbols) and loss modulus G'' (open symbols) of AAc samples with varying *DC* values as a function of gelation time. The sigmoidal mechanical response comprises three characteristic phases, namely an induction period within the first 14 minutes, a rapid increase of the moduli by three orders of magnitude, and an approach to a plateau value. Figure adapted from [Fen22a].

of the gelation follows a sigmoidal curve. After an induction period of $\approx$ 14 minutes, G' increases rapidly by $3-4$ orders of magnitude from approximately 5 Pa to 10 kPa, reaching a plateau value within 5 minutes. The 5 Pa offset in G' during the induction period presumably arises from the intrinsic inertia of the vane geometry, indicating the limit in sensitivity for low viscous solutions of the used experimental Rheo-NMR setup and parameters. The length of the time sweep was kept constant at approximately 25 min to avoid a steady increase of the G' plateau modulus due to water evaporation.

To study the impact of *DC* on gelation kinetics, the gelation curves were normalized to the maximum G' and evaluated by the low parameter fit function

$$G'_{\text{norm}}(t) = \frac{t^n}{t^n + \theta_{\text{rheo}}^n}, \tag{7.2}$$

where θ_{rheo} is the gelation half time with $G'_{\text{norm}}(\theta_{\text{rheo}}) = 0.5$ and n is the gelation rate exponent [Adi16; Mag18]. n is proportional to the slope at $t = \theta_{\text{rheo}}$ according to $\dot{G}'(\theta_{\text{rheo}}) = n/4\theta_{\text{rheo}}$ [Calo4]. Figure 7.6

shows the normalized gelation curves with the fits and the dependency of the maximum elastic modulus G'_{max} and θ_{rheo} on DC.

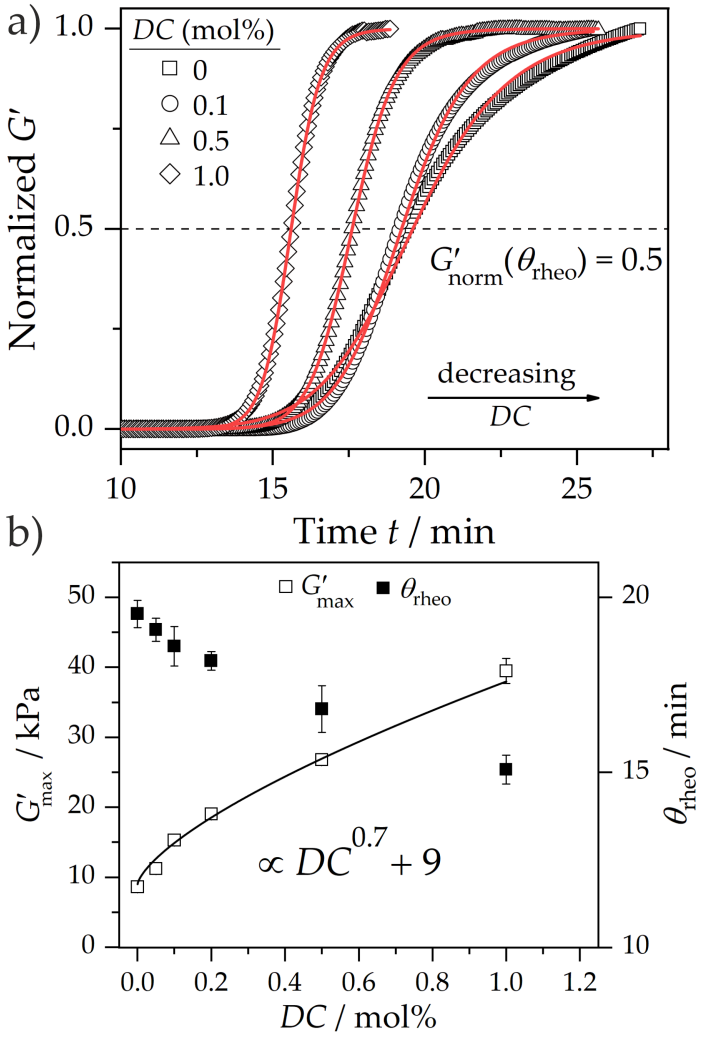

Figure 7.6: Kinetic analysis of normalized rheological gelation curves. a) Time-evolution of normalized G' for varying DC values. Solid lines are least-squares kinetic fits using Equation 7.2. b) Maximum elastic modulus G'_{max} and the gelation half time θ_{rheo} as a function of DC. The solid line is a least-squares power law fit with a scaling exponent of 0.70 ± 0.05, a prefactor of 30 kPa mol%$^{-0.7}$, and an offset of 9 kPa. G'_{max} at $DC = 0$ mol% represents the purely entangled PAAc network. Figure adapted from [Fen22a].

The amount of MBA crosslinker in the pre-gel composition distinctly affects the gelation behavior. θ_{rheo} decreases from 19 min at $DC = 0$ mol% to 15 min $DC = 1$ mol%. G'_{max} increases approximately fourfold from 9 kPa for the purely entangled network up to 39 kPa at $DC = 1$ mol%. Despite the use of low strains, wall slips (not shown) were observed for the highest crosslinked sample with $DC = 1$ mol%

where G' drops by 10 %. This drop was presumably induced by a significant contraction of the bulk material causing the sample to loose contact with the cup geometry. Consequently, data points were cut beyond the wall slips, which does not affect data evaluation as the plateau value had been reached at this point.

The increase of G'_{max} as a function of DC follows a power law with a scaling exponent of 0.70 ± 0.05, suggesting that crosslinking efficiency decreases at higher crosslinker concentrations. This decrease in efficiency agrees with previous studies and has been associated with an increase of topological defects, for instance, due to additional intramolecular cyclization reactions between the propagating polymer chain and pendant vinyl groups from the crosslinker [Adi16].

Figure 7.7 shows the final loss tangent $\tan\delta = G''_{max}/G'_{max}$ and the gelation rate exponent n as a function of DC.

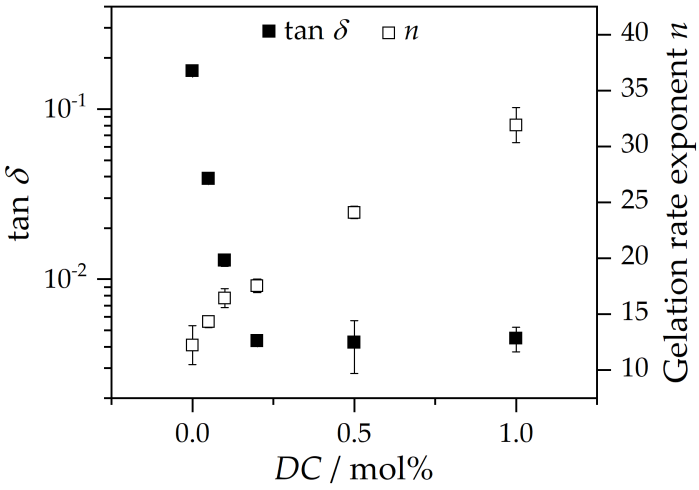

Figure 7.7: Final loss tangent $\tan\delta = G''_{max}/G'_{max}$ and the gelation rate exponent n as a function of DC. $\tan\delta < 1$ implies a predominant elastic response throughout all samples. Figure adapted from [Fen22a].

The $\tan\delta$ measures the ratio of viscous dissipation to elasticity in a material and decreases by two orders of magnitude from 0.2 at $DC = 0$ mol% to 0.004 at $DC = 1$ mol%, reaching a plateau value that indicates the detection limit of G'' in the used Rheo-NMR setup. Higher DC values introduce additional chemical crosslinks into the network, increasing the elastic response. DC further enhances the gelation rate from $n = 12$ to 32. This high value arises from the free radical crosslinking copolymerization and clearly indicates that increasing MBA concentration profoundly facilitates the gelation.

Nanostructural insights into the gelation process were obtained by monitoring T_2 relaxation curves, which can be evaluated in terms of their initial NMR signal intensity and shape. The former is governed by the concentration of polymer network chains whereas the latter

is dictated by the rigidity and heterogeneity of the gelled sample. To quantify the time-evolution of the shape, the T_2 relaxation curves were evaluated by the stretched exponential (Kohlrausch–Williams–Watts) function

$$I(\tau_{\text{echo}}) = A \exp\left(-\left(\frac{\tau_{\text{echo}}}{T_2}\right)^{\beta}\right) + \text{offset}\,, \tag{7.3}$$

where $\beta < 1$ is the stretching exponent and the offset signal intensity from residual solvent was kept constant at 1 %. This low parameter fitting function has been used successfully in previous studies of PAAc hydrogels [Höp14]. The β parameter is inversely proportional to the width of the distribution function [Böh94; Edhoo; Luk19], and therefore, can be associated with the nanoscopic network heterogeneity of the studied sample. Figure 7.8 shows the time-evolution and stretched exponential fits of T_2 relaxation curves during the liquid - gel transition of the sample with $DC = 0.1$ mol%.

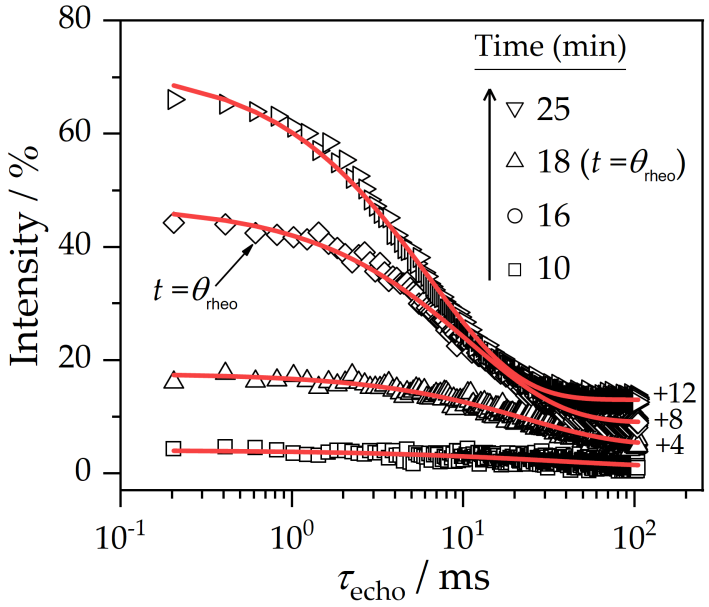

Figure 7.8: Time-evolution and data analysis of T_2 relaxation curves during the gelation of the sample with $DC = 0.1$ mol% obtained by a MSE/CPMG pulse sequence. The sample transitions from the sol state at 10 min to a highly crosslinked gel state at 25 min. Solid lines are least squares stretched exponential fits according to Equation 7.3. Curves were shifted upwards in steps of 4 % for better visibility. Figure adapted from [Fen22a].

The initial NMR signal intensity during the induction period is low at 6 %. At the beginning of the experiment, the sample mainly contains highly mobile species, such as unreacted monomer, oligomers, and

HDO solvent, in the liquid state. Their T_1 relaxation time is on the order of seconds, and therefore, the RD of 300 ms functions as a T_1 filter for solvent suppression. The signal intensity increases gradually by a factor of 10, analogue to the rapid increase of G', when network chains with T_1 relaxation times on the order of the RD are formed.

Figure 7.9 shows the direct correlation of G' with T_2 relaxation times during the gelation of samples with varying DC.

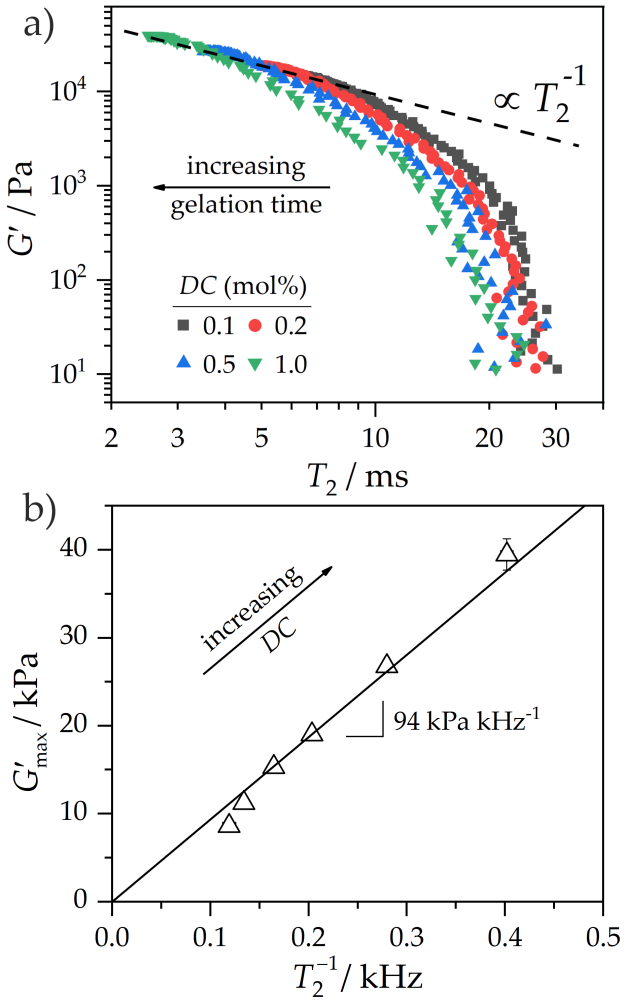

Figure 7.9: a) Correlation plot of the elastic modulus G' against T_2 relaxation times during the gelation of AAc samples with varying DC values, displayed on a log-log scale. Dashed line highlights an inverse relationship between G' and T_2. Figure adapted from [Fen22a]. b) Elastic plateau modulus G'_{max} as a function of T_2 relaxation rate. The solid line is a least-squares linear fit with zero intercept given by $G'_{max} = 94T_2^{-1}$, indicating an inverse relationship between G'_{max} and T_2 relaxation times.

The dependency of G' on T_2 relaxation times has a characteristic curve behavior for every sample. At early gelation times with $G' <$

1 kPa, T_2 is constant approximately in the range $20 - 30$ ms. This finding implies that the polymer network at this point consists mainly out of highly mobile PAAc chains that dominate the relaxation process. At $G' > 1$ kPa topological constraints from chemical crosslinks and polymer chain entanglements start to dominate the relaxation process, which shifts T_2 relaxation times to lower values close to 3 ms at $DC = 1$ mol%. Higher crosslinking densities restrict the mobility of polymer chains between crosslinks, and therefore, enhance dipolar couplings. All samples ultimately approach an inverse relationship between G' and T_2 relaxation times. This finding confirms that the macroscopic elasticity is similarly reflected in the molecular mobility of polymer chains as both are a function of the average polymer chain length between crosslinks. Hence, it further supports theoretical statistical treatments of the relationship between T_2 relaxation times and crosslinking density in gels, presuming that the T_2 relaxation time reflects the conformational mean position of polymer chain segments between crosslinks [CA93]. Moreover, this finding empirically verifies the assumption made in the previous chapter that the equilibrium swelling capacity can be directly inferred from T_2 relaxation times.

Figure 7.9 further shows a horizontal shift of T_2 relaxation times towards lower values at early gelation times as a function of increasing DC. This early increase in molecular stiffness at the same G' suggests the formation of rigid, non-elastic network defects, such as crosslinking clusters, presumably caused by the high concentration of MBA crosslinker, which enhances intramolecular crosslinking reactions. The formation of network defects should lead to higher network heterogeneity at increasing DC, and therefore, be quantifiable by the β stretching parameter. To investigate the influence of DC on network heterogeneity, T_2 relaxation times and β at constant $G' = 1$ kPa were plotted against DC, as shown in Figure 7.10.

The T_2 relaxation curve of a purely entangled network with $DC = 0$ mol% exhibits a mono-exponential decay with one characteristic T_2 relaxation time (i. e., $\beta = 1$). The β parameter decreases up to 0.83 with increasing DC, as highlighted by the linear regression analysis in Figure 7.10. β is a measure of network heterogeneity, since it reflects the superposition of dynamically different topologies with distinct T_2 relaxation times [Saa12; Höp14]. Despite the substantial impact of DC on gelation rate and G', DC only marginally affects network heterogeneity in the chosen range of crosslinker concentrations. Future work could assess the relationship between network heterogeneity and mechanical strength, for instance, by studying different crosslinker types and functionalities, such as trimethylolpropane triacrylate (see Figure 7.11 for chemical structure), to advance our understanding of defect formation in free radical polymerized hydrogels.

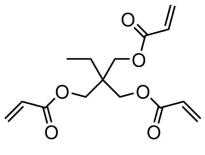

Figure 7.11: Chemical structure of trimethylolpropane triacrylate.

The NMR signal intensity is intrinsically proportional to the number of ^{1}H nuclear spins, and therefore, its time-evolution can be used

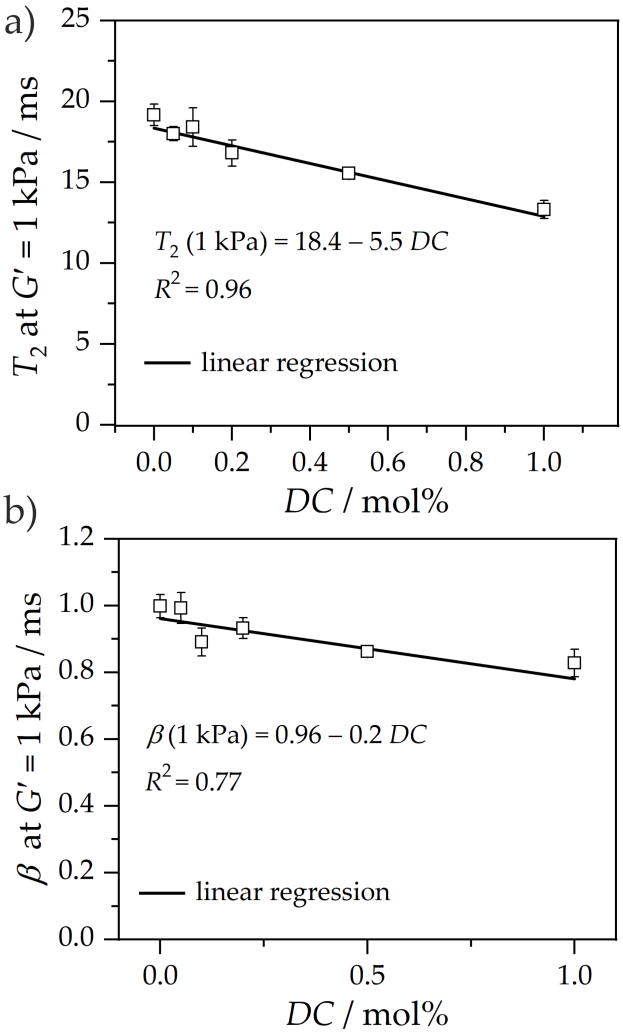

Figure 7.10: T_2 relaxation times (a) and stretching exponent β (b) at constant $G' = 1$ kPa as a function of DC. Solid lines present the result of a linear regression analysis. Both the slight decrease of β and T_2 suggests the formation of rigid non-elastic defects, such as crosslinking clusters, that increase nanoscopic network heterogeneity.

to monitor the polymer concentration during gelation. The applied RD = 300 ms functions as a T_1 filter for solvent suppression and ensures that the NMR signal intensity is highly sensitive towards polymer chains with T_1 relaxation times on the order of milliseconds. Figure B.3, p. 116 shows a saturation recovery experiment of a fully gelled PAAc sample, which exhibits a bi-exponential T_1 build-up curve with characteristic T_1 relaxation times of 35 ms and 3 s of the polymer and solvent, respectively. Consequently, a RD of 300 ms suppresses solvent signal to $1 - \exp(-300/3000) \approx 10\,\%$.

Figure 7.12 shows exemplary the time-evolution of the NMR signal intensity during the gelation of sample with $DC = 1$ mol%. Analogue

to the rheological measurements, NMR signal intensity follows a sigmoidal curve, which was evaluated by the equation

$$I(t) = \frac{(I_{\text{max}} - I_{\text{solv}})t^m}{t^m + \theta_{\text{NMR}}^m} + I_{\text{solv}}\,, \tag{7.4}$$

where I_{max} is a constant representing the maximum NMR signal intensity, I_{solv} is the residual solvent signal, m is the NMR gelation rate exponent, and θ_{NMR} is the NMR gelation halftime.

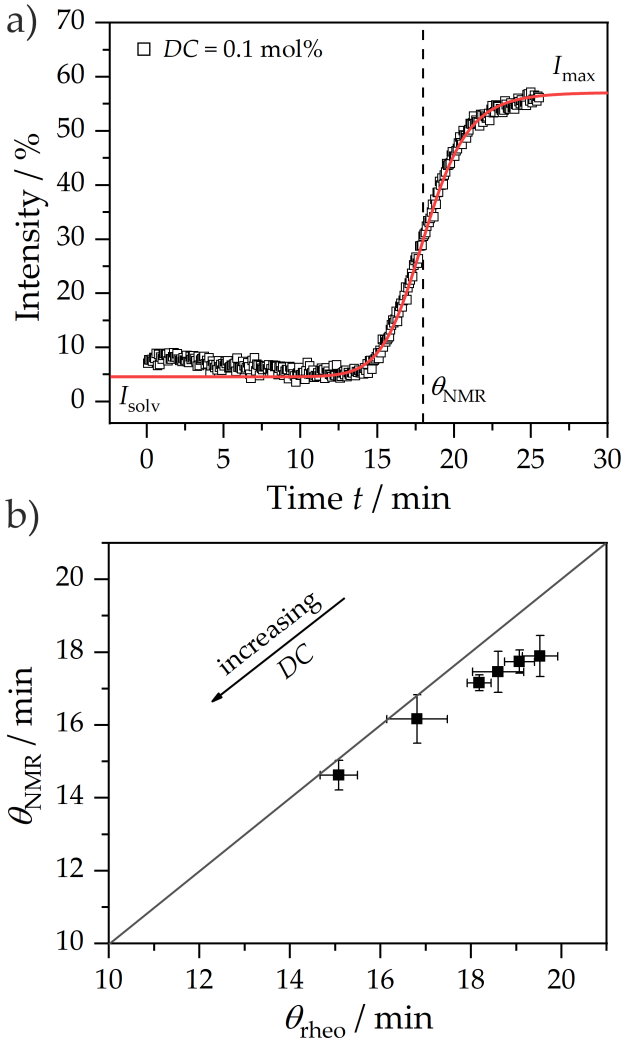

Figure 7.12: a) Time-evolution and kinetic analysis of NMR signal intensity during the gelation of the sample with $DC = 0.1$ mol%. The solid line is a least-squares kinetic fit in the range $10 - 25$ min using Equation 7.4 to quantify residual solvent signal I_{solv} and the NMR gelation half time θ_{NMR}. Figure adapted from [Fen22a]. b) Correlation of the NMR gelation half time θ_{NMR} and rheological gelation half time θ_{rheo}.

Note that during the first 10 min the NMR signal intensity of the raw data drops gradually from 10 % to 6 %. This decrease was attributed to the consumption of triplet oxygen, a paramagnetic radical that shifts T_1 relaxation times of the environment to lower values [Lau87], by the formed initiator radicals. To test this hypothesis, a sample with the same pre-gel composition was degassed with three freeze-pump-thaw cycles. This degassed sample does not exhibits an initial decay of the NMR signal intensity (see Figure B.3 p. 116), supporting the aforementioned assumption.

Figure 7.12 further correlates the NMR gelation half time θ_{NMR} to the rheological gelation half time θ_{rheo}. The kinetic analysis of both rheological and NMR measurements reveals in the margins of error similar gelation half times. For low DC values, θ_{NMR} precedes θ_{rheo} by a minute, suggesting that upon full polymerization other non-covalent interactions, such as the subsequent formation of hydrogen bonds, contribute to an further increase of the mechanical strength. Hydrogen bond formation in hydrogels can last up to several minutes and does not influence the NMR signal intensity [Cui12]. The contribution of these non-covalent interactions to the maximum elastic modulus vanishes at high DC, and therefore, both gelation half times approach the similar value. However, considering the margins of error, the deviation between θ_{NMR} and θ_{rheo} is small and experimental artifacts cannot be fully excluded. Future work could investigate this hypothesis by testing other monomer structures that do not form hydrogen bonds, such as methyl acrylate.

To separate the contribution of solvent signal from the NMR gelation curves, I_{solv} was subtracted from the raw data, which was subsequently normalized to the maximum value yielding the normalized polymer signal intensity

$$I_{\mathrm{poly}}(t) = \frac{I(t) - I_{\mathrm{solv}}}{I_{\mathrm{max}} - I_{\mathrm{solv}}}\,. \tag{7.5}$$

Figure 7.13 shows the correlation of G' with I_{poly} for all pre-gel compositions. The correlation follows a characteristic power law of the form

$$I_{\mathrm{poly}} = G'_{\mathrm{max}}\, I_{\mathrm{poly}}^{2.3}\,. \tag{7.6}$$

Since I_{poly} is sensitive to the polymer concentration, this scaling can be interpret in terms of the confining tube model of semi-dilute entangled polymer solutions. According to this model, the polymer concentration c_{poly} dependency of G' is governed by the Edwards tube diameter a and the correlation length ξ [Gen76; Rub03; Col10]. Both variables resemble two characteristic length scale where ξ describes the distance to neighboring polymer chains (i. e., mesh-size). Figure 7.14 illustrates the confining tube in a semi-dilute entangled polymer solution.

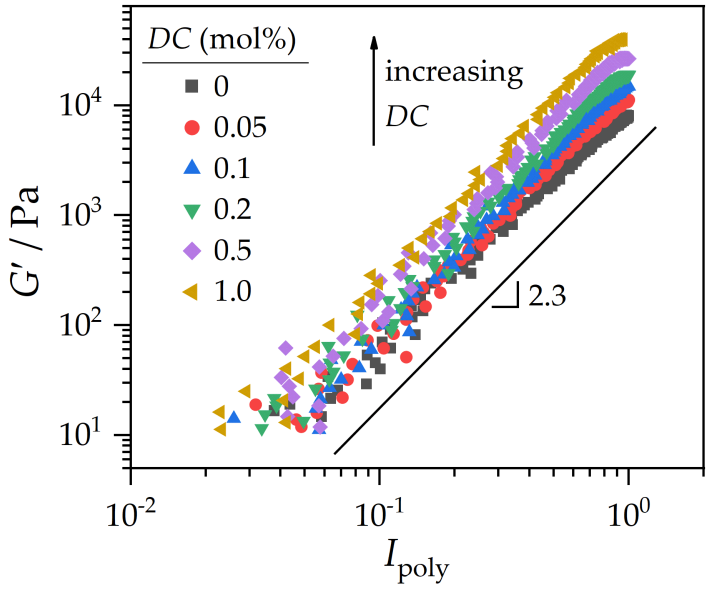

Figure 7.13: Elastic modulus G' as a function of the normalized polymer NMR signal intensity I_{poly} obtained by Equation 7.5, displayed on a log-log scale. The solid line highlights the power law $G' = G'_{\text{max}} I_{\text{poly}}^{2.3}$. The scaling exponent 2.3 represents the dependency of G' on the polymer concentration based on the confining tube model of semi-dilute entangled polymer solutions [Col10]. Figure adapted from [Fen22a].

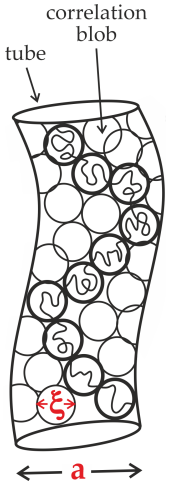

Figure 7.14: The confining tube of a polymer chain in a semi-dilute entangled polymer solutions. Figure adapted from [Fen22a].

According to the rubber-elasticity theory [Fer80], G' is equal to the number density of elastic strands times the thermal energy kT. In semi-dilute entangled polymer solutions, the entanglement volume can be expressed by ξ and a, which scale with the polymer concentration. The polymer concentration dependency of G' is given by

$$G' = \frac{kT}{a^2 \xi} \propto c_{\text{poly}}^{\text{b}}, \tag{7.7}$$

where b is 2.33 in a theta-solvent and 2.31 in a good solvent [Col10]. The empirically obtained scaling of 2.3 agrees with the theoretical predictions and is in the margin of error independent of DC, suggesting that the gelation process is governed by entanglements with DC the offset that determines the elastic plateau modulus.

The Rheo-NMR findings of AAc gelation can be concluded in terms of the semi-empirical function

$$\begin{aligned} G'(DC, t) &= G'_{\text{max}} \, I_{\text{poly}}^{2.3} \\ &= \left(30 DC^{\,0.07} + 9\right) \left(\frac{t^m}{t^m + \theta_{\text{NMR}}^m}\right)^{2.3} \end{aligned} \tag{7.8}$$

considering both the dependency on the synthetic parameters DC (mol%) and on the gelation kinetic parameter I_{poly} (dimensionless)

obtained by NMR. The former captures the influence of the crosslinker concentration on the plateau modulus G'_{max}. The latter describes the time-evolution of G' during gelation based on the kinetic analysis of TD NMR experiments. This relationship advances the development of a unique non-invasive and forceless monitoring of polymer gelation where the elastic modulus can be inferred from the time-evolution of the NMR signal intensity. This may be particuarly useful for soft matter research that studies mechanically weak and sensitive materials, such as in tissue engineering.

8

SEAWATER APPLICATIONS OF CATIONIC HYDROGELS

Abstract This chapter discusses unique seawater applications of the synthesized PAM hydrogels in the fields of water treatment and sustainable energy recovery. A SAP based membrane-free desalination process is described with a theoretical consideration of the Gibbs-Donnan equilibrium. The estimation of the desalination energy demand from the numerical integration of pressure-volume curves is explained. A mechanochemical approach to harness mechanical energy from swelling-shrinking cycles of SAPs induced by salinity gradients is introduced. The principal factors dictating the power output of this osmotic engine are explored.

8.1 MEMBRANE-FREE DESALINATION OF SEAWATER

It has been estimated that 80 % of the global population is exposed to major threats to water security, particularly in areas with rapid population growth and low access to fresh water reservoirs [Vör10]. The fresh water share of global water sources stands at 0.5 % [Kuc14]. Consequently, the implementation of cost-efficient desalination techniques is inevitable to overcome water scarcity. Approximately 16,000 desalination plants operate worldwide, leading to a total desalination capacity of 95 million cubic meters per day [Jon19]. While thermal desalination processes, such as multi-stage flash distillation (MSF), were mainly used in the 20th century, membrane-based desalination techniques are currently predominantly used with the reverse osmosis (RO) process currently accounting for 69 % of the total global desalination capacity [Jon19].

Global desalination capacity is at 95 million cubic meters per day.

The RO process uses semipermeable membranes that reject $> 99\,\%$ of salts dissolved in seawater to obtain pure water [Eli11]. Water molecules of the saline feed solution are pushed through the dense membranes by applying an external pressure of up to 100 bar, which leads to an estimated energy demand for the desalination in the range $3 - 6$ kWh m^{-3}. The theoretical limit is approximately 0.8 kWh m^{-3} based on the osmotic pressure of seawater [Wad01]. Disadvantages of the RO process are the high investment costs of the membranes and their regular maintenance due to clogging and biofouling, which account for 15 % of the total cost per cubic meter [Avl02; Avl03].

Recently, an alternative desalination approach has been proposed that uses commonly available SAPs as a rather cheap material

($1 - 3$ € kg^{-1}) to overcome the membrane related costs of the RO process [Höp10; Höp13; Are19a]. The underlying physical principle of the separation is the Gibbs–Donnan equilibrium, which describes the distribution of mobile salt ions between the SAP gel phase and surrounding solution (see Figure 1.1, p. 3).

The swollen SAP functions as a semipermeable membrane. The crosslinked polyelectrolyte network is spatially fixed and forms the gel phase whereas salt ions, such as Na^+ and Cl^-, can move freely between the surrounding solution and the gel phase. The high concentration of counter ions of the polyelectrolyte chain cause a distinct asymmetric distribution of salt ions between the gel phase and the surrounding solution. Since permeant ions always enter the gel phase on average as ion pairs to ensure electroneutrality, the high concentration of the counterions reduce the concentration gradient of permeant ions towards the gel phase. As a result, the concentration of mobile salt ions is always less in the gel phase compared to the surrounding solution.

A three-step discontinuous process forms the basis of the desalination approach, as shown in Figure 8.1. First, dry SAP particles are swollen in the saline solution, which is subsequently salt enriched due to the Gibbs-Donnan equilibrium induced salt rejection. The concentration of mobile ions inside the swollen particles is less than the initial saline solution. The salt enriched supernatant phase is then discarded and salt depleted water is recovered by deswelling the swollen SAP particles with an external mechanical force. The deswollen particles can be reused in a new cycle by adding saline feed water to reswell the SAP particles.

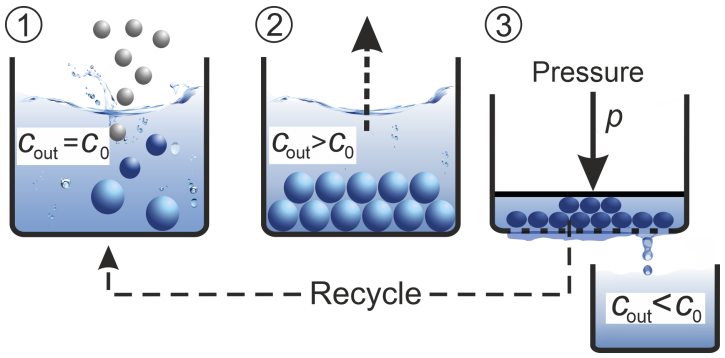

Figure 8.1: Discontinuous three-step desalination process using SAP particles as separation medium. 1) Dry SAP particles are swollen in a saline solution until the equilibrium state. 2) The salt enriched supernatant phase is discarded. 3) Salt depleted water is recovered by applying an external mechanical force to deswell the swollen particles. Figure adapted from [Fen20].

Previous desalination approaches have used PSA based hydrogels to desalinate a 35 $g\,L^{-1}$ (0.171 $mol\,L^{-1}$) sodium chloride NaCl solution that mimics the ionic strength of seawater. The energy demand has been estimated to 8.9 $kWh\,m^{-3}$. However, as concluded in Chapter 5, p. 50, PSA does not swell sufficiently in seawater due to the interaction of the anionic polymer backbone with cationic multivalent ions, such as Mg^{2+} and Ca^{2+}.

Consequently, PSA hydrogels cannot be used for the desalination of seawater. In contrast, the swelling of the synthesized cationic PAM particles is not affected by the seawater composition, and therefore, PAM hydrogels are suitable candidates for the desalination of seawater. Swelling of hydrogels can be treated as a two-phase systems consisting of a gel phase formed by the polymer network and a solution phase. Mobile species, such as water molecules and ions, can move freely across the phase boundary. Considering an equal volume of the gel and solution phase, the concentration of mobile monovalent salt ions in the gel phase is given by

Basics of the mean - field Donnan model

$$c_{in} = \left(\left(\frac{f_{eff}\, c_p}{2} \right)^2 + c_{out}^2 \right)^{1/2} - \frac{f_{eff}\, c_p}{2}\,, \tag{8.1}$$

where c_p is the concentration of charged monomer units and $c_{out} = 2c_0 - c_{in}$ is the salt concentration of the supernatant phase [Are19a]. f_{eff} is in the range $0-1$ and represents the effective charge fraction. The concentration of charged monomer units c_p is related to Q_{eq} by

$$\begin{aligned} c_p = \frac{\chi_p \rho_s}{M_p} &= \frac{\rho_s}{M_p} \times \left(\frac{1}{1+Q_{eq}} \right) \\ &\approx \frac{\rho_s}{M_p Q_{eq}} \qquad \left(Q_{eq} \gg 1 \right)\,, \end{aligned} \tag{8.2}$$

where M_p is the molecular weight of the monomer unit, ρ_s is the density of the solution ($\approx 1000\ g\,L^{-1}$ for water), and χ_p is the polymer mass fraction of the swollen gel, which is related to Q_{eq} [Are19a].

Salt rejection SR measurements can be used as an initial approximation of the SAP based desalination capabilities. This measurement corresponds to the first and second step of the discontinuous desalination process (see Figure 8.1) and studies the salt concentration of the salt enriched supernatant phase. The SR is given relative to the salt concentration of the initial solution c_0 by

$$SR = \frac{c_{out} - c_0}{c_0} \times 100\,\%\,, \tag{8.3}$$

where c_{out} is the concentration of the supernatant phase, which is assumed to be an infinite bath. Dry PAM particles were swollen in 1 wt% NaCl solution, which enables rather simple assessment of the salt

concentration with conductivity measurements. Section B.5.1, p. 117 explains the SR measurements in more detail. Plugging Equation 8.1 in Equation 8.3 yields the theoretical Donnan based salt rejection

$$SR_{\mathrm{D}} = \left(1 - \frac{2c_0}{0.5 f_{\mathrm{eff}} \left(\rho_{\mathrm{s}} / M_{\mathrm{p}} Q_{\mathrm{eq}}\right) + 2c_0}\right) \times 100\,\%\,. \qquad (8.4)$$

Figure 8.2 shows SR as a function of the equilibrium swelling capacity Q_{eq} for the synthesized cationic PAM hydrogel particles.

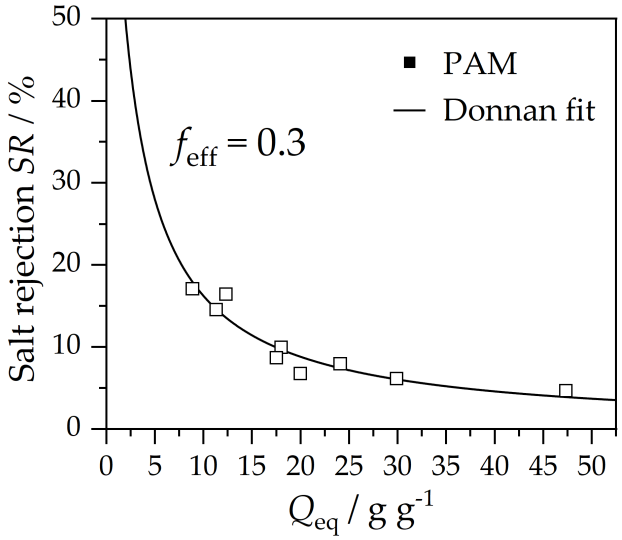

Figure 8.2: Salt rejection of PAM particles in 1 wt% NaCl solution as a function of equilibrium swelling capacity Q_{eq}. The solid line represents a least-squares fit using Equation 8.4 based on the mean-field Donnan theory. The fitting parameter $f_{\mathrm{eff}} = 0.3$ resembles the experimentally determined effective fraction of the charge density within the gel phase. Figure adapted from [Fen20].

SR decreases from 17 % at $Q_{\mathrm{eq}} = 9$ to 4.7 % at $Q_{\mathrm{eq}} = 47$. Increasing Q_{eq} values inherently decrease charge density, and therefore, less SR was observed. The experimentally obtained SR values are further compared to the theoretical SR_D where the free parameter f_{eff} is a measure of the deviation from the theoretical prediction. For PAM hydrogels, a f_{eff} of 0.3 was found, indicating that SR_{D} overpredicts the experimental values. The rather simple derivation of SR_{D} has several limitations. The Donnan theory does not take into account Manning condensation that can limit the effective charge density. When the distance between neighboring charged monomer units are below the Bjerrum length ($\lambda_{\mathrm{B}} = 0.7$ nm in water) [Man69], the electrostatic interactions are on the order of kT. At this critical threshold counterions start to condense along the charged polymer backbone, reducing thereby the effective charge density. The distance between cationic quaternary ammonium

groups of the synthesized PAM hydrogel should be always theoretically larger than λ_B as they are separated by six chemical bonds from the polymer backbone. Yet, the Manning theory considers only an idealized, uniformly charged thread of zero radius without taking into account any molecular properties of the PAM polymer chain, such as the stiffness and restricted rotation of amide bonds. Chemical crosslinks in the hydrogel network presumably further contribute to the deviation, which is particularly dominant at low Q_{eq} with high charge densities.

Sample PAM_DC5_DI25 has the highest $SR = 17\,\%$, and therefore, was chosen for a full desalination cycle of seawater using a custom-build hydraulic press setup. The apparatus has a 400 mL press chamber. A piston is lowered continuously to transfer pressure and compress the swollen hydrogel particles. Two sieves with $3 - 5$ µm wide pore sizes on the bottom and top of the chamber prevent leaking. A distance and pressure sensor monitor the compression of the swollen particles while the outflow is collected in 10 mL fractions. Figure 8.3 illustrates the hydraulic press setup and the molecular structure of the SAP separation medium. Figure 8.4 shows a photo of the press setup. Section B.5.2, p. 117 explains the technical details and experimental parameters of the desalination in more detail.

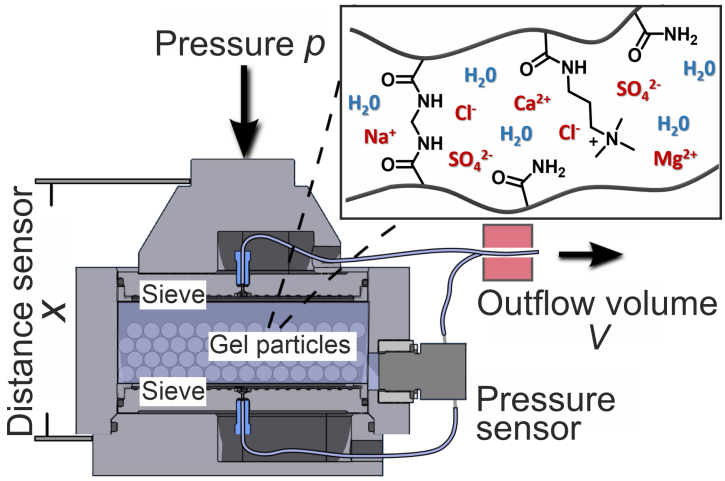

Figure 8.3: Schematic of the hydraulic press setup for the desalination of seawater using cationic PAM hydrogels as a separation medium. Salt depleted water is recovered by deswelling the particles with an external mechanical force. Distance of the piston x, pressure p, and outflow volume V were monitored with an uncertainty ± 1 µm, ± 0.01 bar, and ± 0.5 mL, respectively. The ion content of the seawater was measured offline by inductively coupled plasma optical emission spectroscopy (ICP-OES) and ion chromatography. Figure adapted from [Fen20].

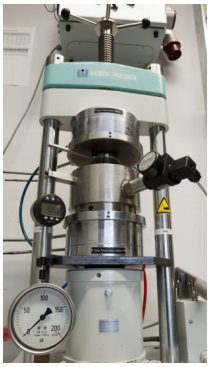

Figure 8.4: Photo of the hydraulic press setup. Figure adapted from [Fen20].

Artificial seawater (see Section B.1, p. 111 for the composition) with a total salt ion concentration of 11.6 g L^{-1} (0.171 mol L^{-1}) serves as the model solution for a proof of concept of the desalination. This molar concentration corresponds to a 1 wt% NaCl solution and was chosen based on two factors. It is in the detectable region of ICP-OES measurements used to quantify the salt ion concentration and is roughly the logarithmic mean of the range of interest (0.1 – 4.3 wt%). Figure 8.5 shows the results of the desalination experiment. The seawater concentration and pressure inside the chamber are shown as a function of the collected outflow volume. The hydrogel compression starts at pressures above 1 bar.

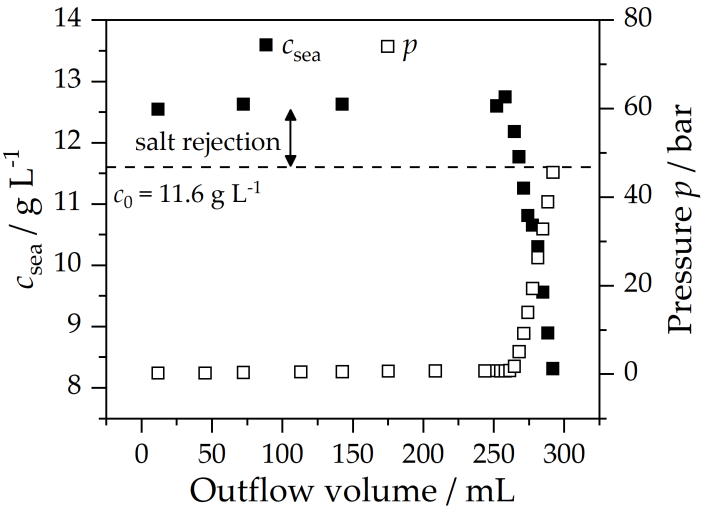

Figure 8.5: Desalination of artificial seawater with initial salt concentration $c_0 = 11.6\,\mathrm{g\,L^{-1}}$ (0.171 mol L^{-1}), highlighted by the dashed line. Sample PAM_DC5_DI25 was used as separation medium. Low pressure was applied to remove the supernatant phase until approximately an outflow volume of 270 mL. Subsequently, the pressure was increased linearly with a rate of 1 bar min^{-1} to compress the swollen hydrogel. The outflow was collected in 3 – 10 mL fractions. Figure adapted from [Fen20].

The continuous compression of the swollen SAP particles releases saline water with decreasing salt concentration. c_{sea} decreases with a slope $\mathrm{d}c_{sea}/\mathrm{d}V = -130\,\mathrm{g\,L^{-2}}$. The last collected fraction at $V =$ 280 mL contained 3 mL saline solution with a salt concentration of 8.3 g L^{-1}, resembling a $\approx 30\,\%$ reduction of the initial salt concentration.

The energy demand of the desalination can be estimated by the numerical integration of the pressure-volume curve according to

$$E = -\int_{i=0}^{n} p_i \,\mathrm{d}V_i\,, \tag{8.5}$$

where V_i is the volume of fraction i [Are17a]. Subtracting the mass of salt inside the fractions $m_{\text{salt},i}$ from the initial mass of salt $m_{\text{salt},0}$, yields the removed salt mass

$$\Delta m_{\text{salt}} = m_{\text{salt},0} - m_{\text{salt},i} = c_0 \sum_i V_i - \sum_i c_i V_i \,, \tag{8.6}$$

where c_i is the salt concentration ($\mathrm{g\,L^{-1}}$) of fraction i. The ratio of the expended energy E to Δm_{salt} defines the energy efficiency parameter ($\mathrm{kWs\,g^{-1}}$)

$$\kappa = \frac{E}{\Delta m_{\text{salt}}} \,, \tag{8.7}$$

which has been used as a criterion for the desalination efficiency [Are17a]. The specific energy $E_{\mathrm{m^3}}$ ($\mathrm{kWh\,m^{-3}}$) for the removal of 35 kg salt in one cubic meter seawater is given by

$$E_{\mathrm{m^3}} = \frac{35000\ \mathrm{g}}{3600\ \mathrm{s\,h^{-1}}} \kappa \approx 10\kappa. \tag{8.8}$$

Using this relation, the specific energy of seawater desalination with cationic PAM hydrogels was estimated to $E_{\mathrm{m^3}} = 17.6\ \mathrm{kWh\,m^{-3}}$, which is similar to previous salt water desalination attempts with PSA based SAPs [Are19a].

Figure 8.6 shows the relative salt ion concentration $c_{\text{rel}} = c_{\text{out}}/c_{\text{sea},0}$ for as a function of outflow volume. $c_{\text{sea},0}$ is the initial concentration of the salt ion. Chloride ions are stronger rejected prior to the deswelling process by the cationic PAM network compared to divalent sulfate ions. Chloride ions are the counterions of the synthesized PAM hydrogels. Consequently, the concentration of chloride is high in the polymer network, reducing the concentration difference between seawater and polymer network. Moreover, two chloride ions are exchanged with divalent sulfate ions that diffuse into the polymer network, which further increases SR of chloride ions. In contrast, cations show no SR and distribute evenly between the supernatant and gel phase. However, this does not lead to a contraction of the network compared to PSA. Quaternary ammonium based hydrogels are therefore essential to enable seawater desalination.

Limitations

Using the press setup and highly crosslinked cationic PAM hydrogels, approximately 3 mL salt depleted seawater with a 30 % reduced concentration was recovered over 1 h applying pressures up to 50 bar. The energy demand was inferred from the pressure-volume curve yielding $E_{\mathrm{m^3}} = 17.6\ \mathrm{kWh\,m^{-3}}$. This estimation has clear limitations as general experimental parameters, such as the energy demand of the press, were neglected. Considering, the significant number of cycles required to obtain one liter of potable drinking water with a concentration $< 0.1\ \mathrm{g\,L^{-1}}$, this desalination approach is not practical compared to other portable desalination devices. Moreover, the discontinuous press setup prevents a reasonable scaling up of this approach.

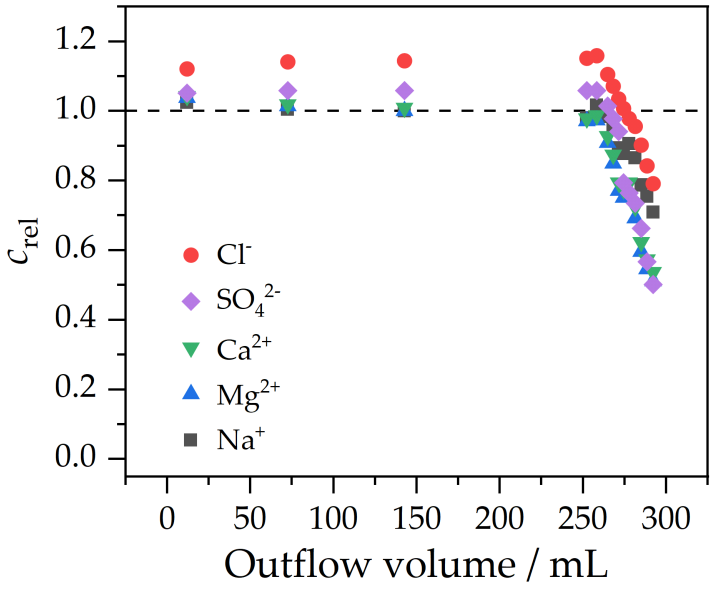

Figure 8.6: Salt partitioning of salt ions during seawater desalination. Cl^- is the counterion of the PAM_DC5_DI25 sample and exhibits the strongest salt rejection. When divalent SO_4^{-2} ions diffuse into the gel phase two Cl^- ions are exchanged, enhancing thereby the SR. Figure adapted from [Fen20].

However, currently 20 billion pieces of used diapers are disposed in landfills, leading to more than 3.5 millions tonnes of diaper waste that take at least 500 years to decompose [Kho19]. Consequently, researching potential reuse of SAP waste in addition to simple incineration is of great interest to improve their environmental performance. The desalination efficiency with SAPs decreases as a function of salt concentration [Are17a]. Therefore, the most feasible application of the SAP desalination is the water treatment of brackish water. PSA based SAPs from diaper waste can be directly reused, reducing the synthetic demand and high cost of cationic hydrogels. Moreover, as a polychelat, PSA can simultaneously function as a rather simple adsorbent for toxic heavy metals present in the brackish water [Roy11]. Future work can further assess other continuous experimental designs, such as a roll-to-roll setup where a sheet of SAP is in alternating fashion immersed in saline solution and moved by two rolls that compress the SAP.

8.2 HARNESSING SUSTAINABLE MECHANICAL ENERGY FROM SALINITY GRADIENTS

Naturally occurring salinity gradients such as in river deltas, have a huge potential as a renewable energy source [Yip16]. The global power production from those natural sources has been estimated to ≈ 2 TW, which covers roughly 10 % of the global electricity consumption [Yip12]. Several techniques have been proposed to harness this energy with the pressure retarded osmosis (PRO) process being the most prominent [Ach10]. In the PRO process, power production is generated by the osmotic driven flow of water from a feed solution to a draw solution through a semipermeable membrane. A hydroturbine extracts work from the expanding draw solution volume. A large scale prototype has been installed in Norway in 2009 that generates 10 kW of power [Ach10].

Recent studies have proposed the use of SAPs to harness the energy in a so-called osmotic engine [Zhu14; Are17b; Jan20; Bui21a; Cho22]. The swelling behavior of SAPs depends on the salt concentration of the external solution, as shown in Section 5.2, p. 48. SAPs contract in highly concentrated salt solutions but start to expand when low concentrated solution is added. Hence, by alternately switching the concentration of the feed solution, SAPs exhibit continuous shrinking and swelling cycles. This volume change can be used to move a piston and produce mechanical energy [Zhu14]. Figure 8.7 illustrates the concept of the osmotic engine.

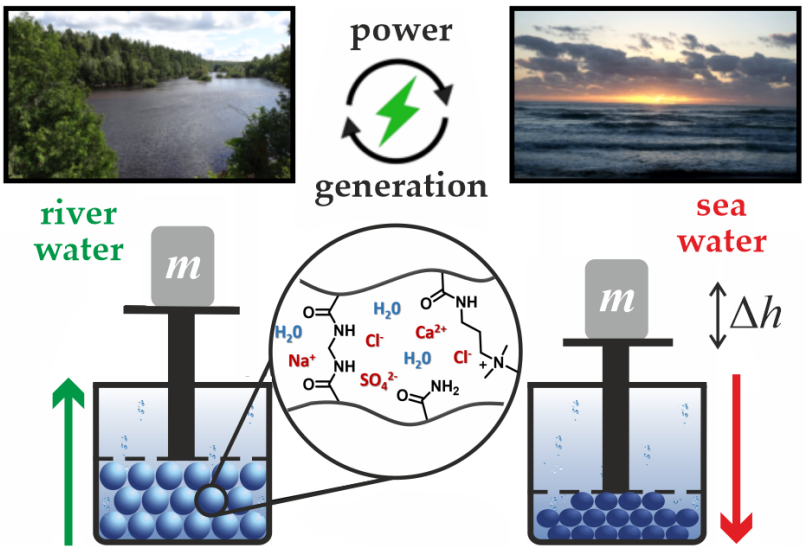

Figure 8.7: Concept of the osmotic engine to harness mechanical energy from natural salinity gradients using SAPs. Swelling and shrinking of SAPs is induced by river water and seawater, respectively. Volume change of the SAP moves a weight with mass m mimicking a piston engine.

Previous approaches have studied extensively the use of PSA based SAPs in the osmotic engine. Great effort has been devoted to understand the influence of synthetic parameters on the power output [Are17b]. The mechanical strength of swollen particles was identified as a key limiting factor of the power output as weakly crosslinked particles with high swelling capacities distinctly deform under pressure imposed by the external load, blocking thereby the path for aqueous solution to reach dry particles. This gel-blocking effect is further enhanced by a broad particle size distribution that tends to increase packing density. To overcome this kinetic hindrance and reduce the gel-blocking effect, monodisperse, spherical SAP particles have been synthesized and systematically surface-crosslinked [Jan20]. The highest power output of 0.67 $\mathrm{W\,kg^{-1}}$ of dried PSA based SAP has been achieved with a core - shell topology using $DC = 1.7\,\mathrm{mol\%}$, $DI = 75\,\mathrm{mol\%}$, and $\phi_{\mathrm{shell}} = 10\,\mathrm{vol\%}$ as synthetic parameters. Synthetic parameters are explained in Section 4.2, p. 34 and Section 4.3, p. 35.

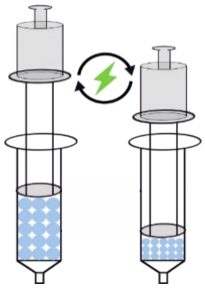

Figure 8.8: Syringe prototype of the osmotic engine.

The use of PSA, however, prevents the application of the osmotic engine in seawater, since expensive preceding water treatments of the feed solution would be required to remove divalent cations. Consequently, this dissertation explores the use of seawater resistant cationic PAM hydrogels in the osmotic engine. The osmotic engine experiments were performed in a syringe based setup, as illustrated in Figure 8.8. The recovered mechanical energy E_{exp} from the expansion of the material during swelling is expressed as the change in potential energy induced by lifting an external load according to

$$E_{\mathrm{exp}} = m_{\mathrm{load}} g_0 \Delta h_{\mathrm{load}}\,, \tag{8.9}$$

where m_{load} is the mass of external load, $g_0 = 9.81\ \mathrm{m\,s^{-2}}$ is the standard gravity constant, and Δh_{load} is the change in height of the piston. Average power output $\overline{P}$ for one swelling cycle was calculated by

$$\overline{P} = \frac{\Delta E_{\mathrm{exp}}}{\Delta t}\,. \tag{8.10}$$

Experimental parameters

To reduce gel-blocking, a spherical highly crosslinked PAM sample with $DC = 3\,\mathrm{mol\%}$, $DI = 25\,\mathrm{mol\%}$ and with a dry particle size of 200 µm was synthesized using the microfluidic technique (see described in Section 4.1). This sample composition observes similar Q_{eq} as the previously found best performing PSA analog [Are17b]. The dry hydrogel particles were swollen in artificial seawater solution for several hours and then poured into the syringe. Sieves were put beneath and on top of the swollen PAM particles to prevent leaking. A stamp with the external load was subsequently placed on top of the particles. The weight of the external load was varied in the range $12 - 1000$ g, which corresponds to the pressure range $184 - 15\,000$ Pa considering the syringe surface area of 6.6 $\mathrm{cm^2}$. First, the power output

at different weights was measured to identify the best performing external load. Therefore, swelling was initiated by adding deionized water into the syringe for 15 minutes while continuously monitoring the power output in one minute intervals. Deswelling was initiated by adding seawater for 5 minutes. Section B.6, p. 118 provides a detailed description of the sample preparation and experimental procedures. Figure 8.9 shows the maximum power output per kilogram of dry sample as a function of pressures resembling the weight of the external load.

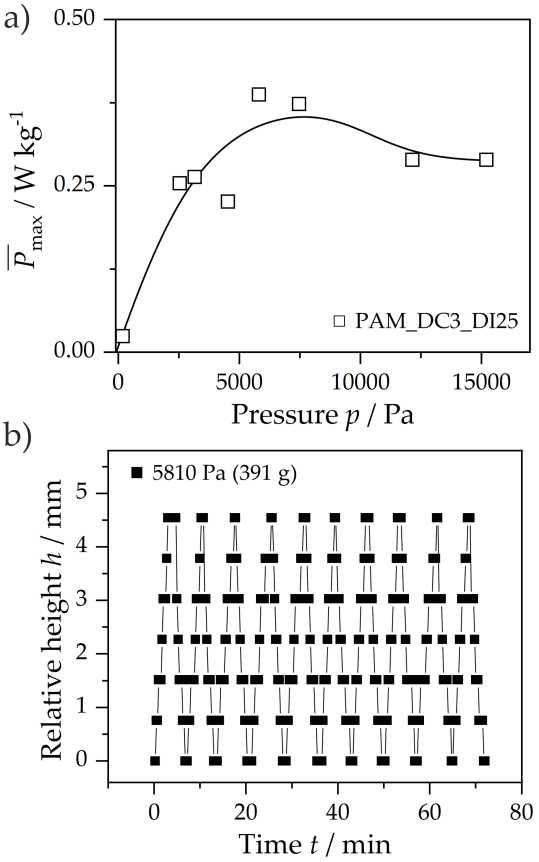

Figure 8.9: a) Average maximum power output as a function of pressure exerted by the weight of the external load on an area of 6.6 cm^2. The highest average power output of $\overline{P} = 0.39$ W kg^{-1} was achieved for the external load of 5810 Pa (391 g). Above pressures of 15000 Pa, the movement of the piston was not detectable. The solid line is a guide to the eye. b) Lifting height of the piston relative to the initial height as a function of experiment time with optimized timing between swelling and shrinking cycles that take $\approx$ 7 min in total. Seawater has no influence on the swelling-shrinking cycles within the studied time range.

It further shows the power output of the best performing load over several swelling-shrinking cycles within one hour to study the influence of seawater exposure on the performance. The highest average power output of $\overline{P} = 0.39\ \mathrm{W\,kg^{-1}}$ was achieved for the external load of 5810 Pa (391 g), which was lifted by 4.5 mm within 3 minutes. This height was used as reference to optimize the timing between consecutive swelling and shrinking periods in an one hour measurement. Swelling was initiated by adding deionized water until a height of 4.5 mm was reached. Subsequently, seawater was added to induce shrinking until the initial height was reached. This pattern was repeated over a period of 70 minutes, as shown in Figure 8.9. One swelling-shrinking cycle takes approximately 7 minutes and an influence of seawater on the maximum height was not detected, implying that PAM based hydrogels enable the application of the osmotic engine in seawater.

Limitations

Although PAM hydrogels could be used in an osmotic engine that is powered by natural salinity gradient sources, it remains a challenge to further increase the power output in terms of synthetic improvements. The PAM chemical structure is inherently unreactive, and therefore, synthetic postmodification reactions, such as surface-crosslinking, cannot be used to improve mechanical properties. Yet, surface-crosslinking has been found to profoundly reduce gel-blocking and increase the power output up to $0.67\ \mathrm{W\,kg^{-1}}$ [Jan20]. To overcome this limitation, future work could investigate whether the modification of PVAm with glycidyl trimethylammonium chloride (see Figure 5.10, p. 52 for chemical structure) improves its swelling capacity in seawater. Residual amine units can then be used to further surface-crosslink the particles with suitable crosslinker, such as diepoxides and glutaraldehyde, to minimize gel-blocking effects in the osmotic engine. As stated in the previous chapter, however, the most reasonable improvements would be the reuse of PSA based SAPs from landfill waste in large scale osmotic engines to reduce additional synthetic efforts of costly cationic hydrogels. Future work can investigate facile postmodifications routes of PSA based SAPs, for instance, using both glycidyl trimethylammonium chloride for seawater resistance and ethylene glycol diglycidyl ether for surface-crosslinking to reduce gel-blocking, as shown in Figure 8.10. Understanding the intriguing balance between different postmodification steps and their applicability in seawater will be of great interest moving forward in addition to recent technical advancements of the osmotic engine [Bui21b].

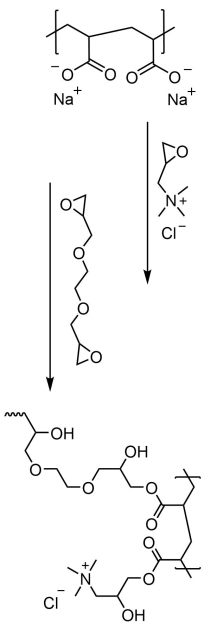

Figure 8.10: Potential chemical postmodifications of PSA.

9

CONCLUSION AND OUTLOOK

This dissertation aimed to synthesize positively charged SAPs to overcome the limited swelling capacity of PSA based SAPs in seawater caused by the high concentration of divalent Mg^{2+} and Ca^{2+} cations. Two hydrogel model systems with distinct positively charged moieties along the polymer backbone were developed. The first acrylamide based hydrogel model system (PAM) contains a cationic quaternary trimethyl ammonium functional group, whereas the other comprises a poly(vinyl amine) (PVAm) backbone. Based on water absorbency measurements of the synthesized cationic hydrogels, it can be concluded that the positive charge of the polymer backbone does not generally lead to an improved swelling capacity in seawater. Divalent SO_4^{2-} anions in seawater interact electrostatically with the cationic backbone, and therefore, can induce a network collapse. As a result of this electrostatic interaction, PVAm hydrogels with $DC = 2\,\text{mol\%}$ exhibit a rapid ion-induced volume transition above low Na_2SO_4 concentrations of 2 $\text{mmol}\,\text{L}^{-1}$, achieving thereby insignificant equilibrium swelling capacities of $Q_{eq} = 2\ \text{g}\,\text{g}^{-1}$, similar to PSA in $MgCl_2$ solutions. The PAM based model system with positively charged quaternary trimethyl ammonium groups, however, is completely unaffected by the seawater composition, indicating that the quaternary ammonium moiety plays a pivotal role in preventing the network collapse. This resistance to seawater was attributed to the bulkiness of the quaternary ammonium group, which prevents effective charge neutralization and condensation of SO_4^{2-} along the polymer backbone.

Cationic quaternary ammonium based hydrogels swell in seawater.

Future work could test this hypothesis by systematically post-modifying PVAm hydrogels with increasing concentrations of glycidyl trimethylammonium chloride, incorporating thereby positively charged quaternary ammonium moieties along the polymer backbone that should promote the swelling capacity in seawater.

A highly crosslinked PAM hydrogel was used as a separation medium in a membrane-free desalination approach to test its applicability in seawater. A hydraulic press setup with a press chamber volume of 400 mL was used to recover salt depleted water by compressing swollen PAM particles with an external mechanical force. The underlying separation mechanism is based on the Gibbs - Donnan equilibrium. Using a 11.6 $\text{g}\,\text{L}^{-1}$ seawater feed solution, 3 mL salt depleted seawater with a 30 % reduced salt concentration was recovered over 1 h applying pressures up to 50 bar. The energy demand was inferred from the pressure-volume curve yielding $E_{m^3} = 17.6\ \text{kWh}\,\text{m}^{-3}$. The discontinuous press setup distinctly limits the scaling up of this

Seawater desalination with cationic hydrogels

approach. Future work could assess alternative setups that enable a continuous process, such as a roll-to-roll setup where a sheet of SAP is in alternating fashion immersed in saline solution and continuously moved by two rolls that simultaneously function as a press.

Salinity gradients as mechanochemical power source

Another relevant SAP application that requires considerable swelling capacity in seawater is the osmotic engine, a mechanochemical concept that extracts mechanical energy from naturally occurring salinity gradients, such as river deltas. SAPs contract in highly concentrated salt solutions but start to expand when low concentrated solution is added. Hence, by alternately switching the concentration of the feed solution, SAPs exhibit continuous shrinking and swelling cycles, which can move a piston, and therefore, produce mechanical energy. Using highly crosslinked PAM hydrogels, the highest average power output of $\overline{P} = 0.39\ \mathrm{W\,kg^{-1}}$ was achieved for the external load of 5810 Pa (391 g), which was lifted by 4.5 mm within 3 minutes.

Cationic hydrogels as adsorbent for toxic divalent arsenate anions

Contamination of fresh water sources with toxic arsenate anions introduced predominantly by mining and geological conditions is a major global thread to ecological systems and human health. Future work could explore the use of cationic hydrogels as a rather simple adsorbent of the arsenate anions. The highly positively charged polymer backbone of PVAm hydrogels should electrostatically interact with the divalent and trivalent arsenate anions in contaminated water, analogue to the divalent sulfate anions in seawater. To test this hypothesis, adsorption kinetics can be assessed and compared to theoretical adsorption models.

TD NMR enables non-invasive assessment of the degree of surface - crosslinking.

Besides the development and application of seawater resistant hydrogels, this dissertation aimed to advance our understanding of the interplay between mechanical properties and molecular dynamics in hydrogels. Molecular dynamics of the polymer network chains were probed by time-domain NMR relaxometry techniques. Both ^{1}H double quantum NMR and T_2 relaxation measurements were conducted to elucidate the influence of synthetic parameters on the crosslinking density and the formation of topological network defects in PVAm hydrogels. A mathematical algorithm for the regularized inversion of double quantum build-ups and T_2 relaxation curves to obtain the respective distribution curves was developed. Based on the systematic study of T_2 relaxation curves of surface-crosslinked PVAm hydrogels, it can be concluded that the formed core - shell topology is reflected in the distribution of T_2 relaxation times, advancing thereby the topological analysis of swollen macrogels with diameters > 100 µm, which currently lacks any feasible alternatives.

The elastic plateau modulus is inversely proportional to the T_2 relaxation time.

An advanced rheological method was used to explore in-situ the relationship between the elastic modulus G' and T_2 relaxation times during the gelation of acrylic acid (AAc) by simultaneously measuring both the mechanical response and ^{1}H T_2 relaxation times. That latter was measured by a portable NMR magnet that was integrated into a

rheometer. Based on the analysis of AAc gelation kinetics with this combined approach, it can be concluded that G' and T_2 relaxation times of the polymer network approach an inverse relationship with a proportionality constant of 94 $\mathrm{kPa\,kHz^{-1}}$ at progressing gelation time. The empirical validation of this relation between macroscopic, mechanical properties and the local molecular mobility of polymer chains has important implications for the further development of non-invasive and forceless mechanical characterizations using TD NMR techniques. Application-relevant properties, such as mechanical strength and swelling capacity, can then be directly inferred from the T_2 relaxation curves.

Future research can expand the use of the Rheo-NMR device to other hydrogel systems, such as poly(acrylamide), to validate the universality of the measured correlation. The correlation plots during the polymerization of charged monomers can be investigated and compared to the theoretical predictions of the confined tube model. Future work can further explore the impact of varying crosslinker types on the time-evolution of network defects in hydrogels. The formation of defects, such as crosslinking cluster and loops, are presumably driven by the branch functionality of the crosslinker and the copolymerization parameters. Understanding the time-evolution of network defects is essential to improve application-relevant properties, such as fracture resistance, of hydrogels.

Part III

APPENDIX

A

SYNTHESIS PROCEDURES

A.1 MATERIALS AND PURIFICATION

(3-Acrylamidopropyl)trimethylammonium chloride (APTAC, 75 wt% in water, Sigma-Aldrich), acrylamide (AM, 99 %, Sigma-Aldrich), ammonium persulfate (APS, > 99 %, Acros Organics), 2,2'-azobis[2-(2-imidazolin-2-yl)propane]- dihydrochloride (VA-044, 95 %, FUJIFILM Wako Pure Chemical, bis(2-bromoethyl)ether (BBE, 95 %, Alfa Aesar), calcium chloride ($CaCl_2$, 99 %, Sigma-Aldrich), deuterium oxide (D_2O, 99 %, Sigma-Aldrich), hydrochloric acid fuming 37 % (HCl, Merck), Lupamin9095 (6.6 wt% PVAm, $M_w = 340\ \mathrm{kg\,mol^{-1}}$, BASF), magnesium chloride hexahydate ($MgCl_2 \cdot 6\,H_2O$, 98 %, Fluka), mineral oil for spectroscopy (Thermo Scientific), *N*,*N*'-methylenebis(acrylamide) (MBA, 99 % Sigma-Aldrich), *N*,*N*,*N*',*N*'-tetramethylethane-1,2-diamine (TEMED, 99.5 %, Acros Organics), sodium chloride (NaCl, 99 %, Acros Organics), sodium hydroxide (NaOH, 33 wt%, Acros Organics), sodium persulfate (SPS, > 98 %, Sigma-Aldrich), and sodium sulfate (Na_2SO_4, 99 %, Riedel-de Haen) were used as received. Acrylic acid (AAc, > 99 %, Merck) and *N*-vinylformamide (NVF, 98 %, Sigma-Aldrich) were freshly distilled at reduced pressure prior to the synthesis.

A.2 POLY(ACRYLAMIDE-*co*-(3-ACRYLAMIDOPROPYL)TRIMETHYL AMMONIUM CHLORIDE) (PAM) HYDROGELS

PAM gels were prepared by aqueous free radical crosslinking copolymerization of AM, APTAC, and MBA according to a previously reported procedure with some modifications [Baro8]. A mole fraction of 0.5 mol% of APS and TEMED to the total monomer concentration was used to initiate the copolymerization. The amount of APS and TEMED was calculated by

$$n(\mathrm{APS,TEMED}) = 0.5\,\mathrm{mol\%} \times n(\mathrm{APTAC} + \mathrm{AM}) + n(\mathrm{MEHQ}) \tag{A.1}$$

to account for the inhibitor 4-methoxyphenol (MEHQ), which is present in the APTAC monomer solution.

Three synthetic parameters, namely the degree of crosslinking *DC* (see Equation 4.3, p. 34), the degree of ionization *DI* (see Equation 4.4, p. 35), and the monomer concentration C_0 of the pregel solution were varied. In the following, the synthesis procedure of sample PAM_DC1_DI25 is explained in detail.

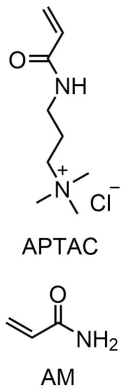

Figure A.1: Chemical structures of APTAC and AM.

Synthesis procedure

MBA (103 mg, 0.67 mmol) was dissolved in deionized water (25 mL). Subsequently, AM (3.55 g, 50 mmol, 1.0 equiv) and APTAC (75 wt% in water, 3.45 g, 16.7 mmol, 0.33 equiv) were added to the solution. TEMED (52 mg, 0.44 mmol) was added and the mixture cooled with an ice bath. The solution was purged with nitrogen for 30 min. APS (101 mg, 0.44 mmol) was dissolved in deionized water (2 mL) and added to the solution. Gelation typically started within one hour and was allowed to complete overnight.

Work-up

The hydrogel was cut into small pieces (≈ 1 cm) and placed into a large water bath for at least 4 days to remove residual monomer and low molecular weight components. The water was renewed every day. Washed hydrogel particles were then dried in a vacuum oven at 60 °C for three days. Dry particles were ground and sieved to reach particle sizes in the range $300 - 600$ µm.

Table A.1 provides an overview of the synthesized PAM hydrogel samples.

Table A.1: Overview of the synthesized PAM hydrogel samples. Dry particle sizes are in the range $300 - 600$ µm. Sample names are inferred from the synthetic parameters: degree of crosslinking DC (see Equation 4.3, p. 34), the degree of ionization DI (see Equation 4.4, p. 35), and the monomer concentration C_0 of the pregel solution.

Sample name	DC (mol%)	DI (mol%)	C_0 (wt%)
PAM_DC1_DI25	1	25	20
PAM_DC1_DI50	1	50	20
PAM_DC1_DI75	1	75	20
PAM_DC3_DI25	3	25	20
PAM_DC3_DI50	3	50	20
PAM_DC3_DI75	3	75	20
PAM_DC5_DI25	5	25	20
PAM_DC5_DI50	5	50	20
PAM_DC5_DI75	5	75	20
PAM_DC1_DI50_13	1	50	13
PAM_DC1_DI50_33	1	50	33
PAM_DC1_DI50_50	1	50	55

A.3 POLY(VINYLAMINE) (PVAM) HYDROGELS

A.3.1 *N,N′-(Oxybis(ethane-2,1-diyl))bis(N-vinylformamide) (BNVF)*

BNVF was synthesized under argon atmosphere by a nucleophilic substitution reaction of NVF with BBE. NVF (2.13 g, 30.0 mmol, 3.00 equiv) was added dropwise to a KO*t*Bu solution (1.6 M in THF, 16.9 mL, 30.0 mmol, 3.00 equiv). The mixture was stirred for 1 h and subsequently BBE (2.32 g, 10.0 mmol, 1.00 equiv) was added dropwise. The solution was stirred for 24 h and the precipitated potassium bromide removed by filtration. The solution was concentrated using a rotatory evaporator. Purification of the crude product by flash column chromatography employing a gradient of cyclohexane/ethyl acetate as eluent yielded a yellow liquid (2.07 g, 95 mol%). BNVF is a 2:1 mixture of *cis* and *trans* isomers.

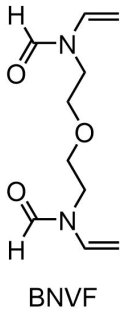

Figure A.2: Chemical structure of BNVF.

^{1}H NMR (400 MHz, $CDCl_3$): $\delta = 8.32$ (s, 1H), 8.08 (d, $J = 9.2$ Hz, 1H), 7.25 - 7.17 (m, 1H), 6.61 - 6.54 (m, 1H), 4.65 (td, $J = 15.3, 1.6$ Hz, 1H), 4.56 - 4.43 (m, 2H), 3.75 (t, $J = 6.0$ Hz, 2H), 3.57 (m, 4H) ppm.

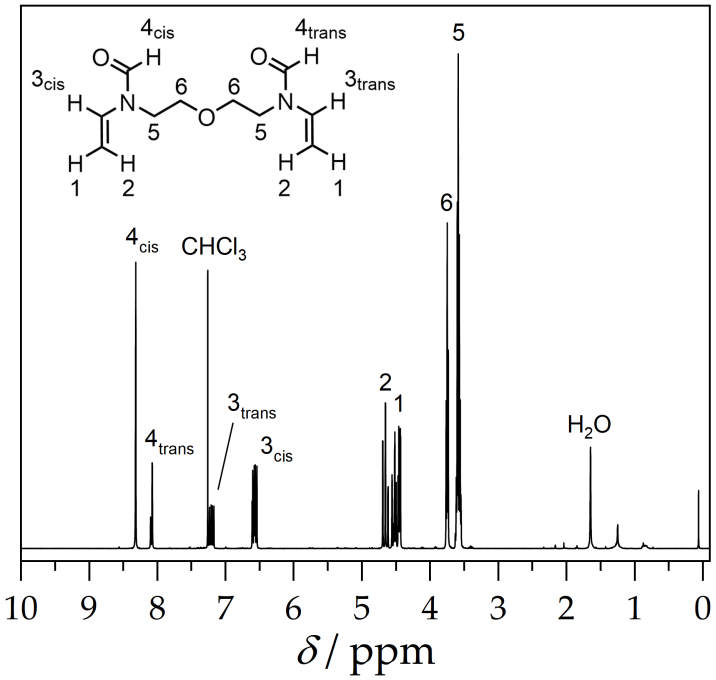

Figure A.3: ^{1}H NMR spectrum of BNVF recorded in $CDCl_3$ at 400 MHz. Depicted chemical structure shows the resonance assignments. Figure adapted from [Fen22b].

A.3.2 *Synthesis and hydrolysis of spherical poly(N-vinylformamide) (PNVF) hydrogels*

Microfluidic device parameters

Spherical PNVF hydrogel particles were prepared with a glass capillary microfluidic device, as shown in Figure 4.1, p. 33. This flow-focusing device consisted of a round capillary that was inserted into a square capillary. Two syringe pumps (Harvard Apparatus, PHD Ultra) provided a constant feed of aqueous monomer solution and oil phase. Table 4.1, p. 33 shows the variation in sizes of the capillaries and flow rates to control the particle sizes. Both immiscible fluids are forced into a narrow orifice, creating a monodisperse emulsion droplets. The droplets were collected in a beaker and the photo-polymerization was initiated by irradiating the droplets with UV light ($\lambda = 365$ nm, 100 W lamp) for two hours. The oil phase contained mineral oil with 10 wt% surfactant (ABIL EM 90, Evonik). The aqueous monomer solution was a 20 wt% mixture of NVF, BNVF, and VA-044 (photo-initiator).

Synthesis procedure

The degree of crosslinking was defined as the molar ratio of BNVF to NVF and was varied to target the following values: $DC = 1$, 2, and 3 mol%. For instance, the pre-gel composition of sample PVAm_DC1 contained NVF (3.50 g, 50.0 mmol) and BNVF (106 mg, 0.5 mmol) that were dissolved in deionized water (14 mL). A syringe was filled with the solution and spherical PNVF particles synthesized using the previously described microfluidic device. The polymerization was allowed to complete overnight at room temperature. After photo-polymerization, the PNVF particles were washed for at least four days in deionized water to remove residual monomer and low molecular weight components. The water was renewed every day. Washed hydrogel particles were then dried in a vacuum oven at 60 °C for three days.

Acidic hydrolysis

Subsequently, PVAm hydrogels were obtained by acidic hydrolysis of PNVF particles. Dry PNVF particles (250 mg) were stirred in 6 M HCl solution (250 mL) for 24 hours at 60 °C. The hydrolyzed particles were washed in deionized water for three days and dried in a vacuum oven at 60 °C for one day. The complete acidic hydrolysis was confirmed by ^{1}H NMR via the disappearance of the formamide peak, as shown in Figure A.4.

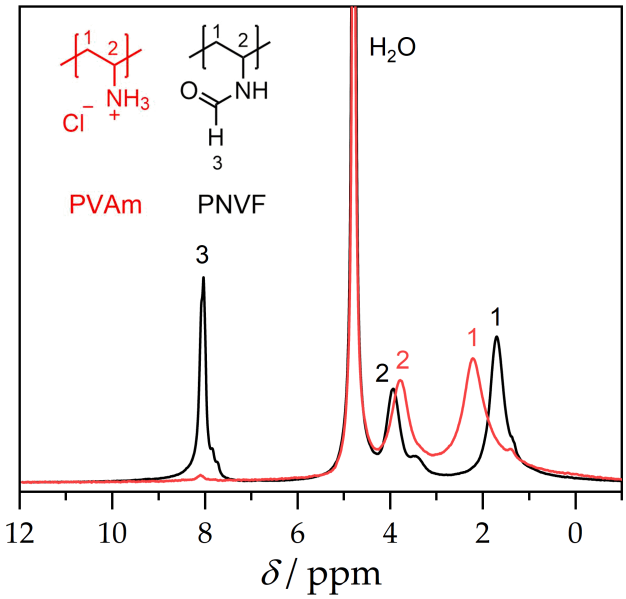

Figure A.4: ^{1}H NMR spectrum of PNVF and PVAm hydrogel particles with $DC = 1$ mol% swollen in D_2O, recorded with a benchtop NMR spectrometer (Magritek) at 80 MHz. Figure adapted from [Fen22b].

A.3.3 *Synthesis of PVAm core-shell particles*

PVAm particles were surface-crosslinked with oxalyl-based bispiperidone 1,2-bis(4-oxo-piperidin-1-yl)ethane-1,2-dione (OBP) crosslinker under mild conditions. Synthesis of OBP has been described previously [Uhl21]. One layer of dry PVAm particles (50 mg) was homogeneously distributed on the bottom of a glass vial. Subsequently, aqueous OBP crosslinker solution was added to partially swell the PVAm particles. Thickness of the shell was changed by varying the amount of crosslinker solution added to the dry particles, as defined by Equation 4.5, p. 38. From this equation the amount of water was calculated to target the following ϕ_{shell} values: $\phi_{\text{shell}} = 1$, 3, 6, and 10 vol%. The amount of OBP crosslinker calculated by Equation 4.6, p. 38. The particles were dried after 24 hours in a vacuum oven at 60 °C for one day.

Table A.2 gives an overview of the synthesized neutral PNVF, cationic PVAm and PVAm core-shell hydrogel samples.

Table A.2: Overview of synthesized PNVF, PVAm and PVAm core-shell hydrogel samples with dry particle diameters sizes of ≈ 600 µm. The sample name derives from the synthetic parameters DC (see Equation 4.3, p. 34) and ϕ_{shell} (see Equation 4.5, p. 38).

Sample	DC (mol%)	ϕ_{shell} (vol%)
PNVF_DC1	1	0
PVAm_DC1	1	0
PVAm_DC1_ϕ10	1	10
PNVF_DC2	2	0
PVAm_DC2	2	0
PVAm_DC2_ϕ1	2	1
PVAm_DC2_ϕ3	2	3
PVAm_DC2_ϕ6	2	6
PVAm_DC2_ϕ10	2	10
PNVF_DC3	3	0
PVAm_DC3	3	0
PVAm_DC3_ϕ10	3	10

A.4 POLY(ACRYLIC ACID) HYDROGELS

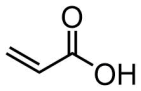

AAc

Figure A.5: Chemical structure of AAc.

PAAc hydrogels used as a reference system in the swelling measurements were prepared similarly to the PAM hydrogels via a free radical crosslinking copolymerization of AAc, SA, and MBA. The amount of SA was adjusted in-situ by deprotonating AAc with NaOH to yield the desired degree of ionization $DI = 75$ mol%. The synthesis of sample PSA_DC1_DI75 is described in the following. MBA (1.54 g, 10 mmol, 0.01 equiv) was dissolved in deionized water (230 mL) and subsequently AAc (72.6 g, 1.00 mol, 1.00 equiv) was added. The solution was cooled with an ice bath and NaOH (33 wt% solution in water, 30 g, 750 mmol, 0.75 equiv) added dropwise. Initiator $Na_2S_2O_8$ (476 mg, 2.00 mmol) was dissolved in deionized water (4 g) and added to the solution, which was subsequently purged with nitrogen for 30 minutes. Accelerator TEMED (2.29 mL, 2.32 g, 20.0 mmol) was added to initiate the polymerization. The reaction was allowed to complete overnight. The hydrogel was cut into small pieces and placed into a large water bath for at least 4 days to remove monomer and low molecular weight components. The water was renewed every day. Washed hydrogel particles were then dried in a vacuum oven at 60 °C for three days. Dry particles were ground and sieved to reach particle sizes in the range $300 - 600$ µm.

B

CHARACTERIZATION AND APPLICATION

B.1 SWELLING EXPERIMENTS

The equilibrium swelling capacity Q_{eq} of hydrogels were determined gravimetrically [Buc98]. Dry hydrogel particles ($\approx$ 10 mg) were placed on a wire mesh with a mesh size of 67 µm. The wire mesh was placed into a Petri dish using a metal rack and aqueous solution was added. The particles were allowed to swell overnight to reach the equilibrium state. Subsequently, the wire mesh with the swollen particles was gently pressed onto a paper towel to remove excess solution. The equilibrium swelling capacity was defined as the mass ratio of absorbed water to dry particles given by

$$Q_{eq} = \frac{m_{wet} - m_{mesh} - m_{poly}}{m_{poly}}, \tag{B.1}$$

where m_{wet} is the mass of swollen particles including the wire mesh, m_{mesh} is the mass of the wire mesh, and m_{poly} is the mass of dry hydrogel particles. Measurements were repeated twice for time-efficiency and showed a low standard deviation $< 5\,\%$.

Artificial Seawater composition

Stock solution of artificial seawater was prepared according to the composition of ASTM International using the four most prominent salts NaCl (24.5 $g\,L^{-1}$), $MgCl_2$ (5.2 $g\,L^{-1}$), Na_2SO_4 (4.1 $g\,L^{-1}$), and $CaCl_2$ (1.2 $g\,L^{-1}$) [Cai21]. The stock solution was diluted to obtain lower salt concentrations, retaining thereby the ratio between salts at every concentration.

B.1.1 *Swelling kinetics*

Swelling kinetics of spherical hydrogel particles were measured with a digital light microscope (Keyence VHX 900F) using a 100× magnification and coaxial illumination. A dry particle was placed into a poly(propylene) cylinder (diameter: 4 mm and height: 7 mm) and then two drops of deionized water were added to initiate the swelling process. The first 10 minutes of swelling were recorded by a video with 15 frames per second and a resolution of 1600×1200. Beyond this period, photographs were taken logarithmically spaced between 600 and 3600 seconds. The diameter was determined from snapshots of the video and photographs using the internal software of the microscope.

B.2 GELATION KINETICS VIA RHEOLOGY

The apparent viscocity was measured using a DHR-3 rheometer (TA Instruments) with a vane (four blades with diameter: 8 mm, height: 11 mm, and width: 1.2 mm) and cup (diameter: 11 mm, height: 13 mm) geometry. A constant shear rate of $\dot{\gamma} = 1\ s^{-1}$ was applied. Gelation was initiated by adding a crosslinker solution containing OBP (13 mg) and water (0.4 mL) at 40 °C to a 6.6 wt% PVAm solution (0.7 mL), which gives $DC = 5$ mol%.

B.3 TIME-DOMAIN NMR RELAXOMETRY

^{1}H time-domain NMR measurements were performed on a low-field benchtop spectrometer (minispec mq20 ND series, Bruker) with a proton resonance frequency of 19.95 MHz (0.47 T). Temperature was controlled by a Bruker VTU unit to 39.5 °C using an air flow rate of 935 L h^{-1}. Dry hydrogel particles (30 mg) were added to a flat bottom NMR tube (10 mm outer diameter) and were swollen overnight in a 1 to 9 ratio, if not mentioned otherwise, with 270 mg D_2O. Prior to the measurement, the $\pi/2$ and π pulse lengths were determined by nutation experiments for every sample, which were typically close to 2.7 µs and 5.2 µs, respectively.

B.3.1 *^{1}H longitudinal T_1 relaxation measurements*

The T_1 relaxation time was measured by the standard saturation recovery (SR) pulse sequence (t1_sat_mb.app) provided by Bruker using 32 scans, a recovery delay in the range $1 - 20\,000$ ms, and a recycle delay of 100 ms. The saturation time was approximately 10 ms and was individually adjusted for every sample to yield an initial intensity $< 5\,\%$. The T_1 build-up curves were fitted using mono- or bi-exponential functions (see Equation 6.9, p. 66).

B.3.2 *^{1}H transverse T_2 relaxation measurements*

T_2 relaxation curves of hydrogels can span over several decades. Therefore, a magic sandwich echo (MSE) and Carr-Purcell-Meiboom-Gill (CPMG) pulse sequence was used to study the PVAm particles [Höp14]. The MSE has a length of 200 µs and refocuses initial magnetization of rigid components. The CPMG/XY16 sequence investigates the relaxation process of mobile components and covers several decades in the range $0.2 - 500$ ms. The XY16 phase cycle was used to avoid spin locking effects. The CPMG T_2 relxation curve was recorded by two individual experiments with echo times $\tau_{echo} = 0.04$ and 1 ms. For signal averaging, 1024 scans were used with a recycle delay of 400 ms, which is > 5 times the T_1 of the polymer chain (see Table 6.2,

p. 67). The raw data of the MSE and two CPMG/XY16 experiments were collected in one data set and normalized to the maximum signal intensity. A mono-exponential fit on the long tail ($>$ 200 ms) was performed to quantify residual solvent signal, which was then subtracted from the raw data. Renormalization of the data yields the whole T_2 relaxation curve of the samples. Figure B.1 shows the raw data and normalization procedure of sample PNVF_DC2 as an example. Normalization and subsequent regularized inversion of T_2 relaxation curves was performed by a MATLAB algorithm (see Section 6.1, p. 53). The structure of the algorithm has been described previously in [Sco15]. The T_2 distribution contained 50 points in the range $0.003 - 300$ ms and was computed for 15 regularization parameters that were logarithmically spaced in the range $0.01 - 10$.

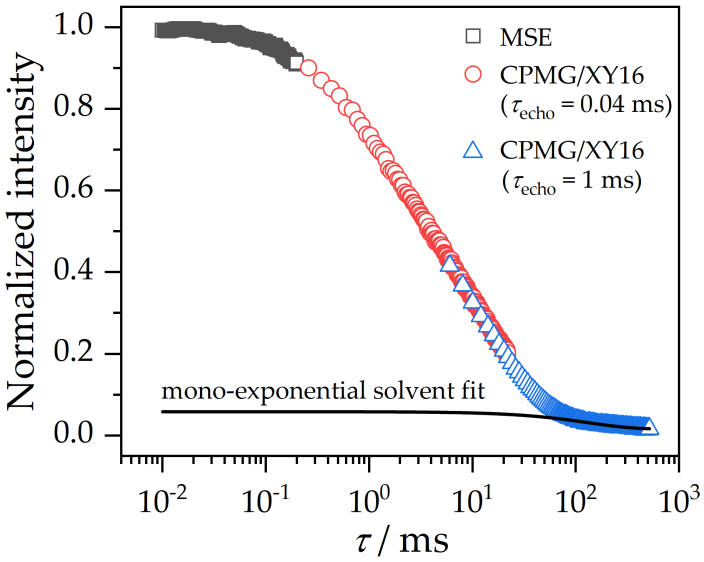

Figure B.1: Raw data of the combined MSE and CPMG data sets of sample PNVF_DC2. Figure adapted from [Fen22b].

The CPMG pulse sequence is more time-efficient than a Hahn echo experiment as it covers a large time scale in one experiment. To validate the use of the CPMG/XY16, a Hahn echo experiment was performed using 265 scans, 30 points, and varying echo times in the range $0.04 - 1$ ms as reference. In addition, a FID after a $\pi/2$ pulse was recorded to compare the intitial signal intensity to the MSE pulse sequence. Figure B.2 shows both data sets for sample PVAm_DC2. Both data sets overlap, implying a low systematic error in the combined data sets of MSE and CPMG/XY16 pulse sequences.

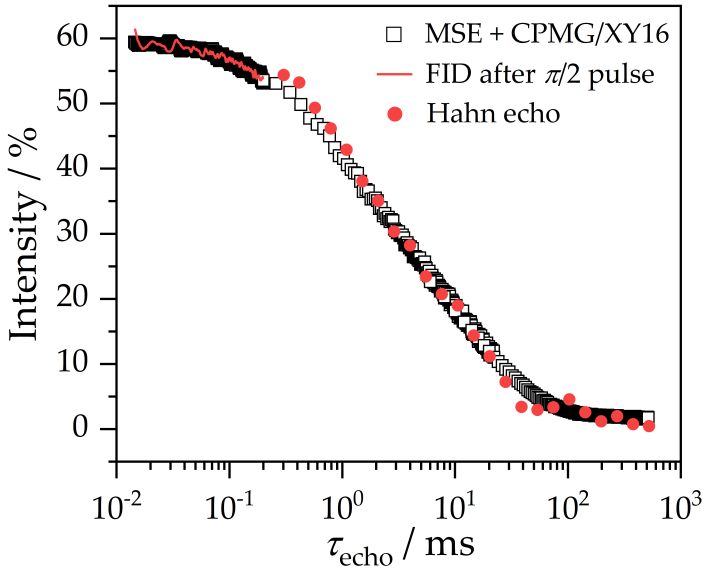

Figure B.2: Comparison of the combined MSE and CPMG/ XY16 pulse sequence with the FID after a $\pi/2$ pulse and a Hahn echo experiment for sample PVAM_DC2. Figure adapted from [Fen22b].

B.3.3 ^1H *residual dipolar coupling measurements*

^{1}H double quantum experiments were performed with a Baum-Pines pulse sequence, which was implemented for the Bruker minispec by Saalwächter et al. [Saa07; Cha11]. 1024 scans were accumulated for signal averaging with a recycle delay of 100 ms. In total, 70 DQ data points where measured with a cycle time increment of 0.01 ms. This increment was consecutively doubled after 7 DQ data points. Section 6.2, p. 57 describes data treatment and normalization for extracting the DQ build-up curves. Regularized inversion of the build-up curves were performed with a MATLAB algorithm (see Section 6.1, p. 53) using the kernel function described in Equation 6.4, p. 57. The D_{res} distribution contained 50 points in the range $0.001 - 100$ ms and was computed for 15 regularization parameters that were logarithmically spaced in the range $0.01 - 10$.

B.4 RHEO-NMR MEASUREMENTS

B.4.1 *Sample preparation*

The Rheo-NMR device was used to study the gelation kinetics of PAAc hydrogels. The total monomer weight fraction of the pre-gel composition in D_2O solvent was 20 wt%. The weight ratio of the initiator VA-044 to AAc monomer was 0.5 wt%. The degree of crosslinker *DC*

(i. e., molar ratio of MBA to AAc) was varied to target the following values: $DC = 0$, 0.05, 0.1, 0.2, 0.5, and 1 mol%. The mixture was stirred vigorously for one minute and cooled to 0 °C to avoid a premature initiation. The mixture (0.8 mL) was then poured into the lower cup geometry of the DHR-3 rheometer.

B.4.2 *Rheo-NMR device*

The centerpiece of the Rheo-NMR device is a low-field portable NMR unit with a proton resonance frequency of 25 MHz (0.6 T). The NMR magnet consists of NdFeB permanent magnets positioned according to the Halbach array. Previous studies provide a detailed description of the construction and technical outline [Rat17]. A Bruker minispec unit (NF series) performs pulsing and data acquisition of the NMR experiments. The NMR probe has a dead time of 10 µs and pulse lengths of 2.2 µs (90°) and 4.4 µs (180°). A Bruker VTU unit controlled the temperature to 40 °C using a low air flow rate of 270 $\mathrm{L\,h^{-1}}$.

B.4.3 *Rheological parameters*

Small amplitude oscillatory time sweeps were performed on a stress-controlled DHR-3 rheometer applying a low strain of $\gamma_0 = 0.5\,\%$ and an angular frequency of $\omega = 6.3\ \mathrm{rad\,s^{-1}}$. A vane (4 blades with diameter: 8 mm, height: 11 mm, width: 1.2 mm) and cup (diameter: 11mm, height: 13 mm) made out of proton-free poly(chlorotrifluoroethylene) (PCTFE) were used as geometry. The distance from the vane to the cup was 1 mm during the time sweep. The chosen parameters of the time sweep were in the linear viscoelastic regime of a gelled sample, confirmed with a strain sweep from 0.5 % to 300 % at 6.3 $\mathrm{rad\,s^{-1}}$. The internal software of the DHR-3 calculated the nominal strain by multiplying the standard geometry strain constant of a double wall concentric cylinder with the motor angular displacement.

B.4.4 ^1H *time-domain NMR parameters*

T_2 relaxation curves were recorded by a combined MSE (magic sandwich echo) and CPMG (Carr, Purcell, Meiboom, Gill) pulse sequence [Fen22a]. A XX4 phase cycle was used to avoid spin locking effects [Gul90]. The pulse sequence accumulated 8 scans for signal averaging and ended with a recycle delay of 300 ms, which leads to a duration of five seconds per experiment. The recycle delay was > 5 times the T_1 relaxation time of PAAc polymer chains. The T_1 magnetization build-up of a fully polymerized sample with $DC = 0.1$ mol% was measured by a saturation recovery pulse sequence and evaluated by a bi-exponential fit according to Equation 6.9, p. 66, as shown in Figure B.3.

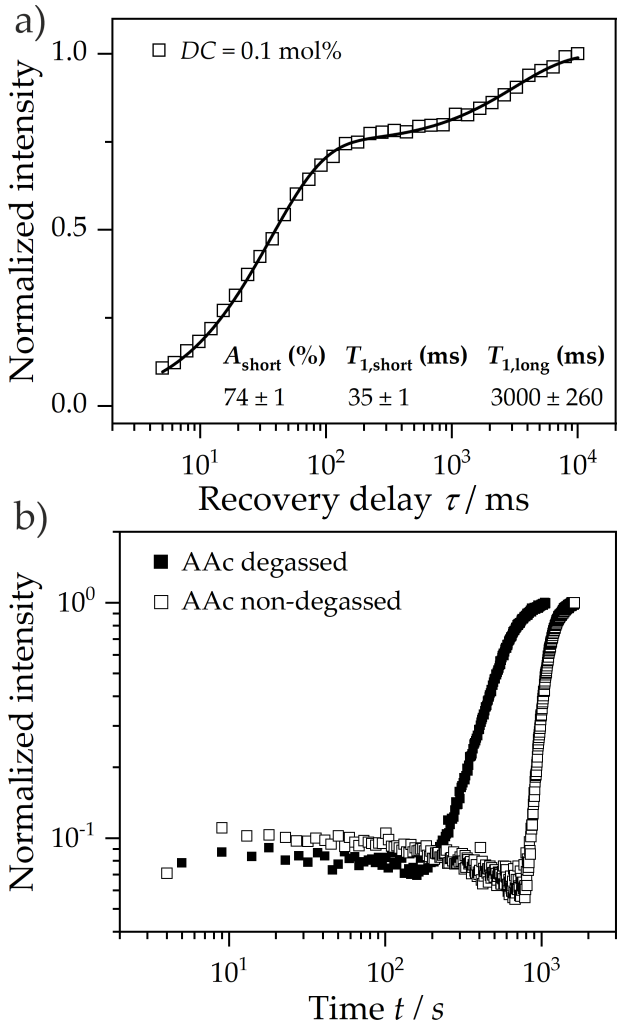

Figure B.3: Longitudinal T_1 magnetization build-up of a fully gelled PAAc hydrogel sample with $DC = 0.1$ mol% measured by a saturation recovery pulse sequence. The solid line is a least-squares bi-exponential fit according to Equation 6.9, p. 66 with A_{short} and $T_{1,\text{short}}$ the fraction and characteristic time constant of proton polymer signal, respectively. $T_{1,\text{long}}$ represents the time constant of solvent signal from residual monomer and solvent as HDO. The polymer to solvent fraction ratio $A_{\text{short}}/(1 - A_{\text{short}})$ is roughly 3:1. This ratio is expected considering the chemical structure of PAAc that has three hydrogen atoms along the polymer backbone and one hydrogen of the carboxylic group undergoing hydrogen-deuterium exchange with D_2O. b) Time-evolution of the ^{1}H NMR signal intensity of a degassed (two freeze-pump-thaw cycles) and a non-degassed AAc sample with $DC = 0$ mol%. Figure adapted from [Fen22a].

B.5 MEMBRANE-FREE DESALINATION EXPERIMENTS

B.5.1 *Salt rejection measurements*

Dry hydrogel particles where mixed overnight with 1 wt% NaCl solution (0.171 mol L^{-1}) in a specific ratio defined by

$$Q_{rel} = \frac{m_s}{m_{absorb}} = 2, \tag{B.2}$$

where m_s is the mass of the brine solution and m_{absorb} is the maximum water uptake of particles according to Q_{eq} at the used brine concentration. Setting $Q_{rel} = 2$ ensures that independent of Q_{eq} half the brine volume is always located within the swollen particles. Based on Q_{eq}, the required mass of dry hydrogel particles m_p was calculated by

$$m_p = \frac{m_{total}}{Q_{rel}(Q_{eq} + 1)}, \tag{B.3}$$

where $m_{total} = 40$ g is the total mass of the mixture. Subtracting m_p from m_{total} yields the mass of the brine solution

$$m_s = m_{total} - m_p. \tag{B.4}$$

Salt concentration of the supernatant phase was analyzed by conductivity measurements (SevenMulti, Mettler Toledo) after calibration at varying NaCl concentrations [Höp10]. The salt rejection SR is given relative to the salt concentration of the initial solution c_0 by Equation 8.3, p. 89.

B.5.2 *Desalination with the custom-build press setup*

Press setup and sample preparation

Desalination of seawater was performed on a custom-build press setup (see Figure 8.3, p. 91). The press chamber has a total volume of 400 mL. A piston was lowered to transfer mechanical force into the sample chamber. The pressure inside the chamber was measured by a pressure sensor (SD-40, Suchy Messtechnik) and the movement of the piston was measured by a distance gauge (MarCator 1086, Mahr). Dry PAM_DC5_DI25 hydrogel particles were swollen overnight in artificial seawater solution with a concentration of 11.6 g L^{-1} (0.171 mol L^{-1}) to reach the equilibrium swelling capacity. The required mass of seawater and hydrogels was determined by Equation B.2 to yield $Q_{rel} = 2$, as described in the salt rejection measurements. Then, the mixture was transferred into the press chamber. A small pressure of approximately 1 bar was applied to remove the supernatant phase. The swollen particles were then compressed by increasing the pressure linearly with 1 bar min^{-1} until a maximum pressure of 50 bar to ensure a continuous volumetric flow rate. The emerging water was contentiously collected in $3 - 10$ mL fractions.

Ion content analysis

Ion content was measured by the Engler-Bunte-Institute (Prof. Harald Horn) at the Karlsruhe Institute of Technology. The cations magnesium, calcium, and sodium were measured by inductively coupled plasma optical emission spectroscopy (ICP-OES, 5110 DV, Agilent). The aqueous sample were measured without pretreatment. The samples were atomized in an argon atmosphere at 8000 K while the emission for all elements was measured simultaneously. The anions chloride and sulfate were measured with ion chromatography (IC, 881 Compact IC pro, Metrohm). The anion exchange membrane was a Metrohm Metrosep A Supp 5-100. The liquid phase was a buffer solution with sodium bicarbonate (1 mmol L^{-1}) and sodium carbonate (3.2 mmol L^{-1}). The suppressor was 100 mmol L^{-1} H_2SO_4 and the flow rate was 0.8 mL min^{-1}.

B.6 OSMOTIC ENGINE EXPERIMENTS

Sample preparation

Monodisperse, spherical PAM_DC3_DI25 particles served as a model system and were prepared with the droplet based microfluidic technique. The outer square glass capillary had a width of 0.6 mm and the inner round glass capillary had a diameter of 0.6 mm. Flow rate of the aqueous phase was 4.3 mL h^{-1} and that of the oil phase was 17 mL h^{-1}, leading to dry particle diameters of $\approx$ 200 µm. The pre-gel solution was a mixture of a 75 wt% APTAC solution (2.3 g, 8 mmol), AM (1.8 g, 25 mmol), MBA (154 mg, 1 mmol), VA-044 (73 mg, 0.23 mmol), and H_2O (14.6 mL). The emulsion droplets were collected in a beaker and subsequently the photo-polymerization induced by irradiating the sample with UV light ($\lambda = 365$ nm, 100 W lamp) for two hours. The polymerization was allowed to complete overnight. After photo-polymerization, the PAM particles were washed for at least four days in deionized water to remove residual monomer and low molecular weight components. The water was renewed every day. Washed hydrogel particles were then dried in a vacuum oven at 60 °C for three days.

Syringe-based osmotic engine

The osmotic engine experiments were performed in a syringe-based prototype, as illustrated in Figure 8.8, p. 96. Dry PAM particles (250 mg) were swollen in artificial seawater for several hours to reach the equilibrium swelling capacity. The swollen particles were poured into the syringe which had both an inlet on top and an outlet on the bottom. Then a sieve and stamp was placed on top of the swollen hydrogels. Swelling-shrinking cycles were initiated by pouring deionized water through the inlet into the syringe. For analyzing the impact of different weights on the power output, the time of swelling and shrinking periods were fixed to 15 minutes and 5 minutes, respectively. Different weights were placed on top of the stamp to vary the mass of the external load in the range $12 - 1000$ g, which corresponds to the pressure range $184 - 15\,000$ Pa. The volume was recorded every

minute to the swelling-shrinking cycles. Average power output was calculated by Equation 8.9, p. 96 and Equation 8.10, p. 96. The surface area of the syringe was 6.6 cm^2, which was used to calculated the height from the volume. The volume was inferred from the syringe. Multiple consecutive swelling-shrinking cycles were recorded with an external weight of 391 g to study the impact of seawater over time. Therefore, the time for both the swelling and shrinking was fixed to three minutes, which allows for more cycles within the time interval.

BIBLIOGRAPHY

[Abr83] A. Abragam. *The principles of nuclear magnetism*. Paperback edition. Vol. 32. Oxford science publications. Oxford: University Press, 1983.

[Ach10] A. Achilli and A. E. Childress. "Pressure retarded osmosis: From the vision of Sidney Loeb to the first prototype installation — Review." In: *Desalination* 261.3 (2010), pp. 205–211.

[Adi16] V. Adibnia and R. J. Hill. "Universal aspects of hydrogel gelation kinetics, percolation and viscoelasticity from PA-hydrogel rheology." In: *Journal of Rheology* 60.4 (2016), pp. 541–548.

[Ali15] W. Ali, B. Gebert, T. Hennecke, K. Graf, M. Ulbricht, and J. S. Gutmann. "Design of Thermally Responsive Polymeric Hydrogels for Brackish Water Desalination: Effect of Architecture on Swelling, Deswelling, and Salt Rejection." In: *ACS Applied Materials & Interfaces* 7.29 (2015), pp. 15696–15706.

[Alm93] K. Almdal, J. Dyre, S. Hvidt, and O. Kramer. "Towards a phenomenological definition of the term 'gel'." In: *Polymer Gels and Networks* 1.1 (1993), pp. 5–17.

[And58] E. R. Andrew, A. Bradbury, and R. G. Eades. "Nuclear Magnetic Resonance Spectra from a Crystal rotated at High Speed." In: *Nature* 182.4650 (1958), p. 1659.

[Ann03] S. L. Anna, N. Bontoux, and H. A. Stone. "Formation of dispersions using "flow focusing" in microchannels." In: *Applied Physics Letters* 82.3 (2003), pp. 364–366.

[Are17a] L. Arens, J. B. Albrecht, J. Höpfner, K. Schlag, A. Habicht, S. Seiffert, and M. Wilhelm. "Energy Consumption for the Desalination of Salt Water Using Polyelectrolyte Hydrogels as the Separation Agent." In: *Macromolecular Chemistry and Physics* 218.24 (2017), p. 1700237.

[Are17b] L. Arens, F. Weißenfeld, C. O. Klein, K. Schlag, and M. Wilhelm. "Osmotic Engine: Translating Osmotic Pressure into Macroscopic Mechanical Force via Poly(Acrylic Acid) Based Hydrogels." In: *Advanced Science* 4.9 (2017), p. 1700112.

[Are19a] L. Arens, D. Barther, J. Landsgesell, C. Holm, and M. Wilhelm. "Poly(sodium acrylate) hydrogels: synthesis of various network architectures, local molecular dynamics, salt partitioning, desalination and simulation." In: *Soft Matter* 15.48 (2019), pp. 9949–9964.

[Are19b] L. Arens and M. Wilhelm. "Self–Assembled Acrylic ABA Triblock Copolymer Hydrogels with Various Block Compositions: Water Absorbency, Rheology, and SAXS." In: *Macromolecular Chemistry and Physics* 220.20 (2019), p. 1900093.

[Aro20] A. Arora, T.-S. Lin, H. K. Beech, H. Mochigase, R. Wang, and B. D. Olsen. "Fracture of Polymer Networks Containing Topological Defects." In: *Macromolecules* 53.17 (2020), pp. 7346–7355.

[Avl02] S. A. Avlonitis. "Operational water cost and productivity improvements for small-size RO desalination plants." In: *Desalination* 142.3 (2002), pp. 295–304.

[Avl03] S. A. Avlonitis, K. Kouroumbas, and N. Vlachakis. "Energy consumption and membrane replacement cost for seawater RO desalination plants." In: *Desalination* 157.1 (2003), pp. 151–158.

[BA11] M. Boulet-Audet, F. Vollrath, and C. Holland. "Rheo-attenuated total reflectance infrared spectroscopy: a new tool to study biopolymers." In: *Physical chemistry chemical physics : PCCP* 13.9 (2011), pp. 3979–3984.

[BP91] L. Brannon-Peppas and N. A. Peppas. "Equilibrium swelling behavior of pH-sensitive hydrogels." In: *Chemical Engineering Science* 46.3 (1991), pp. 715–722.

[Bai14] R. Bai, P. J. Basser, R. M. Briber, and F. Horkay. "NMR Water Self-Diffusion and Relaxation Studies on Sodium Polyacrylate Solutions and Gels in Physiologic Ionic Solutions." In: *Journal of Applied Polymer Science* 131.6 (2014).

[Bak04] V. I. Bakhmutov. *Practical NMR relaxation for chemists*. Chichester: Wiley, 2004.

[Bar01] P. Barone, A. Ramponi, and G. Sebastiani. "On the numerical inversion of the Laplace transform for nuclear magnetic resonance relaxometry." In: *Inverse Problems* 17.1 (2001), pp. 77–94.

[Bar08] M. A. Barakat and N. Sahiner. "Cationic hydrogels for toxic arsenate removal from aqueous environment." In: *Journal of Environmental Management* 88.4 (2008), pp. 955–961.

[Bau86] J. Baum and A. Pines. "NMR studies of clustering in solids." In: *Journal of the American Chemical Society* 108.24 (1986), pp. 7447–7454.

[Beh20] S. Behera and P. A. Mahanwar. "Superabsorbent polymers in agriculture and other applications: a review." In: *Polymer-Plastics Technology and Materials* 59.4 (2020), pp. 341–356.

[Bes19] D. Besghini, M. Mauri, and R. Simonutti. "Time Domain NMR in Polymer Science: From the Laboratory to the Industry." In: *Applied Sciences* 9.9 (2019), p. 1801.

[Blo46] F. Bloch. "Nuclear Induction." In: *Physical Review* 70.7-8 (1946), pp. 460–474.

[Blo48] N. Bloembergen, E. M. Purcell, and R. V. Pound. "Relaxation Effects in Nuclear Magnetic Resonance Absorption." In: *Physical Review* 73.7 (1948), pp. 679–712.

[Blü00] B. Blümich. *NMR imaging of materials*. Vol. 57. Monographs on the physics and chemistry of materials. Oxford and New York: Clarendon Press, 2000.

[Blü19] B. Blümich. *Essential NMR: For Scientists and Engineers*. Second Edition. Chemistry. Cham, Switzerland: Springer, 2019.

[Böh94] R. Böhmer. "Non-linearity and non-exponentiality of primary relaxations." In: *Journal of Non-Crystalline Solids* 172-174 (1994), pp. 628–634.

[Bor94] G. C. Borgia, V. Bortolotti, R. Brown, P. Castaldi, P. Fantazzini, and U. Soverini. "A comparison among different inversion methods for multi-exponential NMR relaxation data." In: *Magnetic Resonance Imaging* 12.2 (1994), pp. 209–212.

[Bov96] F. A. Bovey. *NMR of polymers*. San Diego: Academic Press, 1996.

[Buc98] F. L. Buchholz and A. T. Graham. *Modern Superabsorbent Polymer Technology*. New York: Wiley-VCH, 1998.

[Bui21a] T. Q. Bui, V. D. Cao, W. Wang, and A.-L. Kjøniksen. "Recovered Energy from Salinity Gradients Utilizing Various Poly(Acrylic Acid)-Based Hydrogels." In: *Polymers* 13.4 (2021), p. 645.

[Bui21b] T. Q. Bui, O.-P. Magnussen, V. D. Cao, W. Wang, A.-L. Kjøniksen, and O. Aaker. "Osmotic engine converting energy from salinity difference to a hydraulic accumulator by utilizing polyelectrolyte hydrogels." In: *Energy* 232 (2021), p. 121055.

[Bur90] W. Burchard and S. B. Ross-Murphy, eds. *Physical networks: polymers and gels: Selected papers*. Vol. 9. Selected papers from Networks. London: Elsevier Applied Science, 1990.

[Buw14] S. J. Buwalda, K. W. M. Boere, P. J. Dijkstra, J. Feijen, T. Vermonden, and W. E. Hennink. "Hydrogels in a historical perspective: from simple networks to smart materials." In: *Journal of controlled release : official journal of the Controlled Release Society* 190 (2014), pp. 254–273.

[CA93] J. P. Cohen-Addad. "NMR and fractal properties of polymeric liquids and gels." In: *Progress in Nuclear Magnetic Resonance Spectroscopy* 25.1-3 (1993), pp. 1–316.

[CC81] P.-C. Chen-Chow and S. G. Frank. "In vitro release of lidocaine from Pluronic F-127 gels." In: *International journal of pharmaceutics* 8.2 (1981), pp. 89–99.

[Cai21] Y. Cai, D. Xuan, P. Hou, J. Shi, and C. S. Poon. "Effect of seawater as mixing water on the hydration behaviour of tricalcium aluminate." In: *Cement and Concrete Research* 149 (2021), p. 106565.

[Cal04] D. Calvet, J. Y. Wong, and S. Giasson. "Rheological Monitoring of Polyacrylamide Gelation: Importance of Cross-Link Density and Temperature." In: *Macromolecules* 37.20 (2004), pp. 7762–7771.

[Cap07] S. Capaccioli, D. Prevosto, A. Best, A. Hanewald, and T. Pakula. "Applications of the rheo-dielectric technique." In: *Journal of Non-Crystalline Solids* 353.47-51 (2007), pp. 4267–4272.

[Car54] H. Y. Carr and E. M. Purcell. "Effects of Diffusion on Free Precession in Nuclear Magnetic Resonance Experiments." In: *Physical Review* 94.3 (1954), pp. 630–638.

[Cha04] Z. Chai. "Resin Microspheres as Stationary Phase for Liquid Ligand Exchange Chromatography." In: *Journal of Liquid Chromatography and Related Technologies* 27.5 (2004), pp. 911–925.

[Cha11] W. Chassé, J. L. Valentín, G. D. Genesky, C. Cohen, and K. Saalwächter. "Precise dipolar coupling constant distribution analysis in proton multiple-quantum NMR of elastomers." In: *The Journal of Chemical Physics* 134.4 (2011), p. 044907.

[Cha12a] W. Chassé, M. Lang, J.-U. Sommer, and K. Saalwächter. "Cross-Link Density Estimation of PDMS Networks with Precise Consideration of Networks Defects." In: *Macromolecules* 45.2 (2012), pp. 899–912.

[Cha12b] W. Chassé, K. Saalwächter, and J.-U. Sommer. "Thermodynamics of Swollen Networks As Reflected in Segmental Orientation Correlations." In: *Macromolecules* 45.13 (2012), pp. 5513–5523.

[Cha21] P. T. Chazovachii, M. J. Somers, M. T. Robo, D. I. Collias, M. I. James, E. N. G. Marsh, P. M. Zimmerman, J. F. Alfaro, and A. J. McNeil. "Giving superabsorbent polymers a second life as pressure-sensitive adhesives." In: *Nature Communications* 12.1 (2021), p. 4524.

[Che11] Q. Chen and L. Zhu. "PVA/PVAm Hydrogel Membranes for Removal of Metal Ions from Aqueous Solution." In: *Applied Mechanics and Materials* 130-134 (2011), pp. 1507–1510.

[Che15] Q. Chen, H. Chen, L. Zhu, and J. Zheng. "Fundamentals of double network hydrogels." In: *Journal of Materials Chemistry B* 3.18 (2015), pp. 3654–3676.

[Cho22] H. Choudhary and S. R. Raghavan. "Superfast-Expanding Porous Hydrogels: Pushing New Frontiers in Converting Chemical Potential into Useful Mechanical Work." In: *ACS Applied Materials & Interfaces* (2022).

[Chu93] Y. Chujo, K. Sada, and T. Saegusa. "Cobalt(III) bipyridyl-branched polyoxazoline complex as a thermally and redox reversible hydrogel." In: *Macromolecules* 26.24 (1993), pp. 6320–6323.

[Coh01] I. Cohen, H. Li, J. L. Hougland, M. Mrksich, and S. R. Nagel. "Using selective withdrawal to coat microparticles." In: *Science* 292.5515 (2001), pp. 265–267.

[Col10] R. H. Colby. "Structure and linear viscoelasticity of flexible polymer solutions: comparison of polyelectrolyte and neutral polymer solutions." In: *Rheologica Acta* 49.5 (2010), pp. 425–442.

[Col97] K. D. Collins. "Charge density-dependent strength of hydration and biological structure." In: *Biophysical Journal* 72.1 (1997), pp. 65–76.

[Con15] P. Conte. "Effects of ions on water structure: a low-field ^{1}H T_1 NMR relaxometry approach." In: *Magnetic resonance in chemistry : MRC* 53.9 (2015), pp. 711–718.

[Cui12] J. Cui and A. del Campo. "Multivalent H-bonds for self-healing hydrogels." In: *Chemical communications (Cambridge, England)* 48.74 (2012), pp. 9302–9304.

[Day11] I. J. Day. "On the inversion of diffusion NMR data: Tikhonov regularization and optimal choice of the regularization parameter." In: *Journal of Magnetic Resonance* 211.2 (2011), pp. 178–185.

[Dea18] J. M. Dealy and R. G. Larson. *Structure and rheology of molten polymers: From structure to flow behavior and back again*. 2nd edition. Cincinnati: Hanser Publishers, 2018.

[Di 15] F. Di Lorenzo and S. Seiffert. "Nanostructural heterogeneity in polymer networks and gels." In: *Polymer Chemistry* 6.31 (2015), pp. 5515–5528.

[Don32] F. G. Donnan and E. A. Guggenheim. "Die genaue Thermodynamik der Membrangleichgewichte." In: *Zeitschrift für Physikalische Chemie* 162A.1 (1932), pp. 346–360.

[Edh00] O. Edholm and C. Blomberg. "Stretched exponentials and barrier distributions." In: *Chemical Physics* 252.1-2 (2000), pp. 221–225.

[Eli11] M. Elimelech and W. A. Phillip. "The Future of Seawater Desalination: Energy, Technology, and the Environment." In: *Science* 333.6043 (2011), p. 712.

[Ell01] J. E. Elliott, J. W. Anseth, and C. N. Bowman. "Kinetic modeling of the effect of solvent concentration on primary cyclization during polymerization of multifunctional monomers." In: *Chemical Engineering Science* 56.10 (2001), pp. 3173–3184.

[Ell04] J. E. Elliott, M. Macdonald, J. Nie, and C. N. Bowman. "Structure and swelling of poly(acrylic acid) hydrogels: effect of pH, ionic strength, and dilution on the crosslinked polymer structure." In: *Polymer* 45.5 (2004), pp. 1503–1510.

[Erm97] B. Erman. *Structures and Properties of Rubberlike Networks*. Topics in Polymer Science Ser. Cary: Oxford University Press Incorporated, 1997.

[Fen06] X. Feng, R. Pelton, and M. Leduc. "Mechanical Properties of Polyelectrolyte Complex Films Based on Polyvinylamine and Carboxymethyl Cellulose." In: *Industrial & engineering chemistry research* 45.20 (2006), pp. 6665–6671.

[Fen20] C. Fengler, L. Arens, H. Horn, and M. Wilhelm. "Desalination of Seawater Using Cationic Poly(acrylamide) Hydrogels and Mechanical Forces for Separation." In: *Macromolecular Materials and Engineering* 305.10 (2020), p. 2000383.

[Fen22a] C. Fengler, J. Keller, K.-F. Ratzsch, and M. Wilhelm. "In Situ RheoNMR Correlation of Polymer Segmental Mobility with Mechanical Properties during Hydrogel Synthesis." In: *Advanced Science* 9.4 (2022), e2104231.

[Fen22b] C. Fengler, S. Spange, M. Sommer, and M. Wilhelm. "Synthesis of Superabsorbent Poly(vinylamine) Core–Shell Particles Monitored by Time-Domain NMR." In: *Macromolecules* 55.1 (2022), pp. 349–358.

[Fer80] J. D. Ferry. *Viscoelastic properties of polymers*. 3rd edition. New York: Wiley, 1980.

[Flo42a] P. J. Flory. "Constitution of Three-Dimensional Polymers and the Theory of Gelation." In: *Rubber Chemistry and Technology* 15.4 (1942), pp. 812–819.

[Flo42b] P. J. Flory. "Thermodynamics of High Polymer Solutions." In: *The Journal of Chemical Physics* 10.1 (1942), pp. 51–61.

[Flo43] P. J. Flory and J. Rehner. "Statistical Mechanics of Cross–Linked Polymer Networks I. Rubberlike Elasticity." In: *The Journal of Chemical Physics* 11.11 (1943), pp. 512–520.

[Flo74] P. J. Flory. "Introductory lecture." In: *Faraday Discussions of the Chemical Society* 57 (1974), p. 7.

[Flo77] P. J. Flory. "Theory of elasticity of polymer networks. The effect of local constraints on junctions." In: *The Journal of Chemical Physics* 66.12 (1977), pp. 5720–5729.

[Fuk06] K. Fukushima and Y. Kimura. "Stereocomplexed polylactides (Neo-PLA) as high-performance bio-based polymers: their formation, properties, and application." In: *Polymer International* 55.6 (2006), pp. 626–642.

[Gen04] P.-G. Gennes. *Capillarity and Wetting Phenomena: Drops, Bubbles, Pearls, Waves*. Springer eBook Collection. New York, NY: Springer, 2004.

[Gen76] P. G. de Gennes. "Dynamics of entangled polymer solutions. I. The Rouse model." In: *Macromolecules* 9.4 (1976), pp. 587–593.

[Gon03] J. P. Gong, Y. Katsuyama, T. Kurokawa, and Y. Osada. "Double-Network Hydrogels with Extremely High Mechanical Strength." In: *Advanced Materials* 15.14 (2003), pp. 1155–1158.

[Gon10] J. P. Gong. "Why are double network hydrogels so tough?" In: *Soft Matter* 6.12 (2010), p. 2583.

[Gu19] Y. Gu, J. Zhao, and J. A. Johnson. "A (Macro)Molecular-Level Understanding of Polymer Network Topology." In: *Trends in Chemistry* 1.3 (2019), pp. 318–334.

[Gue20] J. Guerrero, Y.-W. Chang, A. A. Fragkopoulos, and A. Fernandez-Nieves. "Capillary-Based Microfluidics-Coflow, Flow-Focusing, Electro-Coflow, Drops, Jets, and Instabilities." In: *Small* 16.9 (2020), e1904344.

[Gul90] T. Gullion, D. B. Baker, and M. S. Conradi. "New, compensated Carr-Purcell sequences." In: *Journal of Magnetic Resonance (1969)* 89.3 (1990), pp. 479–484.

[Guo18] X. Guo, S. Theissen, J. Claussen, V. Hildebrand, J. Kamphus, M. Wilhelm, B. Luy, and G. Guthausen. "Topological Insight into Superabsorbent Hydrogel Network Structures: a ^{1}H Double-Quantum NMR Study." In: *Macromolecular Chemistry and Physics* 219.13 (2018), p. 1800100.

[Guo19a] X. Guo, C. Pfeifer, M. Wilhelm, B. Luy, and G. Guthausen. "Structure of Superabsorbent Polyacrylate Hydrogels and Dynamics of Counterions by Nuclear Magnetic Resonance." In: *Macromolecular Chemistry and Physics* 220.10 (2019), p. 1800525.

[Guo19b] X. Guo, S. Theissen, J. Claussen, V. Hildebrand, J. Kamphus, M. Wilhelm, B. Luy, and G. Guthausen. "Dynamics of Sodium Ions and Water in Swollen Superabsorbent Hydrogels as Studied by 23Na- and 1H-NMR." In: *Macromolecular Chemistry and Physics* 220.2 (2019), p. 1800350.

[Gut16] G. Guthausen. "Analysis of food and emulsions." In: *TrAC Trends in Analytical Chemistry* 83 (2016), pp. 103–106.

[Hah50] E. L. Hahn. "Spin Echoes." In: *Physical Review* 80.4 (1950), pp. 580–594.

[Han93] P. C. Hansen and D. P. O'Leary. "The Use of the L-Curve in the Regularization of Discrete Ill-Posed Problems." In: *SIAM Journal of Scientific Computing* 14.6 (1993), pp. 1487–1503.

[Han94] P. C. Hansen. "REGULARIZATION TOOLS: A Matlab package for analysis and solution of discrete ill-posed problems." In: *Numerical Algorithms* 6.1 (1994), pp. 1–35.

[He19] Z. He, A. Shen, Y. Guo, Z. Lyu, D. Li, X. Qin, M. Zhao, and Z. Wang. "Cement-based materials modified with superabsorbent polymers: A review." In: *Construction and Building Materials* 225 (2019), pp. 569–590.

[Hil06] B. P. Hills. "Applications of Low-Field NMR to Food Science." In: *Annual Reports on NMR Spectroscopy*. Ed. by G. A. Webb. Vol. 58. Academic Press, 2006, pp. 177–230.

[His93] K. Hisatake, S. Tanaka, and Y. Aizawa. "Evaporation rate of water in a vessel." In: *Journal of Applied Physics* 73.11 (1993), pp. 7395–7401.

[Hof10] K. Hofmann, I. Kahle, F. Simon, and S. Spange. "Chromo- and fluorophoric water-soluble polymers and silica particles by nucleophilic substitution reaction of poly(vinyl amine)." In: *Beilstein Journal of Organic Chemistry* 6 (2010), p. 79.

[Hof12] A. S. Hoffman. "Hydrogels for biomedical applications." In: *Advanced Drug Delivery Reviews* 64 (2012), pp. 18–23.

[Höp10] J. Höpfner, C. Klein, and M. Wilhelm. "A Novel Approach for the Desalination of Seawater by Means of Reusable Poly(acrylic acid) Hydrogels and Mechanical Force." In: *Macromolecular Rapid Communications* 31.15 (2010), pp. 1337–1342.

[Höp13] J. Höpfner, T. Richter, P. Košovan, C. Holm, and M. Wilhelm. "Seawater Desalination via Hydrogels: Practical Realisation and First Coarse Grained Simulations." In: *Progress in Colloid and Polymer Science* 140 (2013), p. 247.

[Höp14] J. Höpfner, G. Guthausen, K. Saalwächter, and M. Wilhelm. "Network Structure and Inhomogeneities of Model and Commercial Polyelectrolyte Hydrogels as Investigated by Low-Field Proton NMR Techniques." In: *Macromolecules* 47.13 (2014), pp. 4251–4265.

[Hor00] F. Horkay, I. Tasaki, and P. J. Basser. "Osmotic Swelling of Polyacrylate Hydrogels in Physiological Salt Solutions." In: *Biomacromolecules* 1.1 (2000), pp. 84–90.

[Hor01] F. Horkay, I. Tasaki, and P. J. Basser. "Effect of Monovalent - Divalent Cation Exchange on the Swelling of Polyacrylate Hydrogels in Physiological Salt Solutions." In: *Biomacromolecules* 2.1 (2001), pp. 195–199.

[Hor06] F. Horkay, A. M. Hecht, C. Rochas, P. J. Basser, and E. Geissler. "Anomalous small angle x-ray scattering determination of ion distribution around a polyelectrolyte biopolymer in salt solution." In: *The Journal of Chemical Physics* 125.23 (2006), p. 234904.

[Hor21] F. Horkay. "Polyelectrolyte Gels: A Unique Class of Soft Materials." In: *Gels* 7.3 (2021), p. 102.

[Hri02] B. Hribar, N. T. Southall, V. Vlachy, and K. A. Dill. "How ions affect the structure of water." In: *Journal of the American Chemical Society* 124.41 (2002), pp. 12302–12311.

[Hua06] J. Huang, Z.-M. Huang, Y.-Z. Bao, and Z.-X. Weng. "Synthesis and characterization of reinforced acrylic-based superabsorbents crosslinked with divinylbenzene." In: *Journal of Applied Polymer Science* 100.2 (2006), pp. 1594–1600.

[Hug01] T. Hugel, M. Grosholz, H. Clausen-Schaumann, A. Pfau, H. Gaub, and M. Seitz. "Elasticity of Single Polyelectrolyte Chains and Their Desorption from Solid Supports Studied by AFM Based Single Molecule Force Spectroscopy." In: *Macromolecules* 34.4 (2001), pp. 1039–1047.

[Ika87] Y. Ikada, K. Jamshidi, H. Tsuji, and S. H. Hyon. "Stereocomplex formation between enantiomeric poly(lactides)." In: *Macromolecules* 20.4 (1987), pp. 904–906.

[Jae10] W. Jaeger, J. Bohrisch, and A. Laschewsky. "Synthetic polymers with quaternary nitrogen atoms—Synthesis and structure of the most used type of cationic polyelectrolytes." In: *Progress in Polymer Science* 35.5 (2010), pp. 511–577.

[Jam53] H. M. James and E. Guth. "Statistical Thermodynamics of Rubber Elasticity." In: *The Journal of Chemical Physics* 21.6 (1953), pp. 1039–1049.

[Jan20] A. Jangizehi, C. Fengler, L. Arens, and M. Wilhelm. "Optimizing the Power Production in an Osmotic Engine via Microfluidic Fabricated and Surface Crosslinked Hydrogels Utilizing Fresh and Salt Water." In: *Macromolecular Materials and Engineering* 305.7 (2020), p. 2000174.

[Jan21] A. Jangizehi and S. Seiffert. "Salt partitioning in ionized, thermo-responsive hydrogels: perspective to water desalination." In: *Journal of Chemical Physics* 154.14 (2021), p. 144902.

[Joc09] S. Jockusch, N. J. Turro, Y. Mitsukami, M. Matsumoto, T. Iwamura, T. Lindner, A. Flohr, and G. Di Massimo. "Photoinduced surface crosslinking of superabsorbent polymer particles." In: *Journal of Applied Polymer Science* 111.5 (2009), pp. 2163–2170.

[Jon19] E. Jones, M. Qadir, M. T. van Vliet, V. Smakhtin, and S.-m. Kang. "The state of desalination and brine production: A global outlook." In: *Science of the Total Environment* 657 (2019), pp. 1343–1356.

[Jon44] G. D. Jones, J. Zomlefer, and K. Hawkins. "Attempted preparation of polyvinylamine." In: *The Journal of Organic Chemistry* 09.6 (1944), pp. 500–512.

[Kat55] A. Katchalsky and I. Michaeli. "Polyelectrolyte gels in salt solutions." In: *Journal of Polymer Science* 15.79 (1955), pp. 69–86.

[Kav98] G. M. Kavanagh and S. B. Ross-Murphy. "Rheological characterisation of polymer gels." In: *Progress in Polymer Science* 23.3 (1998), pp. 533–562.

[Kes04] B. Keskinler, E. Yildiz, E. Erhan, M. Dogru, Y. Bayhan, and G. Akay. "Crossflow microfiltration of low concentration-nonliving yeast suspensions." In: *Journal of Membrane Science* 233.1-2 (2004), pp. 59–69.

[Kho19] S. C. Khoo, X. Y. Phang, C. M. Ng, K. L. Lim, S. S. Lam, and N. L. Ma. "Recent technologies for treatment and recycling of used disposable baby diapers." In: *Process Safety and Environmental Protection* 123 (2019), pp. 116–129.

[Kim07] J.-W. Kim, A. S. Utada, A. Fernández-Nieves, Z. Hu, and D. A. Weitz. "Fabrication of Monodisperse Gel Shells and Functional Microgels in Microfluidic Devices." In: *Angewandte Chemie* 119.11 (2007), pp. 1851–1854.

[Kim20] Y. J. Kim, S. J. Hong, W. S. Shin, Y. R. Kwon, S. H. Lim, H. C. Kim, J. S. Kim, J. W. Kim, and D. H. Kim. "Preparation of a biodegradable superabsorbent polymer and measurements of changes in absorption properties depending on the type of surface–crosslinker." In: *Polymers for Advanced Technologies* 31.2 (2020), pp. 273–283.

[Kiz03] M. Y. Kizilay and O. Okay. "Effect of Initial Monomer Concentration on Spatial Inhomogeneity in Poly(acrylamide) Gels." In: *Macromolecules* 36.18 (2003), pp. 6856–6862.

[Koe12] M. Koebel, A. Rigacci, and P. Achard. "Aerogel-based thermal superinsulation: an overview." In: *Journal of Sol-Gel Science and Technology* 63.3 (2012), pp. 315–339.

[Kou15] R. Kou, J. Zhang, T. Wang, and G. Liu. "Interactions between Polyelectrolyte Brushes and Hofmeister Ions: Chaotropes versus Kosmotropes." In: *Langmuir : the ACS journal of surfaces and colloids* 31.38 (2015), pp. 10461–10468.

[Kra01] L. Krasemann, A. Toutianoush, and B. Tieke. "Self-assembled polyelectrolyte multilayer membranes with highly improved pervaporation separation of ethanol/water mixtures." In: *Journal of Membrane Science* 181.2 (2001), pp. 221–228.

[Krö00] M. Kröner, J. Dupuis, and M. Winter. "N-Vinylformamide — Syntheses and Chemistry of a Multifunctional Monomer." In: *Journal für praktische Chemie* 342.2 (2000), pp. 115–131.

[Kro86] R. M. Kroeker and R. Mark Henkelman. "Analysis of biological NMR relaxation data with continuous distributions of relaxation times." In: *Journal of Magnetic Resonance (1969)* 69.2 (1986), pp. 218–235.

[Kuc14] J. Kucera. *Desalination: water from water*. Salem, Massachusetts: Wiley Online Library, 2014.

[Lan11] F. Lange, K. Schwenke, M. Kurakazu, Y. Akagi, U.-i. Chung, M. Lang, J.-U. Sommer, T. Sakai, and K. Saalwächter. "Connectivity and Structural Defects in Model Hydrogels: A Combined Proton NMR and Monte Carlo Simulation Study." In: *Macromolecules* 44.24 (2011), pp. 9666–9674.

[Lau87] R. B. Lauffer. "Paramagnetic metal complexes as water proton relaxation agents for NMR imaging: theory and design." In: *Chemical Reviews* 87.5 (1987), pp. 901–927.

[Lee09] E.-J. Lee, D.-S. Shin, H.-E. Kim, H.-W. Kim, Y.-H. Koh, and J.-H. Jang. "Membrane of hybrid chitosan-silica xerogel for guided bone regeneration." In: *Biomaterials* 30.5 (2009), pp. 743–750.

[Len87] V. Lenaerts, C. Triqueneaux, M. Quartern, F. Rieg-Falson, and P. Couvreur. "Temperature-dependent rheological behavior of Pluronic F-127 aqueous solutions." In: *International journal of pharmaceutics* 39.1-2 (1987), pp. 121–127.

[Lev08] M. H. Levitt. *Spin dynamics: Basics of nuclear magnetic resonance*. Second edition, reprinted with corrections. Chichester, Hoboken, NJ, and San Francisco, CA: John Wiley & Sons Ltd, 2008.

[Li18] Z. Li, H. Jangra, Q. Chen, P. Mayer, A. R. Ofial, H. Zipse, and H. Mayr. "Kinetics and Mechanism of Oxirane Formation by Darzens Condensation of Ketones: Quantification of the Electrophilicities of Ketones." In: *Journal of the American Chemical Society* 140.16 (2018), pp. 5500–5515.

[Li94] J. Li, A. Harada, and M. Kamachi. "Sol - Gel Transition during Inclusion Complex Formation between alpha - Cyclodextrin and High Molecular Weight Poly(ethylene glycol)s in Aqueous Solution." In: *Polymer Journal* 26.9 (1994), pp. 1019–1026.

[Lin19] T.-S. Lin, R. Wang, J. A. Johnson, and B. D. Olsen. "Revisiting the Elasticity Theory for Real Gaussian Phantom Networks." In: *Macromolecules* 52.4 (2019), pp. 1685–1694.

[Lit01] V. M. Litvinov and A. A. Dias. "Analysis of Network Structure of UV-Cured Acrylates by ^{1}H NMR Relaxation, ^{13}C NMR Spectroscopy, and Dynamic Mechanical Experiments." In: *Macromolecules* 34.12 (2001), pp. 4051–4060.

[Lit04] V. M. Litvinov and J. P. Penning. "Phase Composition and Molecular Mobility in Nylon 6 Fibers as Studied by Proton NMR Transverse Magnetization Relaxation." In: *Macromolecular Chemistry and Physics* 205.13 (2004), pp. 1721–1734.

[Luk19] A. Lukichev. "Physical meaning of the stretched exponential Kohlrausch function." In: *Physics Letters A* 383.24 (2019), pp. 2983–2987.

[MJ20] S. Mojarad-Jabali, K. Kabiri, Z. Karami, D. J. Mastropietro, and H. Omidian. "Surface cross-linked SAPs with improved swollen gel strength using diol compounds." In: *Journal of Macromolecular Science, Part A* 57.1 (2020), pp. 62–71.

[Mac94] C. W. Macosko. *Rheology: Principles, measurements, and applications*. Advances in interfacial engineering series. New York, NY: VCH, 1994.

[Mag18] S. M. Magami and R. L. Williams. "Gelation studies on acrylic acid-based hydrogels via in situ photo-crosslinking and rheology." In: *Journal of Applied Polymer Science* 135.38 (2018), p. 46691.

[Mak07] Y. Maki, H. Mori, and T. Endo. "Controlled RAFT Polymerization of N-Vinylphthalimide and its Hydrazinolysis to Poly(vinyl amine)." In: *Macromolecular Chemistry and Physics* 208.24 (2007), pp. 2589–2599.

[Man69] G. S. Manning. "Limiting Laws and Counterion Condensation in Polyelectrolyte Solutions I. Colligative Properties." In: *The Journal of Chemical Physics* 51.3 (1969), pp. 924–933.

[Man90] A. Manz, N. Graber, and H. M. Widmer. "Miniaturized total chemical analysis systems: A novel concept for chemical sensing." In: *Sensors and Actuators B: Chemical* 1.1-6 (1990), pp. 244–248.

[Mar71] J. L. Markley, W. J. Horsley, and M. P. Klein. "Spin–Lattice Relaxation Measurements in Slowly Relaxing Complex Spectra." In: *The Journal of Chemical Physics* 55.7 (1971), pp. 3604–3605.

[Mat96] A. M. Mathur, S. K. Moorjani, and A. B. Scranton. "Methods for Synthesis of Hydrogel Networks: A Review." In: *Journal of Macromolecular Science, Part C* 36.2 (1996), pp. 405–430.

[Mau06] A. Maus, C. Hertlein, and K. Saalwächter. "A Robust Proton NMR Method to Investigate Hard/Soft Ratios, Crystallinity, and Component Mobility in Polymers." In: *Macromolecular Chemistry and Physics* 207.13 (2006), pp. 1150–1158.

[McC14] J. McCann, S. Thaiboonrod, R. V. Ulijn, and B. R. Saunders. "Effects of crosslinker on the morphology and properties of microgels containing N-vinylformamide, glycidylmethacrylate and vinylamine." In: *Journal of Colloid and Interface Science* 415 (2014), pp. 151–158.

[McK94] G. B. McKenna and F. Horkay. "Effect of crosslinks on the thermodynamics of poly(vinyl alcohol) hydrogels." In: *Polymer* 35.26 (1994), pp. 5737–5742.

[Mei12] T. Meins, N. Dingenouts, J. Kübel, and M. Wilhelm. "In Situ Rheodielectric, ex Situ 2D-SAXS, and Fourier Transform Rheology Investigations of the Shear-Induced Alignment of Poly(styrene- b -1,4-isoprene) Diblock Copolymer Melts." In: *Macromolecules* 45.17 (2012), pp. 7206–7219.

[Mei58] S. Meiboom and D. Gill. "Modified Spin–Echo Method for Measuring Nuclear Relaxation Times." In: *Review of Scientific Instruments* 29.8 (1958), pp. 688–691.

[Mew11] J. Mewis. *Colloidal Suspension Rheology*. Online-Ausg. EBL-Schweitzer. Cambridge: Cambridge University Press, 2011.

[Mez20] T. Mezger. *The Rheology Handbook*. Vincentz Network, 2020.

[Moe04] S. Moelbert, B. Normand, and P. de Los Rios. "Kosmotropes and chaotropes: modelling preferential exclusion, binding and aggregate stability." In: *Biophysical Chemistry* 112.1 (2004), pp. 45–57.

[Moi15] N. Moini and K. Kabiri. "Effective parameters in surface cross-linking of acrylic-based water absorbent polymer particles using bisphenol A diethylene glycidyl ether and cycloaliphatic diepoxide." In: *Iranian Polymer Journal* 24.11 (2015), pp. 977–987.

[Moi17] N. Moini, K. Kabiri, M. J. Zohuriaan-Mehr, H. Omidian, and N. Esmaeili. "Fine tuning of SAP properties via epoxy-silane surface modification." In: *Polymers for Advanced Technologies* 28.9 (2017), pp. 1132–1147.

[Mor01] F. A. Morrison. *Understanding rheology*. Topics in chemical engineering. New York: Oxford Univ. Press, 2001.

[Mor04] I. Morfin, F. Horkay, P. J. Basser, F. Bley, A.-M. Hecht, C. Rochas, and E. Geissler. "Adsorption of divalent cations on DNA." In: *Biophysical Journal* 87.4 (2004), pp. 2897–2904.

[Mus19a] M. Mussel, P. J. Basser, and F. Horkay. "Effects of mono- and divalent cations on the structure and thermodynamic properties of polyelectrolyte gels." In: *Soft Matter* 15.20 (2019), pp. 4153–4161.

[Mus19b] M. Mussel and F. Horkay. "Experimental Evidence for Universal Behavior of Ion-Induced Volume Phase Transition in Sodium Polyacrylate Gels." In: *The journal of physical chemistry letters* 10.24 (2019), pp. 7831–7835.

[Mus21] M. Mussel, P. J. Basser, and F. Horkay. "Ion-Induced Volume Transition in Gels and Its Role in Biology." In: *Gels* 7.1 (2021).

[Nag96] H. J. Naghash and O. Okay. "Formation and structure of polyacrylamide gels." In: *Journal of Applied Polymer Science* 60.7 (1996), pp. 971–979.

[Nel05] W. B. Nelson. *Applied life data analysis*. Wiley series in probability and mathematical statistics. Applied probability and statistics. Hoboken, NJ: Wiley-Interscience, 2005.

[Nel65] J. A. Nelder and R. Mead. "A Simplex Method for Function Minimization." In: *The Computer Journal* 7.4 (1965), pp. 308–313.

[Nie21] S. Nie, K.-F. Ratzsch, S. L. Grage, J. Keller, A. S. Ulrich, J. Lacayo-Pineda, and M. Wilhelm. "Correlation between Macroscopic Elasticity and Chain Dynamics of Natural Rubber during Vulcanization as Determined by a Unique Rheo-NMR Combination." In: *Macromolecules* 54.13 (2021), pp. 6090–6100.

[Nis02] T. Nisisako, T. Torii, and T. Higuchi. "Droplet formation in a microchannel network." In: *Lab Chip* 2.1 (2002), pp. 24–26.

[Non15] T. Nonoyama and J. P. Gong. "Double-network hydrogel and its potential biomedical application: A review." In: *Proceedings of the Institution of Mechanical Engineers, Part H: Journal of Engineering in Medicine* 229.12 (2015), pp. 853–863.

[Nor04] T. Norisuye, Q. Tran-Cong-Miyata, and M. Shibayama. "Dynamic Inhomogeneities in Polymer Gels Investigated by Dynamic Light Scattering." In: *Macromolecules* 37.8 (2004), pp. 2944–2953.

[Oka94] O. Okay. "Kinetic modelling of network formation and properties in free-radical crosslinking copolymerization." In: *Polymer* 35.4 (1994), pp. 796–807.

[Oli08] J. Olivier, W. D. Johnson, and G. D. Marshall. "The logarithmic transformation and the geometric mean in reporting experimental IgE results: what are they and when and why to use them?" In: *Annals of Allergy, Asthma & Immunology* 100.4 (2008), pp. 333–337.

[Owe61] B. B. Owen, R. C. Miller, C. E. Milner, and H. L. Cogan. "The dielectric constant of water as a function of temperature and pressure." In: *Journal of Physical Chemistry* 65.11 (1961), pp. 2065–2070.

[Oye14] M. L. Oyen. "Mechanical characterisation of hydrogel materials." In: *International Materials Reviews* 59.1 (2014), pp. 44–59.

[Pak18a] P. M. Pakdel and S. J. Peighambardoust. "A review on acrylic based hydrogels and their applications in wastewater treatment." In: *Journal of Environmental Management* 217 (2018), pp. 123–143.

[Pak18b] P. M. Pakdel and S. J. Peighambardoust. "Review on recent progress in chitosan-based hydrogels for wastewater treatment application." In: *Carbohydrate Polymers* 201 (2018), pp. 264–279.

[Pan03] P. Panine, M. Gradzielski, and T. Narayanan. "Combined rheometry and small-angle x-ray scattering." In: *Review of Scientific Instruments* 74.4 (2003), pp. 2451–2455.

[Pat22] P. Patel and P. Thareja. "Hydrogels differentiated by length scales: A review of biopolymer-based hydrogel preparation methods, characterization techniques, and targeted applications." In: *European Polymer Journal* 163 (2022), p. 110935.

[Pel14] R. Pelton. "Polyvinylamine: A Tool for Engineering Interfaces." In: *Langmuir* 30.51 (2014), pp. 15373–15382.

[Pep80] N. A. Peppas and R. E. Berner. "Proposed method of intracopdal injection and gelation of poly (vinyl alcohol) solution in vocal cords: polymer considerations." In: *Biomaterials* 1.3 (1980), pp. 158–162.

[Phi11] A. Philipse and A. Vrij. "The Donnan equilibrium: I. On the thermodynamic foundation of the Donnan equation of state." In: *J. Phys. Condens. Matter (Journal of Physics: Condensed Matter)* 23.19 (2011), p. 194106.

[Pin10] R. K. Pinschmidt Jr. "Polyvinylamine at last." In: *Journal of Polymer Science Part A: Polymer Chemistry* 48.11 (2010), pp. 2257–2283.

[Pot20] J.-E. Potaufeux, J. Odent, D. Notta-Cuvier, F. Lauro, and J.-M. Raquez. "A comprehensive review of the structures and properties of ionic polymeric materials." In: *Polymer Chemistry* 11.37 (2020), pp. 5914–5936.

[Pra89] M. M. Prange, H. H. Hooper, and J. M. Prausnitz. "Thermodynamics of aqueous systems containing hydrophilic polymers or gels." In: *AIChE Journal* 35.5 (1989), pp. 803–813.

[Pre04] J. H. Prestegard, C. M. Bougault, and A. I. Kishore. "Residual dipolar couplings in structure determination of biomolecules." In: *Chemical Reviews* 104.8 (2004), pp. 3519–3540.

[Pro82] S. W. Provencher. "A constrained regularization method for inverting data represented by linear algebraic or integral equations." In: *Computer Physics Communications* 27.3 (1982), pp. 213–227.

[Pur77] E. M. Purcell. "Life at low Reynolds number." In: *American Journal of Physics* 45.1 (1977), pp. 3–11.

[QP11] M. Quesada-Pérez, J. A. Maroto-Centeno, J. Forcada, and R. Hidalgo-Alvarez. "Gel swelling theories: the classical formalism and recent approaches." In: *Soft Matter* 7.22 (2011), p. 10536.

[Qua03] H. Quan and J. Zhang. "Estimate of standard deviation for a log-transformed variable using arithmetic means and standard deviations." In: *Statistics in medicine* 22.17 (2003), pp. 2723–2736.

[Rad21] N. W. Radebe, C. Fengler, C. O. Klein, R. Figuli, and M. Wilhelm. "Rheo-IR: A combined setup for correlating chemical changes via FTIR spectroscopy and rheological properties in a strain-controlled rheometer." In: *Journal of Rheology* 65.4 (2021), pp. 681–693.

[Ram13] R. A. Ramli, W. A. Laftah, and S. Hashim. "Core–shell polymers: a review." In: *RSC Advances* 3.36 (2013), pp. 15543–15565.

[Rän18] V. Räntzsch et al. "Polymer crystallinity and crystallization kinetics via benchtop ^{1}H NMR relaxometry: Revisited method, data analysis, and experiments on common polymers." In: *Polymer* 145 (2018), pp. 162–173.

[Rän19] V. Räntzsch, M. B. Özen, K.-F. Ratzsch, E. Stellamanns, M. Sprung, G. Guthausen, and M. Wilhelm. "Polymer Crystallization Studied by Hyphenated Rheology Techniques: Rheo-NMR, Rheo-SAXS, and Rheo-Microscopy." In: *Macromolecular Materials and Engineering* 304.2 (2019), p. 1800586.

[Rap17] B. E. Rapp. *Microfluidics: Modeling, mechanics, and mathematics*. MicroNano Technologies Series. Kidlington, United Kingdom: William Andrew, 2017.

[Rat17] K.-F. Ratzsch, C. Friedrich, and M. Wilhelm. "Low-field rheo-NMR: A novel combination of NMR relaxometry with high end shear rheology." In: *Journal of Rheology* 61.5 (2017), pp. 905–917.

[Red57] A. G. Redfield. "On the Theory of Relaxation Processes." In: *IBM Journal of Research and Development* 1.1 (1957), pp. 19–31.

[Rey83] O. Reynolds. "An experimental investigation of the circumstances which determine whether the motion of water shall be direct or sinuous, and of the law of resistance in parallel channels." In: *Philosophical Transactions of the Royal Society of London* 174 (1883), pp. 935–982.

[Rhi71] W.-K. Rhim, A. Pines, and J. S. Waugh. "Time-Reversal Experiments in Dipolar-Coupled Spin Systems." In: *Physical Review B* 3.3 (1971), pp. 684–696.

[Rog08] L. Z. Rogovina, V. G. Vasil'ev, and E. E. Braudo. "Definition of the concept of polymer gel." In: *Polymer Science Series C* 50.1 (2008), pp. 85–92.

[Roy11] P. K. Roy, V. Swami, D. Kumar, and C. Rajagopal. "Removal of toxic metals using superabsorbent polyelectrolytic hydrogels." In: *Journal of Applied Polymer Science* 122.4 (2011), pp. 2415–2423.

[Rub03] M. Rubinstein and R. H. Colby. *Polymer physics*. Oxford: Oxford Univ. Press, 2003.

[Rub96] M. Rubinstein, R. H. Colby, A. V. Dobrynin, and J.-F. Joanny. "Elastic Modulus and Equilibrium Swelling of Polyelectrolyte Gels." In: *Macromolecules* 29.1 (1996), pp. 398–406.

[Saa05] K. Saalwächter. "Artifacts in Transverse Proton NMR Relaxation Studies of Elastomers." In: *Macromolecules* 38.4 (2005), pp. 1508–1512.

[Saa07] K. Saalwächter. "Proton multiple-quantum NMR for the study of chain dynamics and structural constraints in polymeric soft materials." In: *Progress in Nuclear Magnetic Resonance Spectroscopy* 51.1 (2007), pp. 1–35.

[Saa12] K. Saalwächter. "Microstructure and molecular dynamics of elastomers as studied by advanced low-resolution nuclear magnetic resonance methods." In: *Rubber Chemistry and Technology* 85.3 (2012), pp. 350–386.

[Saa18] K. Saalwächter and S. Seiffert. "Dynamics-based assessment of nanoscopic polymer-network mesh structures and their defects." In: *Soft Matter* 14.11 (2018), pp. 1976–1991.

[Sau99] B. R. Saunders and B. Vincent. "Microgel particles as model colloids: theory, properties and applications." In: *Advances in Colloid and Interface Science* 80.1 (1999), pp. 1–25.

[Sco15] A. Scotti, W. Liu, J. S. Hyatt, E. S. Herman, H. S. Choi, J. W. Kim, L. A. Lyon, U. Gasser, and A. Fernandez-Nieves. "The CONTIN algorithm and its application to determine the size distribution of microgel suspensions." In: *The Journal of Chemical Physics* 142.23 (2015), p. 234905.

[Sco97] R. A. Scott and N. A. Peppas. "Kinetic study of acrylic acid solution polymerization." In: *AIChE Journal* 43.1 (1997), pp. 135–144.

[Sei17a] S. Seiffert. "Microfluidics and Macromolecules: Top-Down Analytics and Bottom-Up Engineering of Soft Matter at Small Scales." In: *Macromolecular Chemistry and Physics* 218.2 (2017), p. 1600280.

[Sei17b] S. Seiffert. "Origin of nanostructural inhomogeneity in polymer-network gels." In: *Polymer Chemistry* 8.31 (2017), pp. 4472–4487.

[Sei17c] S. Seiffert. "Scattering perspectives on nanostructural inhomogeneity in polymer network gels." In: *Progress in Polymer Science* 66 (2017), pp. 1–21.

[She13] H. M. Shewan and J. R. Stokes. "Review of techniques to manufacture micro-hydrogel particles for the food industry and their applications." In: *Journal of Food Engineering* 119.4 (2013), pp. 781–792.

[Ste66] Steinberg I. Z., Oplatka A., and A. Katchalsky. "Mechanochemical Engines." In: *Nature* 210.5036 (1966), pp. 568–571.

[Sto44] W. H. Stockmayer. "Theory of Molecular Size Distribution and Gel Formation in Branched Polymers II. General Cross Linking." In: *The Journal of Chemical Physics* 12.4 (1944), pp. 125–131.

[Str96] J. L. Stringer and N. A. Peppas. "Diffusion of small molecular weight drugs in radiation-crosslinked poly(ethylene oxide) hydrogels." In: *Journal of Controlled Release* 42.2 (1996), pp. 195–202.

[Stu17] D. Stueber and S. Jehle. "Quantitative Component Analysis of Solid Mixtures by Analyzing Time Domain ^{1}H and ^{19}F T1 Saturation Recovery Curves (qSRC)." In: *Journal of Pharmaceutical Sciences* 106.7 (2017), pp. 1828–1838.

[Sue13] T. C. Suekama, V. Aziz, Z. Mohammadi, C. Berkland, and S. H. Gehrke. "Synthesis and characterization of poly(N-vinyl formamide) hydrogels—A potential alternative to polyacrylamide hydrogels." In: *Journal of Polymer Science Part A: Polymer Chemistry* 51.2 (2013), pp. 435–445.

[Tan79] T. Tanaka and D. J. Fillmore. "Kinetics of swelling of gels." In: *The Journal of Chemical Physics* 70.3 (1979), pp. 1214–1218.

[Teh08] S.-Y. Teh, R. Lin, L.-H. Hung, and A. P. Lee. "Droplet microfluidics." In: *Lab on a Chip* 8.2 (2008), pp. 198–220.

[Tha13] S. Thaiboonrod, C. Berkland, A. H. Milani, R. Ulijn, and B. R. Saunders. "Poly(vinylamine) microgels: pH-responsive particles with high primary amine contents." In: *Soft Matter* 9.15 (2013), pp. 3920–3930.

[Tho01] T. Thorsen, R. W. Roberts, F. H. Arnold, and S. R. Quake. "Dynamic pattern formation in a vesicle-generating microfluidic device." In: *Physical Review Letters* 86.18 (2001), pp. 4163–4166.

[Tho02] T. Thorsen, S. J. Maerkl, and S. R. Quake. "Microfluidic large-scale integration." In: *Science (New York, N.Y.)* 298.5593 (2002), pp. 580–584.

[Tod06] H. Todt, G. Guthausen, W. Burk, D. Schmalbein, and A. Kamlowski. "Water/moisture and fat analysis by time-domain NMR." In: *Food Chemistry* 96.3 (2006), pp. 436–440.

[Tra18] T. Trantidou, M. S. Friddin, A. Salehi-Reyhani, O. Ces, and Y. Elani. "Droplet microfluidics for the construction of compartmentalised model membranes." In: *Lab Chip* 18.17 (2018), pp. 2488–2509.

[Tro19] K. Trommler, T. Walther, S. Seifert, A. Seifert, H.-J. Hähnle, S. Anders, L. Kroll, and S. Spange. "The Reaction of Poly(Vinyl Amine) with Acetone in Water: Macromolecular Chemistry and Physics, 220(3), 1800444." In: *Macromolecular Chemistry and Physics* 220.3 (2019), p. 1800444.

[Uhl21] T. Uhlig, C. Fengler, A. Seifert, F. Taubert, L. Kaßner, H.-J. Hähnle, C. Hamers, M. Wilhelm, S. Spange, and M. Sommer. "Reversible and Stable Hemiaminal Hydrogels from Polyvinylamine and Highly Reactive and Selective Bis(N -acylpiperidone)s." In: *ACS Macro Letters* 10.3 (2021), pp. 389–394.

[Uta05] A. S. Utada, E. Lorenceau, D. R. Link, P. D. Kaplan, H. A. Stone, and D. A. Weitz. "Monodisperse Double Emulsions Generated from a Microcapillary Device." In: *Science* 308.5721 (2005), pp. 537–541.

[Vac11] F. Vaca Chávez and K. Saalwächter. "Time-Domain NMR Observation of Entangled Polymer Dynamics: Universal Behavior of Flexible Homopolymers and Applicability of the Tube Model." In: *Macromolecules* 44.6 (2011), pp. 1549–1559.

[Vla12] G. T. Vladisavljević, I. Kobayashi, and M. Nakajima. "Production of uniform droplets using membrane, microchannel and microfluidic emulsification devices." In: *Microfluidics and Nanofluidics* 13.1 (2012), pp. 151–178.

[Vör10] C. J. Vörösmarty et al. "Global threats to human water security and river biodiversity." In: *Nature* 467.7315 (2010), pp. 555–561.

[Wad01] N. M. Wade. "Distillation plant development and cost update." In: *Desalination* 136.1 (2001), pp. 3–12.

[Wan16] R. Wang, M. K. Sing, R. K. Avery, B. S. Souza, M. Kim, and B. D. Olsen. "Classical Challenges in the Physical Chemistry of Polymer Networks and the Design of New Materials." In: *Accounts of Chemical Research* 49.12 (2016), pp. 2786–2795.

[Wan19] H. Wang, H. Liu, H. Liu, W. Su, W. Chen, and J. Qin. "One-Step Generation of Core–Shell Gelatin Methacrylate (GelMA) Microgels Using a Droplet Microfluidic System." In: *Advanced Materials Technologies* 0.0 (2019), p. 1800632.

[Whi86] S. Whitaker. "Flow in porous media I: A theoretical derivation of Darcy's law." In: *Transport in Porous Media* 1.1 (1986), pp. 3–25.

[Wic60] O. Wichterle and D. Lím. "Hydrophilic Gels for Biological Use." In: *Nature* 185.4706 (1960), pp. 117–118.

[Wu92] X. S. Wu, A. S. Hoffman, and P. Yager. "Synthesis and characterization of thermally reversible macroporous poly(N-isopropylacrylamide) hydrogels." In: *Journal of Polymer Science Part A: Polymer Chemistry* 30.10 (1992), pp. 2121–2129.

[Yan03] Q. Yan and J. J. de Pablo. "Monte Carlo Simulation of a Coarse-Grained Model of Polyelectrolyte Networks." In: *Physical Review Letters* 91.1 (2003), p. 018301.

[Yin20] Y. Yin, B. Hu, X. Yuan, L. Cai, H. Gao, and Q. Yang. "Nanogel: A Versatile Nano-Delivery System for Biomedical Applications." In: *Pharmaceutics* 12.3 (2020).

[Yip12] N. Y. Yip and M. Elimelech. "Thermodynamic and energy efficiency analysis of power generation from natural salinity gradients by pressure retarded osmosis." In: *Environmental Science & Technology* 46.9 (2012), pp. 5230–5239.

[Yip16] N. Y. Yip, D. Brogioli, H. V. M. Hamelers, and K. Nijmeijer. "Salinity Gradients for Sustainable Energy: Primer, Progress, and Prospects." In: *Environmental Science & Technology* 50.22 (2016), pp. 12072–12094.

[ZM10] M. J. Zohuriaan-Mehr, H. Omidian, S. Doroudiani, and K. Kabiri. "Advances in non-hygienic applications of superabsorbent hydrogel materials." In: *Journal of Materials Science* 45.21 (2010), pp. 5711–5735.

[Zho16] M. Zhong, R. Wang, K. Kawamoto, B. D. Olsen, and J. A. Johnson. "Quantifying the impact of molecular defects on polymer network elasticity." In: *Science* 353.6305 (2016), p. 1264.

[Zhu14] X. Zhu, W. Yang, M. C. Hatzell, and B. E. Logan. "Energy Recovery from Solutions with Different Salinities Based on Swelling and Shrinking of Hydrogels." In: *Environmental Science & Technology* 48.12 (2014), pp. 7157–7163.

[van73] K. P. A. M. van Putte and J. den van Enden. "Pulse NMR as a quick method for the determination of the solid fat content in partially crystallized fats." In: *Journal of Physics E: Scientific Instruments* 6.9 (1973), pp. 910–912.